8-24-2012 12:00 AM

Late Archean oceans: A laboratory model of oxygen oases

Maija J. Raudsepp, *The University of Western Ontario*

Supervisor: Dr. Gordon Southam, *The University of Western Ontario*

A thesis submitted in partial fulfillment of the requirements for the Master of Science degree in Geology

LATE ARCHEAN OCEANS: A LABORATORY MODEL OF OXYGEN OASES

Thesis format: Integrated Article

by

Maija Raudsepp

Graduate Program in Earth Sciences

A thesis submitted in partial fulfillment
of the requirements for the degree of
Master of Science

The School of Graduate and Postdoctoral Studies
The University of Western Ontario
London, Ontario, Canada

THE UNIVERSITY OF WESTERN ONTARIO
School of Graduate and Postdoctoral Studies

CERTIFICATE OF EXAMINATION

Supervisor

Dr. Gordon Southam

Co-supervisor

Dr. Neil Banerjee

Examiners

Dr. Jisuo Jin

Dr. Cameron Tsujita

Dr. Hugh Henry

The thesis by

Maija Jocelyn Raudsepp

entitled:

Late Archean oceans: A laboratory model of oxygen oases

is accepted in partial fulfillment of the
requirements for the degree of
Master of Science in Geology

Date

Chair of the Thesis Examination Board

Abstract

A cyanobacterial mat, including associated aerobic and anaerobic heterotrophs, was grown in an airtight chamber to simulate the formation of an oxygen oasis in two different Archean-like environments. In the first experiment, methane added to the ecosystem was rapidly oxidized and then $O_{2(g)}$ increased to 10%. Photosynthesis resulted in a pH of 9.5 and the precipitation of magnesium-manganese carbonates within the mat. In the second experiment, daily additions of ferrous iron were rapidly oxidized, resulting in ferric hydroxide encrusted mat. The growth of cyanobacteria and iron reducing bacteria resulted in an active redox cycle between ferrous and ferric iron. Secondary precipitates, including iron-manganese nodules, dense blocky iron precipitates and iron outlined microfossils, formed at depth in the mat. This experiment suggest that a novel iron cycle may have been active in iron formations. Both experiments recreate important geochemical changes and signatures preserved in late Archean stromatolitic reefs and iron formations.

Key words: late Archean, oxygen oases, cyanobacteria, methanotrophy, iron reducing bacteria, iron formations, laboratory model

This thesis is dedicated to my family and to my husband, Adam Shypanski,
for your unconditional love.

Acknowledgements

This thesis benefited greatly from the assistance of many people. First, this project would not be possible without the inspiration, guidance and extraordinary support of my supervisor, Gord Southam. I greatly enjoyed our science talks and have learnt so much in the last two years. To Neil Banerjee, thanks for all the time and help you have given to the project. I really appreciate our discussions on geochemistry. To Clare Robinson, thank-you for being my E&S advisor and teaching me about aqueous chemistry.

I would also like to thank everyone who taught me laboratory techniques, including Tim Goldhawk and Todd Simpson for teaching me SEM, and Richard Gardiner for teaching me TEM. Thanks go out to Jon Jacobs, who built my two plexiglass chambers, to Stephen Wood, who made the thin-sections, and to Lisa Monroe, who helped me with XRD and isotopic work. Special thanks need to go to Monique Durr for all the time she put into my geochemical data. To Jeremiah Shuster, thank-you for teaching me so many geomicrobiology lab techniques and to all the Southam labmates, thank-you for the help in lab and the many interesting conversations we had. I will look back fondly on my time at Western because of you.

To my family, I am incredible grateful for your love and support, thank-you. In particular to my parents, thank-you also for giving me a love of learning, for taking me on adventures outside to give me curiosity about the natural world and for all the support you have given in my academic pursuits. Finally to my husband Adam Shypanski, thank-you for coming with me on this grand adventure and for always being there for me.

Table of Contents

List of Tables

List of Figures

List of Appendices

List of Abbreviations

%	parts per hundred
‰	parts per thousand
˚C	Celsius
ΔG_r°	Standard Gibbs free energy of reaction
µGC	micro-gas chromatography
µl	microlitre
µm	micrometre or micron
µM	micromolar
atm	atmosphere (unit of pressure)
AOM	anaerobic oxidation of methane
BASE	baseline for water-mineral interactions (un-inoculated)
BIF	banded iron formation
BSE- SEM	backscattered secondary electron - scanning electron microscopy
CFU	colony forming units
CPD	critical point drying
DIC	dissolved inorganic carbon
EDS	energy dispersive x-ray spectroscopy
EPS	extracellular polymeric substances
Fe-BASE	baseline water-mineral interactions with iron additions
Fe-OCM	oxygenic cyanobacterial mat with iron additions
FeRB	iron reducing bacteria
g	grams
Ga	Gigannum (billion years)
GIF	granular iron formation
GOE	Great Oxidation Event
IC	ion-exchange chromatography
ICP-AES	inductively coupled plasma-atomic emission spectroscopy
IF	iron formation
kg	kilogram
K_m	Michaelis constant
kV	kilovolt
L	litre
M	moles per litre
Ma	Megannum (million years)
mg	milligram
MIF-S	mass independent fractionation of sulphur isotopes
ml	millilitre
mm	millimetre

mM	millimoles per litre
mol	moles
nm	nanometre
OCM	oxygenic cyanobacterial mat
PAL	present atmospheric level
ppm	parts per million (mg/kg)
SEM	scanning electron microscopy
SRB	sulphate reducing bacteria
TEM	transmission electron microscopy
XRF	x-ray fluorescence
XRD	x-ray diffractometer

Chapter 1 Introduction

1.1 Archean bacteria, geochemical cycles and the geologic record

The emergence and evolution of novel microbial metabolic processes during the Archean Eon resulted in profound geochemical changes in Earth's atmosphere, hydrosphere and surficial geology. Early evidence of life is recorded in the Barberton Greenstone Belt, South Africa and the Pilbara Greenstone Belt, Australia after 3.5 Ga. However, the complexity of the organisms fossilized in these cratons suggests life evolved much earlier (Nisbet and Fowler 1999). In the early to mid-Archean, microbial metabolic processes were likely limited to microbial hydrogen, sulphur and iron-oxidizing phototrophy, sulphur-oxidizing chemolithoautotrophy, fermentation, sulphur reduction, iron reduction and methanogenesis (Widdel et al. 1993; Nisbet and Fowler 1999). Primary productivity pathways would have been limited by the availability of electron donors in the environment (Canfield et al. 2006).

By at least 2.7 Ga, oxygenic photosynthesis had evolved in cyanobacteria. The growth of oxygenic cyanobacteria on continental shelves created local oxygen oases in an otherwise weakly reducing Earth (Kasting 1993). With advent of oxygenic photosynthesis, primary productivity was no longer limited by electron donors and acceptors but by nutrient availability, such as phosphate or required trace metals (*e.g.,* Fennel et al. 2005). The presence of oxygen also allowed for the emergence of aerobic heterotrophy and methanotrophy as viable metabolic processes, in addition to metabolic processes present in the early Archean (Hayes 1994). The presence of oxygen would have increased the oceanic sulphate concentration and the amount of ferric iron but would have limited the extent of strictly anaerobic bacteria. These new microbial processes

changed the oxygen, carbon, hydrogen, sulphur, and iron cycles, and indirectly influenced metal redox states at multiple spatial scales, ranging from within microbial mats to global geochemical cycles.

Geologic setting for late Archean microbial mats

This thesis will focus on microbial mat communities capable of oxygenic photosynthesis that are hypothesized to have grown in Archean shallow marine environments. Precambrian continental shelves probably had broader and gentler slopes and a more uniform water circulation pattern than their Phanerozoic counterparts (Eriksson et al. 1998). In addition, epeiric seas may have been more common in the Precambrian than at present (Eriksson et al. 1998). However, in general, the shallow marine environment would have been geographically limited by the absence of large stable cratons (Cady 2001). Many Archean shallow marine environments were influenced by volcanic and hydrothermal vent activity (Brasier et al. 2006), as is evident in the close association of Archean stromatolitic sequences with volcanic facies (Hofmann 2000).

Archean ocean composition

In general, the Archean ocean composition was mainly controlled by volcanic activity and water-rock interaction on the seafloor rather than dissolved chemical inputs from continental weathering (Veizer 1988). The ocean was saturated relative to calcite, dolomite and quartz (Holland and Kasting 1992) and based on reasonable values for atmospheric CO_2, oceanic pH was at least greater than 6.5 (Grotzinger and Kasting 1993; Holland 2003). The Archean ocean temperature was not more than 57˚C, based on gypsum-anhydrite stability (Holland and Kasting 1992), but above freezing as glacial

sediments are only found in two Archean aged stratal successions, were both suggest glaciation on a local scale at most (Young 1991). Based on hydrothermal fluid inclusions, the salinity of the Archean ocean was comparable to modern seawater (De Ronde et al. 1997).

Like the Archean atmosphere, the Archean ocean was mostly anoxic, allowing for specific metal redox states to be prevalent in the Archean but relatively rare in the Proterozoic and Phanerozoic oceans. For examples, both Mn and Fe concentrations are an order of magnitude higher in Archean limestones compared to Phanerozoic limestones (Veizer et al. 1989). Assuming the oceans were saturated with respect to calcite and siderite, Ca^{2+} and Fe^{2+} concentrations would have had a ratio of $4x10^{-3}$ at equilibrium (Holland 2003). Given that Ca^{2+} has ranged from 10 to 30 mM through the Phanerozoic, Archean Fe^{2+} could have been in the range of 40 to 120 μM (Canfield 2005). The limited presence of pyrite in Archean formations suggests S^{2-} concentrations were very low (Canfield and Raiswell 1999). The lack of biogenic sulphur fractionation in Archean sulphides suggests the sulphate concentration was less than 200 μM (Habicht et al. 2002). Thus oceanic sulphur was most likely present as S°, rather than S^{2-} or SO_4^{2-} (Canfield et al. 2006). The composition of the Precambrian ocean is very poorly constrained, which in turn makes the presence of biogeochemical signatures difficult to determine.

Geologic evidence for late Archean microbial mats

Geologic evidence for life in the Archean includes fossil remains in chert, carbonate stromatolites and microbial induced sedimentary structures (Cady 2001). From the Archean, approximately 40 bacteria morphological types from 14 locations have been described (Schopf et al. 2007). Preserved morphologies include coccoid, rod, vibroid and

various sizes of filamentous bacteria (Westall 2004). However, microbial species or metabolic activity cannot be definitively determined based on morphology (Schopf et al. 2007). Archean stromatolites have been described in approximately 50 locations, with most stromatolites located in South Africa, Australia and Canada (Schopf et al. 2007). While stromatolites have preserved the macro-morphology of microbial mats, microfossils in the stromatolite are rare because re-crystallization of the carbonate destroys the organisms morphological remains (Altermann et al. 2006).

The microbial metabolic processes in Archean mats are determined by using specific biomarkers and biogeochemical signatures preserved in the rock record and phylogenetic branches from the universal tree of life (*e.g.,* Canfield and Raiswell 1999). Biosignatures include unique organic molecules left in kerogen and minerals with biological fractionated carbon, sulphur or nitrogen (Cady 2001).

$\delta^{13}C$ is a particularly useful biomarker for deducing microbial community structure because the organic carbon becomes increasely isotopically depleted as the carbon moves through trophic levels. In the late Archean, a greater range in $\delta^{13}C$ for organic carbon indicates a greater diversity of metabolic processes within shallow marine environments, most likely the result of oxygen production. For example, in the Hamersley Province, the organic carbon $\delta^{13}C$ signature for all sedimentary deposits older than 2.7 Ga and all late Archean deep water facies is consistent with anoxic metabolic processes, such as anoxygenic photosynthesis, sulphate reduction, fermentation and methanogensis (Eigenbrode and Freeman 2006). In contrast, in shallow marine facies younger than 2.7 Ga, the $\delta^{13}C$ of organic carbon has a greater range that is consistent with methanotrophy and aerobic heterotrophy, both of which require an oxygenated

environment, 'combining' oxygenic photosynthesis with fermentation and methanogensis (Figure 1.1) (Eigenbrode and Freeman 2006).

1.2 A late Archean shallow marine cyanobacteria mat

This thesis will focus on cyanobacteria using oxygenic photosynthesis, iron reducing bacteria (FeRB), sulphate reducing (SRB), methanogens and methanotrophs in an oxygen oasis. Multiple lines of evidence show these metabolic processes existed in the late Archean.

Cyanobacteria

The earliest fossils found in the Archean are hypothesized to be cyanobacteria. Schopf (1993) argues that microfossils from the Apex Chert formation, 3.465 Ga, are cyanobacteria, as the fossils have a filamentous morphology and a diameter greater than 3.5 μm. Cyanobacteria are assumed to be the primary organisms building Archean (3.5 - 2.5 Ga) stromatolites based on similarities in morphologies between Archean, Proterozoic and modern stromatolites (Altermann et al. 2006; Canfield 2005). Modern cyanobacteria are more complex than other bacterial photosynthesizers. Through lateral gene transfer cyanobacteria have a combination of photosystem 1, from green sulphur bacteria, and photosystem 2 and the Calvin-Benson cycle, from purple sulphur bacteria (Nisbet and Fowler 1999). In addition, cyanobacteria use chlorophyll a rather than bacteriochlorophyll. However, dates for these evolutionary changes have not been determined (Hohmann-Marriott and Blankenship 2011). The presence of cyanobacteria at 3.5 Ga does not necessitate an early emergence of oxygenic photosynthesis. Some modern species of cyanobacteria can use H_2S in anoxygenic photosynthesis, which is

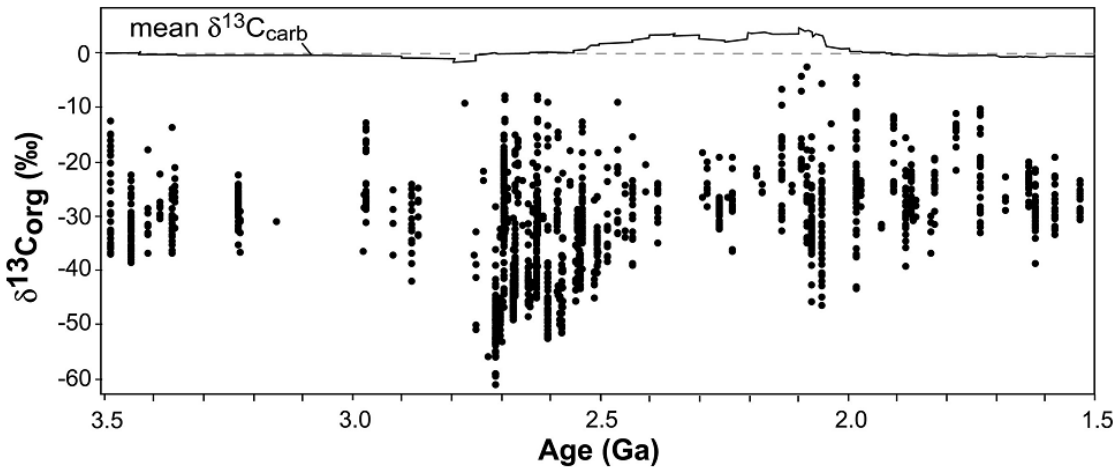

Figure 1.1 Between 2.7 and 2.5 Ga, the strongly depleted $\delta^{13}C$ values indicates presence of methanotrophy, which encorporated highly depleted methane into biomass. The more enriched $\delta^{13}C$ values indicates a decrease in methanogens and an increase in aerobic heterotrophy (from Eigenbrode and Freeman 2006).

hypothesized be the evolutionary precursory to oxygenic photosynthesis (Cohen et al. 1975).

Definitive geochemical evidence of oxygenic photosynthesis (Equation 1.1) does not appear in the geologic record until ~2.7 Ga. Evidence of oxygenic photosynthesis by cyanobacteria includes the growth of stromatolites in freshwater lakes with no source hydrogen, iron or sulphur for anoxygenic photosynthesis (Buick 1992), the presence of α-2 methylhopane, which is a cyanobacteria molecular fossil (Brocks et al. 1999), and the evolutionary radiation of organisms capable of aerobic heterotrophy (Canfield and Raiswell 1999), all of which only occur after 2.7 Ga.

$$6\,CO_2 + 6\,H_2O \rightarrow C_6H_{12}O_6 + 6\,O_2 \quad (1.1)$$

Because of the discrepancy between the record of cyanobacteria and oxygenic photosynthesis, some researchers argue for a late Archean emergence of cyanobacteria. The early to mid-Archean cyanobacteria fossils have been argued to be either abiotic pseudo-fossils formed by hydrothermal derived carbon via Fischer-Tropsch type synthesis (Brasier et al. 2002), more recent bacterial contamination, or fossils of simpler anoxygenic photosynthesizers (Westall 2004). The oldest confirmed and continuous lineage of cyanobacteria fossils are from rocks dated between 2.7 - 2.5 Ga (Altermann and Kazmierczak 2003). Nonetheless, cyanobacteria using oxygenic photosynthesis were present in the late Archean.

Precambrian cyanobacteria fossils and mats are primarily preserved in silica (Westall 2004). In addition, silicified remnants of extracellular polymeric substances (EPS) can be found in Archean fossilized biofilms (Westall et al. 2000). Cyanobacteria in modern terrestrial hydrothermal vent environments have been used as a model for

silicification in the Archean (Walter et al. 1972; Phoenix et al. 2000; Konhauser et al. 2001). Colloidal silica is electrochemically attracted to the cell wall of cyanobacteria. In particular, live cyanobacteria have been found to preferentially deposit colloidal silica on the cell poles (Amores and Warren 2009). Currently, the relationship between the Archean microbial mats and hydrothermal vents depositing silica has been difficult to determine (Westall 2004).

Calcareous cyanobacteria fossils are common in Paleozoic and Mesozoic rocks (542 - 65 Ma) but rare in the Precambrian deposits, most likely due to environmental conditions rather than biologic evolution (Riding 1982). The alkalinity gradient between the bulk ocean water and cyanobacterial mats may be responsible for the lack of fossils in Archean stromatolites (Arp et al. 2001). In geologic periods with high atmospheric CO_2 and high dissolved inorganic carbon concentrations, such as the Precambrian, carbonate concentration is uniform throughout microbial mats (Arp et al. 2001). With little to no carbonate gradient, calcite precipitation occurs throughout the mats' EPS rather than concentrated on cyanobacteria sheaths (Arp et al. 2001). As a result, microbial mats are preserved as stromatolites without preserving individual cells.

Sulphate reducing bacteria (SRB)

Dissimilatory sulphate reduction (Equations 1.2 and 1.3) is phylogenetically deep rooted metabolic process and is found in both the domains Archaea and Bacteria (Wagner et al. 1998). The presence SRB in the geologic record cannot be determined by morphology or pyritization of cell walls but is best determined by biogenic pyrite with an isotopically depleted $\delta^{34}S$ signal (Shen and Buick 2004). The presence of locally depleted $\delta^{34}S$ in pyrite in a rare 3.47 Ga sulphate deposit is consistent with the presence

of SRB in the early Archean, as suggested by phylogenetics (Shen et al. 2001). Early sulphate reducing bacteria were most likely closely associated with anoxygenic photosynthetic bacteria, as this would be a primary source of sulphate (Canfield and Raiswell 1999). At ~2.7 Ga, the range in $\delta^{34}S$ from all sedimentary pyrite increases, perhaps due to increased SRB activity in select closed basins (Canfield and Raiswell 1999). Also, $\delta^{34}S$ isotopic variation of up to 20‰ have been reported for late Archean Algoma-type BIFs in the Canadian shield (Thode and Goodwin 1983). However until the Proterozoic (2.3 Ga), the global SRB population was limited by low oceanic sulphate concentrations (<200 μM) (Habicht et al. 2002).

$$CH_3COO^- + SO_4^{2-} \rightarrow 2\,HCO_3^- + HS^- \quad (1.2)$$

$$4\,H_2 + SO_4^{2-} + H^+ \rightarrow HS^- + 4\,H_2O \quad (1.3)$$

Iron reducing bacteria (FeRB)

Like modern marine environments, FeRB may have consumed organic matter in many Precambrian sedimentary environments (Equation 1.4) (Lovley 1991). Much of the work on Archean FeRB has focused on the role of FeRB in producing Fe(II) minerals and removing organic carbon in iron formations (IFs) (discussed further in Section 1.5) (Walker 1984; Nealson and Myers 1990). Iron reduction coupled with hydrogen oxidation (Equation 1.5) is found in several deep branching hyperthermophilic Bacteria, suggesting that dissimilarly iron reduction was present in the Archean and one of the earliest forms of respiration (Vargas et al. 1998; Lovley 2004).

$$CH_3COO^- + 8\,Fe(OH)_3 + 15\,H^+ \rightarrow 2\,HCO_3^- + 8\,Fe^{2+} + 20\,H_2O \quad (1.4)$$

$$4\,H_2 + 8\,Fe(OH)_3 + 16\,H^+ \rightarrow 8\,Fe^{2+} + 24\,H_2O \quad (1.5)$$

Methanogens

Highly depleted $\delta^{13}C$ in a fluid inclusions dated at ~3.5 Ga suggests the presence of methanogens (Ueno et al. 2006). The reduction of CO_2 by either H_2 (Equation 1.6) or acetate to CH_4 (Equation 1.7) are the two primary mechanism by which methanogenesis occurs. Genetic studies have found that the first chemical pathway evolved once and is common to all methanogens (Bapteste et al. 2005). Methanogenesis is a deep rooted metabolic process, and H_2 and CO_2 was most likely available at early Archean hydrothermal vents. Konhauser et al. (2009) has argued that a decrease in oceanic nickel availability starting at 2.7 Ga may have caused a decrease in methanogenesis. In contrast, others argue that increased oceanic sulphate through the late Archean and Paleoproterozoic allowed for SRB to outcompete methanogens for organic matter (Zahnle et al. 2006).

$$CH_3COO^- + H_2O \rightarrow CH_4 + HCO_3^- \quad (1.6)$$

$$4\,H_2 + HCO_3^- + H^+ \rightarrow CH_4 + 3\,H_2O \quad (1.7)$$

Methanotrophs

While anoxygenic methanotrophy may have been possible in the early Archean, widespread methanotrophy most likely required the presence of oxygen (Equation 1.8). Hayes (1994) proposed that highly depleted late Archean $\delta^{13}C$ kerogen values were due to uptake of biotic methane into organic carbon through methanotrophy. The $\delta^{13}C$ evidence of methanotrophy is recorded in shallow marine environments and stromatolites (Hayes 1994) but limited in deep water environments (Eigenbrode and Freeman 2006). The presence of the molecular fossil 3β-methylhopanes in late Archean bitumen is also consistent with methanotrophs (Brocks et al. 2003). The extent and growth of

methanotrophy would have been dependent on the concentration of oxygen, methane and sulphate. Hayes (1994) has proposed the metabolic limits for methanotrophs are at least 20 nM dissolved CH_4 (18 - 22 µatm CH_4) and at least 650 nM dissolved O_2 (500 µatm O_2).

$$CH_4 + 2\,O_2 \rightarrow CO_2 + 2\,H_2O \quad (1.8)$$

1.3 Atmospheric change in the late Archean

Archean greenhouse gas concentration

The early Archean atmosphere was most likely weakly reducing and composed primarily of N_2, CO_2, and CH_4 (Kasting 1993). Constraints on the Archean atmospheric composition are primarily based on Earth systems computer modelling and evidence from the geologic record. One constraint on the greenhouse gas concentrations, especially CO_2 and CH_4, is the absence of geologic evidence for glaciations until 2.9 Ga despite a faint young Sun (20 - 30% less luminous compared to present) (Kump et al. 2004). If no CH_4 was present in the Archean atmosphere, the minimum CO_2 concentration required to keep Earth above freezing is 0.3 atm (Kump et al. 2004). However, mineral equilibriums from paleosols, shallow marine carbonates and banded iron formations suggests CO_2 concentrations were much lower (Rosing et al. 2010). By the late Archean, CH_4 from methanogenesis may have accumulated to levels between 100 - 1000 ppm (Kasting 2005). CO_2:CH_4 mixing ratios higher than 1:1 and CH_4 concentrations above 1000 ppm are unlikely to have occurred as a photochemical organic haze would have formed, resulting in decreased primary productivity and biotic methanogenesis (Kasting 2005). Decreasing rates of methanogenesis and thus atmospheric methane concentration may

have allowed for the rise of atmospheric oxygen (Zahnle et al. 2006; Konhauser et al. 2009). This decreasing atmospheric CH_4 resulted in Paleoproterozoic glaciations, as recorded in the Huronian Formation, Canada (Kasting 2005). The concentration of other gases in the Archean, such as ammonia, is equivocal due to a lack of geochemical proxies for these gases

Archean oxygen concentration

Many lines of evidence suggest only a low concentration of atmospheric oxygen was present before 2.4 Ga. The geochemical of composition paleosols, the presence of detrital uranium and pyrite and the lack of redbeds in Archean rocks all point towards low O_2 in the atmosphere (Holland 2003). The record of mass independent fractionation of sulphur (MIF-S) isotopes suggests $O_{2(g)}$ in the Archean was at least less than 10^{-5} PAL (present atmospheric level) (Farquhar et al. 2000; Pavlov and Kasting 2002). Atmospheric O_2 rose above 10^{-5} PAL between 2.45 and 2.32 Ga in an period known as the Great Oxidation Event (GOE) (Bekker et al. 2004).

Kasting (1993) described a stepwise oxygenation of Earth occurring by: first oxygenation of the top layer of the ocean near continental shelves, then oxygen accumulation of the atmosphere and finally oxygenation of the deep ocean. In addition to the biosignatures of oxygen discussed earlier, redox sensitive metals, such as rhenium, molydbenum, uranium, sulphur and iron, record local late Archean oxygen oases (Anbar et al. 2007). On a 2.6 - 2.5 Ga carbonate platform in the Transvaal Supergroup, South Africa, the enrichment of Re and absence of Mo, along with iron speciation in the sediment indicates that shelf waters up to several hundred metres deep had an O_2 concentration of < 10 to 100 μM, in contrast to a predominately anoxic deep ocean

(Kendall et al. 2010). Similar geochemical signatures in the Mount McRae Shale, Australia also indicate oxygenated water 50 million years before the GOE (Anbar et al. 2007). However, Kirschvink et al. (2012) argue these geochemical signatures are artifacts from post-depositional high temperature metamorphism.

Accumulation of oxygen

Explanations for the oxygenation of Earth must also take into account the 300 Ma delay between the evolution of oxygenic photosynthesis at 2.7 Ga and the recorded global oxygenation at 2.4 Ga. The global increase in atmospheric oxygen was dependent on the balance between oxygen sources and sinks. Sources of oxygen included the burial of organic carbon originally sourced from oxygenic photosynthesis, the burial of biogenic pyrite (Garrels and Perry 1974; Holland 1978) and the escape of $H_{2(g)}$ into space (Catling et al. 2001). Sinks of oxygen included the weathering and oxidation of reduced minerals and the oxidation of reduced volcanic and metamorphic gases (Holland 2002; Catling and Claire 2005).

To have a net accumulation of atmospheric oxygen, organic carbon must be stored in a geologic reservoir. Both heterotrophy and organic carbon weathering consume oxygen at the same mole ratio as oxygen production. When the rate of these reactions balances oxygenic photosynthesis no net oxygen is produced. Anaerobic heterotrophy, such as iron and sulphate reduction, has the same net balance as aerobic respiration as the production of electron acceptors consumes oxygen. Only when organic carbon is removed from the system by burial can oxygen accumulate.

Currently, only 0.1 - 0.2% of the organic carbon produced by photosynthesis is buried representing a total oxygen flux of $10 \pm 3 \times 10^{12}$ mol O_2/year (Holland 2002). The

fraction of organic carbon buried compared to the complete carbon reservoir has been determined by comparing the $\delta^{13}C$ values for organic kerogen to carbonates (Schidlowski, 1987). The difference between $\delta^{13}C$ in kerogen and carbonates has not changed since the early Archean, suggesting that 20% of the total carbon has been removed from the ocean as organic carbon throughout recorded geologic history (Schidlowski, 1987).

The accumulation of oxygen can also occur when anaerobic heterotrophy consumes organic material and the resulting reduced products are mineralized and preserved in the geologic record. The organic material consumed must originally be sourced from oxygenic photosynthesis. For iron reduction to be a net producer of oxygen 1) ferric iron (Fe^{3+}) must have been formed anaerobically and 2) Fe^{2+} product must be mineralized. For sulphate reduction to be a net producer of oxygen 1) sulphate must have been formed anaerobically and 2) resulting S^{2-} must be mineralized. As such the production of pyrite (mineralization of both biogenic ferrous iron and sulphide) could result in the accumulation of oxygen (net reaction is Equation 1.9) (Canfield 2005). Canfield et al. (2006) has proposed that sulphides produced by SRB in the Archean were most likely mineralized as pyrite rather than being biologically cycled again because phototrophic sulphur oxidizing bacteria primarily use S°. Weathering, in particular the aerobic oxidation of pyrite, consumes atmospheric oxygen (reverse of Equation 1.9).

$$16\,H^+ + 8\,SO_4^{2-} + 2\,Fe_2O_3 \rightarrow 8\,H_2O + 4\,FeS_2 + 15\,O_2 \quad (1.9)$$

1.4 Low temperature serpentinization

An important source of hydrogen is produced from the Earth's crust by serpentinization. Serpentinization, the hydrolysis of olivine, is thermodynamically favourable at low temperatures and exothermic (simplified reaction is Equation 1.10). Olivine is composed of the two end member minerals: fayalite, Fe_2SiO_4, and forsterite, Mg_2SiO_2. At temperatures lower than 200˚C, serpentinization produces a mineral assemblage of lizardite, chrysotile, magnetite and sometimes brucite (Moody 1976). Serpentinization is dependent on pH, temperature, silica activity, oxygen fugacity, the amount of water and the availability of mineral surfaces (Moody 1976; Frost and Beard 2007).

$$6(Mg,Fe)_2SiO_4 + 7H_2O \rightarrow 3(Mg,Fe)_3Si_2O_5(OH)_4 + Fe_3O_4 + H_2 \quad (1.10)$$

Geochemical reactions in serpentinization

Many of the specific geochemical reactions in serpentinization are unknown. Bach et al. (2006) proposed a sequence of reactions for serpentinization, whereby serpentinization first occurs without magnetite (Equation 1.11), and then silica reacts with the iron-rich brucite to form magnetite, serpentine and $H_{2(g)}$ (Equation 1.12). The silica in reaction 1.12 may be sourced from the breakdown of orthopyroxene or other silicates (Bach et al. 2006). In general, the process of serpentinization excludes iron from the serpentine minerals and enriches iron in brucite and magnetite (Moody 1976).

$$2Mg_{1.8}Fe_{0.2}SiO_4 + 3H_2O \rightarrow Mg_{2.85}Fe_{0.15}Si_2O_5(OH)_4 + Mg_{0.75}Fe_{0.25}(OH)_2 \quad (1.11)$$

$$57Mg_{0.75}Fe_{0.25}(OH)_2 + 30SiO_2$$

$$\rightarrow 15Mg_{2.85}Fe_{0.15}Si_2O_5(OH)_4 + 23H_2O + 4Fe_3O_4 + 4H_{2(g)} \quad (1.12)$$

In fayalite serpentinization, iron oxidation in anaerobic reducing environments is coupled to the reduction of H_2O to H_2 (Neal and Stanger 1983). This process is estimated to account for 50% of all iron oxidation on the modern ocean floor (Bach and Edwards 2003). Serpentinization also results in a pH increase and locally enhances carbonate precipitation (Kelley et al. 2001). In Fischer-Tropsch type reactions, CO_2 and H_2 can abiotically react on mineral catalysts, such as a Ni-Fe alloys, chromite or magnetite, to form CH_4 and other hydrocarbons (Equation 1.13) (Foustoukos and Seyfried 2004). These Fischer-Tropsch type reactions had been found in modern hydrothermal vents (*e.g.* Kelley et al. 2005; Konn et al. 2009) and both hydrogen and methane have been produced by serpentinization at low temperatures (30 - 70˚C) in the laboratory (Neubeck et al. 2011).

$$CO_2 + \left[\frac{m}{2n}\right] H_2 \rightarrow \left(\frac{1}{n}\right) C_nH_m + 2H_2O \quad (1.13)$$

Serpentinization and life

While serpentinites have been found in many tectonic environments (Fyer 2002), the discovery of the off-axis Lost City hydrothermal vent field has created greater interest in the connection between biology and serpentinization (Kelley et al. 2001). At Lost City, carbonate hydrothermal vents up to 60 m tall emit warm (40 - 75˚C), alkaline (pH < 9.0) water with relatively high concentrations of H_2 and CH_4 (Kelley et al. 2001). These vents support a large biomass of methanogens and methanotrophs, as well as sulphur oxidizing bacteria and sulphate reducing (H_2 oxidizing) bacteria (Kelley et al. 2005; Brazelton et al. 2006). Several researchers have proposed that life originated at alkaline hydrothermal vents undergoing serpentinization (Sleep et al. 2004; Russell et al. 2010). In particular, the slow reaction already occurring abiotically at the vent between H_2 and

CO_2 to produce CH_4 (Equation 1.13) could be catalyzed by Earth's earliest bacteria for growth and energy (Russell et al. 2010; Lane et al. 2010).

In the Archean, abiotically and biotically produced methane would have accumulated in the atmosphere. Methane that entered the troposphere would have been photolysed by strong UV radiation into H_2 and CO_2 (Catling et al. 2001). If this H_2 exited the top of the atmosphere into space, the net result was the irreversible oxidation of Earth's crust (Catling et al. 2001), including the accumulation of ferric iron when the H_2 was produced through serpentinization. As such, serpentinization was important in the iron, carbon, and hydrogen biological and geological cycles.

1.5 Iron Formations

Resolving the mechanisms responsible for the deposition of Archean and Paleoproterozoic iron formations (IFs) is also important for understanding the biogeochemical cycles and the redox state of oceans on early Earth (Trendall 2002). IFs are defined as rocks originally deposited as a chemical sediment, that contain at least 15 wt% iron and that are typically laminated with layers of iron and chert (James 1954). Most IFs contain between 20 to 40 wt% total Fe and 43 to 56 wt% SiO_2 (Klein 2005). Hematite, magnetite and chert are the most abundant minerals in IFs but carbonates (siderite and ankerite) and silicates (stilpnomelane, greenalite and riebeckite) may also be present (Trendall 2002). IFs are only found in rocks dated between 3.8 and 1.8 Ga and between 0.8 and 0.6 Ga (associated with Neoproterozoic glaciations), periods characterized by an anoxic ferruginous ocean that allowed for the transport of dissolved iron (Klein 2005). However, the relationship between the oxidation state of the Earth's

ocean and IFs is more complicated given the deposition of IFs continued at least 300 Ma after the GOE (Farquhar et al. 2011). IFs deposited in the Neoproterozoic will not be discussed in this thesis as global climate and biogeochemical cycles were likely very different at this time compared to the Archean and Paleoproterozoic.

IFs from the Archean and Paleoproterozoic are broadly divided into Algoma-type iron formations and Superior-type iron formations (Figure 1.2), which have been interpreted to occur in different depositional environments (Gross 1980). Algoma-type IFs most are commonly found in Archean greenstone belts (James 1983). In sequences, Algoma-type IFs are associated with volcanic rocks and have a smaller lateral thickness than Superior-type IFs (Gross 1980). Superior-type IFs are most common in rocks dated between 2.7 and 1.8 Ga, with a peak in deposition approximately concurrent with the GOE (~2.5 - 2.3 Ga) (Trendall 2002). Superior-type IFs are not associated with volcanic rocks, may be laterally continuous for hundreds of kilometres and are hypothesized to have formed on continental shelves (Gross 1980). The two largest iron formations, the Hamersley succession, Australia and the Transvaal succession, South Africa, are both Superior-type IFs and are hypothesized to have been deposited in the same basin between 2.5 and 2.44 Ga (Beukes and Gutzmer 2008). However, classification of all IFs based on the characteristics of typical Algoma and Superior-type IFs has been somewhat problematic (Trendall 2002).

IFs are also classified by textural characteristics. IFs can occur as banded iron formations (BIFs), which are composed of alternating layers of silica and iron, or as granular iron formations (GIFs), which are composed of iron particles in a silica matrix (Trendall 2002). Most IFs older than 2.0 Ga are banded, while most IFs deposited

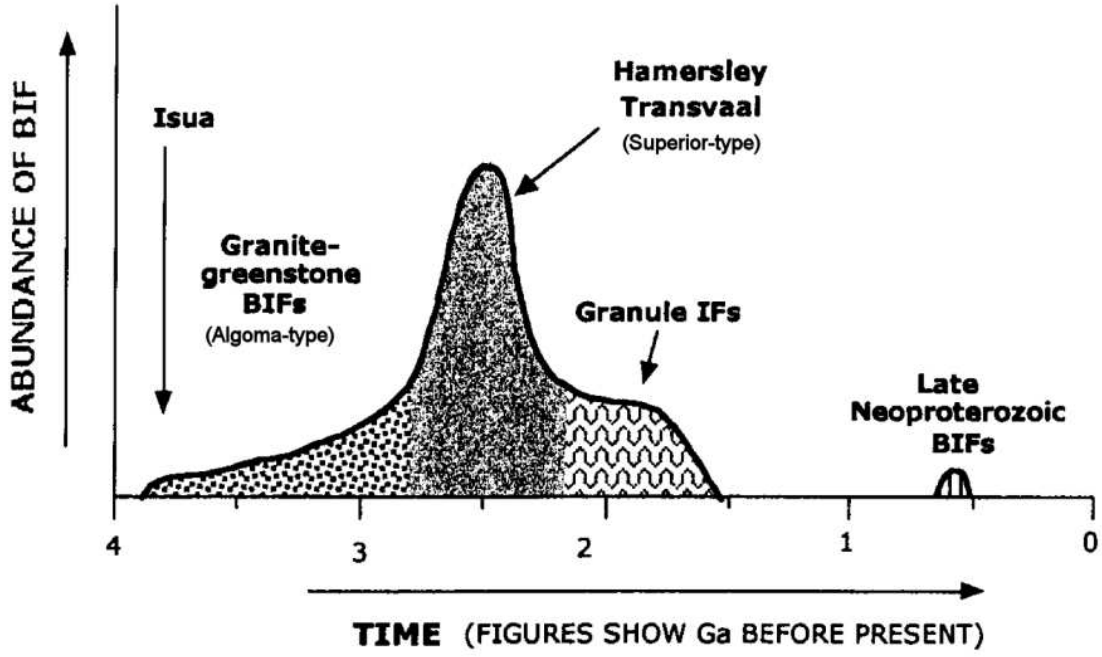

Figure 1.2 In addition to changing characteristics of iron formations, the depositional volume of IFs increased at ~2.5 Ga. The earliest deposited IF was in the Isua greenstone belt at 3.8 Ga (modified from Trendall 2002).

between 2.0 and 1.8 Ga are granular (Trendall 2002). BIFs are composed of 0.3 to 1.7 mm microbands composed of alternating laminations of iron-rich and silica-rich chemical sediment (Klein 2005). Because thinly laminated BIFs preserve delicate micro-structures and contain very little continental detritus (only contain 0.09 to 1.8 wt% Al_2O_3), they are hypothesized to have been deposited below the 200 m storm wave base on continental shelves (Klein 2005). Granular iron formations by definition have a granular, colloidal texture and are hypothesized to have been formed in a shallow marine setting where waves and tides reworked the already deposited and laminated chemical mud (Simonson and Goode 1989; Beukes and Gutzmer 2008). This morphology may be more common in the Paleoproterozoic compared to the Archean due to a change in oceanic redox structure (Klein 2005).

Fe(III) minerals in IFs

While hematite, magnetite and chert are the most abundant minerals currently found in IFs, iron hydroxides and a silica gel were likely the primary solid phases that precipitated out of ocean water during deposition (Klein 2005). Based on the REE composition, the original source of the dissolved iron was from hydrothermal vent fluid (Fryer 1983; Bau and Moller 1993). Iron was likely transported onto the continental shelves by intermittent upwelling currents (Klein and Beukes 1989). Three mechanisms have been proposed for the oxidation of ferrous iron to produce the ferric minerals in IFs, including: 1) the photochemical oxidation of ferrous iron by UV light (Equation 1.14); 2) the oxidation of ferrous iron by free oxygen in the environment, which was original produced by cyanobacteria using oxygenic photosynthesis (equation 15) and; 3) the

oxidation of ferrous iron by phototrophs using anoxygenic Fe-based photosynthesis (equation 16) (Koehler et al. 2010).

$$2\,Fe^{2+} + 6\,H_2O + \text{UV light} \rightarrow 2\,Fe(OH)_3 + 4\,H^+ + H_2 \quad (1.14)$$

$$4\,Fe^{2+} + O_2 + 10\,H_2O \rightarrow 4Fe(OH)_3 + 8\,H^+ \quad (1.15)$$

$$4\,Fe^{2+} + HCO_3^- + 10\,H_2O \rightarrow 4\,Fe(OH)_3 + CH_2O + 7\,H^+ \quad (1.16)$$

One of the first mechanisms proposed for IF deposition was the abiotic oxidation of iron by the high UV light present in the Archean (Cairns-Smith 1978; Francois 1986). However, laboratory studies have shown that ferrous iron oxidation by an high-UV, Archean-like environment precipitates out as greenalite or siderite before being photo-oxidized (Konhauser et al. 2007). The other two mechanisms proposed for the deposition of a IF are dependent on biological activity. Cloud (1973) originally hypothesized that oxygen produced by cyanobacteria was responsible for the oxidation of ferrous iron in an anoxic ocean. These cyanobacteria may have lived planktonically (Konhauser et al. 2005) or benthically as mats where by oxygen migrated from the oxygen oases to deeper marine environments before reacted with the ferrous iron (Beukes 2004). An association between cyanobacteria and IFs in the late Archean is supported by the presence of cyanobacterial biomarkers found within shales interbedded with BIF from the 2.78 to 2.45 Ga Mount Bruce Supergroup, Hamersley Basin (Brocks et al. 2003). However, this mechanism of iron oxidation is difficult to reconcile with presence of early to mid-Archean IFs, given that the geologic record suggests oxygenic photosynthesis only evolved by 2.7 Ga (Posth et al. 2011). Several researchers have proposed IFs could have been formed by anoxygenic Fe-phototrophs, that oxidized iron during photosynthesis (Ehrenreich and Widdel 1994; Kappler et al. 2005; Posth et al. 2008). In addition,

genetic analyses shows these Fe-phototrophs are a more ancient lineage than cyanobacteria (Xiong 2006). However, no geologic evidence of these Fe-phototrophs in the Archean currently exists (Posth et al. 2011).

Fe(II) minerals in IFs

Ferrous minerals in IFs could have been deposited as primary precipitation out of seawater, such as spheroidal siderite, or from diagenetic and metamorphic processes (Konhauser et al. 2005). Magnetite is the most common ferrous iron containing mineral in IFs and can account for up to a third of all the iron (Morris 1993). Magnetite may have been formed by a reaction between siderite and hematite during low-temperature metamorphism (Equation 1.17) but was more likely formed due to dissimilatory iron reduction by bacteria (Equation 1.4 combined with 18) (Konhauser et al. 2005).

$$Fe_2O_{3(s)} + FeCO_{3(s)} \rightarrow 4\,Fe_3O_{4(s)} + CO_2 \quad (1.17)$$

$$Fe^{2+} + 2\,Fe(OH)_3 + 2\,OH^- \rightarrow Fe_3O_{4(s)} + 4\,H_2O \quad (1.18)$$

The presence of carbonates containing depleted $\delta^{13}C$ in many IFs (Walker 1984) and magnetite overgrowths on hematite grains supports the precipitation of magnetite by FeRB (Morris 1993; Pecoits et al. 2009). The presence of heterotrophs in the iron-rich sediment during deposition may also explain why IFs contain very little organic carbon compared to other Archean marine sediments. For example, magnetite-rich BIFs from the Campbellrand carbonate platform in the Transvaal Supergroup have a very low average organic carbon content (0.012 wt%) compared to limestones (0.886 wt%), dolomites (0.523 wt%) and shales (3.91 wt%) of the same group (Klein 2005). Thus, redox cycling of carbon and iron by microorganisms may have been responsible for the formation of both ferrous and ferric minerals in IFs.

1.6 Chapter outlines

Both experiments in this thesis are centered on a laboratory model of a late Archean oxygen oasis containing cyanobacteria, aerobic heterotrophs, iron reducing bacteria (FeRB), sulphate reducing bacteria (SRB), and methanogens. The microbial mat was grown on forsterite sand in an 11.9 L airtight plexiglass chamber.

The focus of Chapter 2 is the geochemical transition from an anoxic to an oxygen-rich environment as the cyanobacterial mat grows. Forsterite ($Mg_{1.7}Fe_{0.3}SiO_4$) and fayalite (Fe_2SiO_4) were added as a mineral substrate for microbial attachment and as the sole source of iron in the experiment. This laboratory model started with an Archean-like atmosphere, high in $CO_{2(g)}$ and $CH_{4(g)}$. The research goals of this experiment were to**:** 1) examine the geochemical changes in the 'atmosphere', 'ocean' and pore water due to biologic growth and 2) to identify geochemical signatures of oxygen in mineral precipitates and biomarkers that could be preserved in the geologic record.

The focus of Chapter 3 is the interaction between ferrous iron and an oxygen oasis. In this experiment, 0.03 mM of ferrous iron was added daily to the surface water overlying the microbial mat; 0.03 mM is a low estimate for the amount of dissolved ferrous iron that was present in the Archean ocean (Canfield 2005). The research goals of this experiment were to: 1) determine how the microbial mat would responded to being slowly mineralized by iron and 2) to compare the iron minerals precipitated in the mat with Archean and Paleoproterozoic iron formations.

1.7 References

Altermann, W. and Kazmierczak, J. 2003. Archean microfossils: A reappraisal of early life on Earth. Research in Microbiology, **154**: 611-617.

Altermann, W., Kazmierczak, J., Oren, A., and Wright, D.T. 2006. Cyanobacterial calcification and its rock-building potential during 3.5 billion years of Earth history. Geobiology, **4**: 147-166.

Amores, D.R. and Warren, L.A. 2009. Metabolic patterning of biosilicification. Chemical Geology, **268**: 81-88.

Anbar, A.D. 2007. A whiff of oxygen before the Great Oxidation Event? Science, **317**: 1903-1906.

Arp, G., Reimer, A., and Reitner, J. 2001. Photosynthesis-induced biofilm calcification and calcium concentrations in Phanerozoic oceans. Science, **292**: 1701-1704.

Bach, W. and Edwards, K. 2003. Iron and sulfide oxidation within the basaltic ocean crust: Implications for chemolithoautotrophic microbial biomass production. Geochimica et Cosmochimica Acta, **67**: 3871-3887.

Bach, W., Paulick, H., Garrido, C.J., Ildefonse, B., Meurer, W.P., and Humphris, S.E. 2006. Unraveling the sequence of serpentinization reactions: Petrography, mineral chemistry, and petrophysics of serpentinites from MAR 15 ˚N (ODP leg 209, site 1274). Geophysical Research Letters, **33**: L13306.

Bapteste, E., Brochier, C., and Boucher, Y. 2005. Higher-level classification of the Archaea: Evolution of methanogenesis and methanogens. Archaea, **1**: 353-363.

Bau, M. and Moller, P. 1993. Rare-earth element systematics of the chemically precipitated component in early Precambrian iron formations and the evolution of the terrestrial atmosphere-hydrosphere-lithosphere system. Geochimica et Cosmochimica Acta, **57**: 2239-2249.

Bekker, A., Holland, H.D., Wang, P.L., Rumble, D., Stein, H.J., Hannah, J.L., Coetzee, L.L., and Beukes, N.J. 2004. Dating the rise of atmospheric oxygen. Nature, **427**: 117-120.

Beukes, N. 2004. Biogeochemistry - early options in photosynthesis. Nature, **431**: 522-523.

Beukes, N.J. and Gutzmer, J. 2008. Origin and paleoenvironmental significance of major iron formations at the Archean-Paleoproterozoic boundary. Society of Economic Geologists Reviews, **15**: 5-47.

Brasier, M., McLoughlin, N., Green, O., and Wacey, D. 2006. A fresh look at the fossil evidence for early Archaean cellular life. Philosophical Transactions of the Royal Society Biological Sciences, **361**: 887-902.

Brasier, M., Green, O., Jephcoat, A., Kleppe, A., Van Kranendonk, M., Lindsay, J., Steele, A., and Grassineau, N. 2002. Questioning the evidence for Earth's oldest fossils. Nature, **416**: 76-81.

Brazelton, W.J., Schrenk, M.O., Kelley, D.S., and Baross, J.A. 2006. Methane- and sulfur-metabolizing microbial communities dominate the Lost City hydrothermal field ecosystem. Applied and Environmental Microbiology, **72**: 6257-6270.

Brocks, J.J., Logan, G., Buick, R., and Summons, R.E. 1999. Archean molecular fossils and the early rise of eukaryotes. Science, **285**: 1033-1036.

Brocks, J.J., Buick, R., Summons, R.E., and Logan, G.A. 2003. A reconstruction of Archean biological diversity based on molecular fossils from the 2.78 to 2.45 billion-year-old Mount Bruce Supergroup, Hamersley Basin, Western Australia. Geochimica et Cosmochimica Acta, **67**: 4321-4335.

Buick, R. 1992. The antiquity of oxygenic photosynthesis: evidence from stromatolites in sulfate-deficient Archean lakes. Science, **255**: 74-77.

Cady, S. 2001. Paleobiology of the Archean. Archaea: Ancient Microbes, Extreme Environments, and the Origin of Life, **50**: 3-35.

Cairns-Smith, A.G. 1978. Precambrian solution photochemistry, inverse segregation, and banded iron formations. Nature, **276**: 807-808.

Canfield, D. 2005. The early history of atmospheric oxygen: Homage to Robert A. Garrels. Annual Review of Earth and Planetary Sciences, **33**: 1-36.

Canfield, D. and Raiswell, R. 1999. The evolution of the sulfur cycle. American Journal of Science, **299**: 697-723.

Canfield, D., Rosing, M.T., and Bjerrum, C. 2006. Early anaerobic metabolisms. Philosophical Transactions of the Royal Society Biological Sciences, **361**: 1819-1834.

Catling, D. and Claire, M. 2005. How Earth's atmosphere evolved to an oxic state: A status report. Earth and Planetary Science Letters, **237**: 1-20.

Catling, D., Zahnle, K., and McKay, C. 2001. Biogenic methane, hydrogen escape, and the irreversible oxidation of early Earth. Science, **293**: 839-843.

Cloud, P. 1973. Paleoecological significance of banded iron-formation. Economic Geology, **68**: 1135-1143.

Cohen, Y., Padan, E., and Shilo, M. 1975. Facultative anoxygenic photosynthesis in cyanobacterium *Oscillatoria limnetica*. Journal of Bacteriology, **123**: 855-861.

De Ronde, C., Channer, D., Faure, K., Bray, C., and Spooner, E. 1997. Fluid chemistry of Archean seafloor hydrothermal vents: Implications for the composition of circa 3.2 Ga seawater. Geochimica et Cosmochimica Acta, **61**: 4025-4042.

Ehrenreich, A. and Widdel, F. 1994. Anaerobic oxidation of ferrous iron by purple bacteria, a new-type of phototrophic metabolism. Applied and Environmental Microbiology, **60**: 4517-4526.

Eigenbrode, J.L. and Freeman, K.H. 2006. Late Archean rise of aerobic microbial ecosystems. Proceedings of the National Academy of Sciences, **103**: 15759-15764.

Eriksson, P., Mueller, W., and Tirsgaard, H. 1998. Precambrian clastic sedimentation systems. Sedimentary Geology, **120**: 1-4.

Farquhar, J., Bao, H.M., and Thiemens, M. 2000. Atmospheric influence of Earth's earliest sulfur cycle. Science, **289**: 756-758.

Farquhar, J., Zerkle, A.L., and Bekker, A. 2011. Geological constraints on the origin of oxygenic photosynthesis. Photosynthesis Research, **107**: 11-36.

Fennel, K., Follows, M., and Falkowski, P. 2005. The co-evolution of the nitrogen, carbon and oxygen cycles in the Proterozoic ocean. American Journal of Science, **305**: 526-545.

Foustoukos, D. and Seyfried, W. 2004. Hydrocarbons in hydrothermal vent fluids: The role of chromium-bearing catalysts. Science, **304**: 1002-1005.

Francois, L.M. 1986. Extensive deposition of banded iron formations was possible without photosynthesis. Nature, **320**: 352-354.

Frost, B.R. and Beard, J.S. 2007. On silica activity and serpentinization. Journal of Petrology, **48**: 1351-1368.

Fryer, B.J. 1983. Rare earth elements in iron-formation. *In* Iron-formation: facts and problems *Edited by* A.F. Trendall and R.C. Morris. Elsevier, Amsterdam, pp. 345-358.

Fryer, P. 2002. Recent studies of serpentinite occurrences in the oceans: Mantle-ocean interactions in the plate tectonic cycle. Chemie Der Erde-Geochemistry, **62**: 257-302.

Garrels, R.M. and Perry, E.A. 1974. Cycling of carbon, sulfur and oxygen through geological time. *In* The sea *Edited by* E.D. Goldberg. Wiley Interscience, New York, pp. 303-316.

Gross, G.A. 1980. A classification of iron formations based on depositional environments. The Canadian Mineralogist, **18**: 215-222.

Grotzinger, J.P. and Kasting, J.F. 1993. New constraints on Precambrian ocean composition. Journal of Geology, **101**: 235-243.

Habicht, K., Gade, M., Thamdrup, B., Berg, P., and Canfield, D. 2002. Calibration of sulfate levels in the Archean ocean. Science, **298**: 2372-2374.

Hayes, J. 1994. Global methanotrophy at the Archean-Proterozoic transition. *In* Early life on Earth: Nobel Symposium No. 84 *Edited by* S. Bengtson. Columbia University Press, New York, pp. 220-236.

Hofmann, H. 2000. Archean stromatolites as microbial archives. *In* Microbial Sediments *Edited by* R.E. Riding and S.M. Awramik. Springer, Berlin, pp. 315-327.

Hohmann-Marriott, M. and Blankenship, R.E. 2011. Evolution of photosynthesis. Annual Review of Plant Biology, **62**: 515-548.

Holland, H.D. 1978. The chemistry of the atmosphere and oceans. Wiley, New York.

Holland, H.D. and Kasting, J.F. 1992. The environment of the Archean earth. *In* The Proterozoic Earth *Edited by* J.W. Schopf and C. Klein. Cambridge University Press, Cambridge, pp. 21-23.

Holland, H.D. 2003. The geologic history of seawater. *In* Treatise on Geochemistry *Edited by* H.D. Holland and K.K. Turekian. Pergamon, Oxford, pp. 583-625.

Holland, H. 2002. Volcanic gases, black smokers, and the Great Oxidation Event. Geochimica et Cosmochimica Acta, **66**: 3811-3826.

James, H.L. 1983. Distribution of banded iron-formation in space and time. *In* Iron-formation: facts and problems *Edited by* A.F. Trendall and R.C. Morris. Elsevier, Amsterdam, pp. 471-490.

James, H.L. 1954. Sedimentary facies of iron-formation. Economic Geology, **49**: 235-293.

Kappler, A., Pasquero, C., Konhauser, K.O., and Newman, D.K. 2005. Deposition of banded iron formations by anoxygenic phototrophic Fe(II)-oxidizing bacteria. Geology, **33**: 865-868.

Kasting, J.F. 1993. Earth's early atmosphere. Science, **259**: 920-926.

Kasting, J. 2005. Methane and climate during the Precambrian era. Precambrian Research, **137**: 119-129.

Kelley, D., Karson, J., Blackman, D., Fruh-Green, G., Butterfield, D., Lilley, M., Olson, E., Schrenk, M., Roe, K., Lebon, G., Rivizzigno, P., and AT3-60 Shipboard Party. 2001. An off-axis hydrothermal vent field near the Mid-Atlantic Ridge at 30 degrees N. Nature, **412**: 145-149.

Kelley, D., Karson, J., Fruh-Green, G., Yoerger, D., Shank, T., Butterfield, D., Hayes, J., Schrenk, M., Olson, E., Proskurowski, G., Jakuba, M., Bradley, A., Larson, B., Ludwig, K., Glickson, D., Buckman, K., Bradley, A., Brazelton, W., Roe, K., Elend, M., Delacour, A., Bernasconi, S., Lilley, M., Baross, J., Summons, R., and Sylva, S. 2005. A serpentinite-hosted ecosystem: The Lost City hydrothermal field. Science, **307**: 1428-1434.

Kendall, B., Reinhard, C.T., Lyons, T., Kaufman, A.J., Poulton, S.W., and Anbar, A.D. 2010. Pervasive oxygenation along late Archaean ocean margins. Nature Geoscience, **3**: 647-652.

Kirschvink, J.L., Raub, T.D. and Fischer, W. 2012. Archean "whiffs of oxygen" go Poof! 22nd V.M. Goldschmidt Conference. Montreal, Canada.

Klein, C. 2005. Some Precambrian banded iron-formations (BIFs) from around the world: Their age, geologic setting, mineralogy, metamorphism, geochemistry, and origin. American Mineralogist, **90**: 1473-1499.

Klein, C. and Beukes, N.J. 1989. Geochemistry and sedimentology of a facies transition from limestone to iron-formation deposition in the early Proterozoic Transvaal Supergroup, South Africa. Economic Geology, **84**: 1733-1774.

Koehler, I., Konhauser, K., and Kappler, A. 2010. Role of microorganism in banded iron formations. *In* Geomicrobiology: Molecular and environmental perspective *Edited by* L.L. Barton, M. Mandl and A. Loy. Springer, Dordrecht, pp. 309-324.

Konhauser, K.O., Newman, D.K., and Kappler, A. 2005. The potential significance of microbial Fe(III) reduction during deposition of Precambrian banded iron formations. Geobiology, **3**: 167-177.

Konhauser, K., Phoenix, V., Bottrell, S., Adams, D., and Head, I. 2001. Microbial-silica interactions in Icelandic hot spring sinter: Possible analogues for some Precambrian siliceous stromatolites. Sedimentology, **48**: 415-433.

Konhauser, K.O., Amskold, L., Lalonde, S.V., Posth, N.R., Kappler, A., and Anbar, A. 2007. Decoupling photochemical Fe(II) oxidation from shallow-water BIF deposition. Earth and Planetary Science Letters, **258**: 87-100.

Konhauser, K.O., Pecoits, E., Lalonde, S.V., Papineau, D., Nisbet, E.G., Barley, M.E., Arndt, N.T., Zahnle, K., and Kamber, B.S. 2009. Oceanic nickel depletion and a methanogen famine before the Great Oxidation Event. Nature, **458**: 750-U85.

Konn, C., Charlou, J.L., Donval, J.P., Holm, N.G., Dehairs, F., and Bouillon, S. 2009. Hydrocarbons and oxidized organic compounds in hydrothermal fluids from Rainbow and Lost City ultramafic-hosted vents. Chemical Geology, **258**: 299-314.

Kump, L.R., Kasting, J.F., and Crane, R.G. 2004. The Earth system. Pearson Education, Inc., Upper Saddle River, New Jersey.

Lane, N., Allen, J.F., and Martin, W. 2010. How did LUCA make a living? Chemiosmosis in the origin of life. Bioessays, **32**: 271-280.

Lovley, D.R. 1991. Dissimilatory Fe(III) and Mn(IV) reduction. Microbiological reviews, **55**: 259-287.

Lovley, D.R. 2004. Potential role of dissimilatory iron reduction in the early evolution of microbial respiration. Springer Netherlands, .

Moody, J.B. 1976. Serpentinization: a review. Lithos, **9**: 125-138.

Morris, R.C. 1993. Genetic modelling for banded iron-formation of the Hamersley Group, Pilbara Craton, Western Australia. Precambrian Research, **60**: 243-286.

Neal, C. and Stanger, G. 1983. Hydrogen generation from mantle source rocks in Oman. Earth and Planetary Science Letters, **66**: 315-320.

Nealson, K.H. and Myers, C.R. 1990. Iron reduction by bacteria: A potential role in the genesis of banded iron formations. American Journal of Science, **290A**: 35-45.

Neubeck, A., Nguyen, T.D., Bastviken, D., Crill, P., and Holm, N.G. 2011. Formation of H_2 and CH_4 by weathering of olivine at temperatures between 30 and 70 ˚C. Geochemical Transactions, **12**: 6.

Nisbet, E.G. and Fowler, C.M.R. 1999. Archaean metabolic evolution of microbial mats. Proceedings of the Royal Society of London Biological Sciences, **266**: 2375-2382.

Pavlov, A. and Kasting, J. 2002. Mass-independent fractionation of sulfur isotopes in Archean sediments: Strong evidence for an anoxic Archean atmosphere. Astrobiology, **2**: 27-41.

Pecoits, E., Gingras, M.K., Barley, M.E., Kappler, A., Posth, N.R., and Konhauser, K.O. 2009. Petrography and geochemistry of the Dales Gorge banded iron formation: Paragenetic sequence, source and implications for palaeo-ocean chemistry. Precambrian Research, **172**: 163-187.

Phoenix, V., Adams, D., and Konhauser, K. 2000. Cyanobacterial viability during hydrothermal biomineralisation. Chemical Geology, **169**: 329-338.

Posth, N.R., Konhauser, K.O., and Kappler, A. 2011. Banded iron formations. *In* Encyclopedia of geobiology *Edited by* J. Reitner and V. Thiel. Springer, Dordrecht, The Netherlands, pp. 92-102.

Posth, N.R., Hegler, F., Konhauser, K.O., and Kappler, A. 2008. Alternating Si and Fe deposition caused by temperature fluctuations in Precambrian oceans. Nature Geoscience, **1**: 703-708.

Riding, R. 1982. Cyanophyte calcification and changes in ocean chemistry. Nature, **299**: 814-815.

Rosing, M.T., Bird, D.K., Sleep, N.H., and Bjerrum, C.J. 2010. No climate paradox under the faint early Sun. Nature, **464**: 744-747.

Russell, M.J., Hall, A.J., and Martin, W. 2010. Serpentinization as a source of energy at the origin of life. Geobiology, **8**: 355-371.

Schidlowski, M. 1987. Application of stable carbon isotopes to early biochemical evolution on Earth. Annual Review of Earth and Planetary Sciences, **15**: 47-72.

Schopf, J.W. 1993. Microfossils of the early Archean Apex Chert: New evidence of the antiquity of life. Science, **260**: 640-646.

Schopf, J.W., Kudryavtsev, A.B., Czaja, A.D., and Tripathi, A.B. 2007. Evidence of Archean life: Stromatolites and microfossils. Precambrian Research, **158**: 141-155.

Shen, Y., Buick, R., and Canfield, D. 2001. Isotopic evidence for microbial sulphate reduction in the early Archaean era. Nature, **410**: 77-81.

Shen, Y. and Buick, R. 2004. The antiquity of microbial sulfate reduction. Earth-Science Reviews, **64**: 243-272.

Simonson, B.M. and Goode, A.D.T. 1989. First discovery of ferruginous chert arenites in the early Precambrian Hamersley Group of Western Australia. Geology, **17**: 269-272.

Sleep, N., Meibom, A., Fridriksson, T., Coleman, R., and Bird, D. 2004. H_2-rich fluids from serpentinization: Geochemical and biotic implications. Proceedings of the National Academy of Sciences, **101**: 12818-12823.

Thode, H.G. and Goodwin, A.M. 1983. Further sulfur and carbon isotope studies of late Archean iron-formations of the Canadian shield and the rise of sulfate reducing bacteria. Precambrian Research, **20**: 337-356.

Trendall, A.F. 2002. The significance of iron-formation in the Precambrian stratigraphic record. *In* Precambrian sedimentary environments: A modern approach to ancient depositional systems *Edited by* W. Altermann and P.L. Corcoran. Blackwell Science, Oxford, pp. 33-66.

Ueno, Y., Yamada, K., Yoshida, N., Maruyama, S., and Isozaki, Y. 2006. Evidence from fluid inclusions for microbial methanogenesis in the early Archaean era. Nature, **440**: 516-519.

Vargas, M., Kashefi, K., Blunt-Harris, E., and Lovley, D.R. 1998. Microbiological evidence for Fe(III) reduction on early Earth. Nature, **395**: 65-67.

Veizer, J. 1988. The evolving exogenic cycle. *In* Chemical cycles in the evolution of the Earth *Edited by* B.C. Gregor, R.M. Garrels, F.T. Mackenzie and B.J. Maynard. Wiley-Interscience, New York, pp. 175-218.

Veizer, J., Hoefs, J., Lowe, D.R., and Thurston, P.C. 1989. Geochemistry of Precambrian carbonates: 2. Archean greenstone belts and Archean sea-water. Geochimica et Cosmochimica Acta, **53**: 859-871.

Wagner, M., Roger, A., Flax, J., Brusseau, G., and Stahl, D. 1998. Phylogeny of dissimilatory sulfite reductases supports an early origin of sulfate respiration. Journal of Bacteriology, **180**: 2975-2982.

Walker, J.C.G. 1984. Suboxic diagenesis in banded iron formations. Nature, **309**: 340-342.

Walter, M.R., Bauld, J., and Brock, T.D. 1972. Siliceous algal and bacterial stromatolites in hot spring and geyser effluents of Yellowstone National Park. Science, **178**: pp. 402-405.

Westall, F., Steele, A., Toporski, J., Walsh, M., Allen, C., Guidry, S., McKay, D., Gibson, E., and Chafetz, H. 2000. Polymeric substances and biofilms as biomarkers in terrestrial materials: Implications for extraterrestrial samples. Journal of Geophysical Research, **105**: 24511-24527.

Westall, F. 2004. Early life on Earth: The ancient fossil record. Springer Netherlands, .

Widdel, F., Schnell, S., Heising, S., Ehrenreich, A., Assmus, B., and Schink, B. 1993. Ferrous iron oxidation by anoxygenic phototrophic bacteria. Nature, **362**: 834-836.

Xiong, J. 2006. Photosynthesis: What color was its origin? Genome biology, **7**: 245.

Young, G.M. 1991. The geologic record of glaciation: Relevance to the climatic history of Earth. Geoscience Canada, **18**: 100-108.

Zahnle, K.J., Claire, M.W., and Catling, D.C. 2006. The loss of mass-independent fractionation of sulfur due to a Paleoproterozoic collapse of atmospheric methane. Geobiology, **4**: 271-283.

Chapter 2 A laboratory model of an Archean oxygen oasis

2.1 Introduction

Oxygenation in the late Archean

During the late Archean, oxygen was restricted to areas of high biological productivity where cyanobacteria were using oxygenic photosynthesis (Kasting 1993). Evidence from biomarkers (Brocks et al. 1999; Canfield and Raiswell 1999) and geochemical signatures (Kendall et al. 2010) show that oxygenic photosynthesis had evolved by 2.7 Ga. In contrast, atmospheric oxygen did not accumulate above 10^{-5} PAL until after 2.45 Ga (review of multiple lines of evidence in Holland 2011). As noted by Walker (1987), predicting the influence of oxygen Archean geochemical cycles is difficult as the biosphere appears upside down compared to the modern ocean. In the Archean, Earth's ocean and atmosphere were slightly reducing and the most oxidized chemical states were closely associated with photosynthetic microbial mats. The slow accumulation of oxygen over several hundred million years was dependent not only on the burial of organic carbon produced by oxygenic photosynthesis but also on the various oxygen sinks that were present (Catling et al. 2001). Oxygen sinks included but were not limited to reduced aqueous species, such as ferrous iron and sulphide, and reduced volcanic and metamorphic gases, such as SO_2, CH_4 and H_2 (Holland 2002). Not all geochemical processes occurring in an oxygen oasis would have been preserved in the geologic record, therefore, it is important to understand how a cyanobacterial mat possessing oxygenic photosynthesis will interact with a slightly reducing environment.

Model microbial systems

Numerous studies have used microbial mats to interpret preserved Archean biosignatures, including biominerals, molecular fossils, REE element ratios, and isotopic fractionations of C, S, N and Fe (Bebout et al. 2002). Cyanobacterial mats, both grown in the laboratory (Bebout et al. 2002; Bebout et al. 2004) and observed in the field (Hoehler et al. 2001) have been used to test hypotheses about Archean microbial-gas interactions. The study of modern stromatolites (*e.g.,* Reid et al. 2000) and the precipitation of carbonates in laboratory mats (Kuhl et al. 2003) has been important for interpreting the fossil record of stromatolites. This study is unique as it uses waters of similar salinity, but with a lower sulphate concentration than modern ocean water. It also employed diverse heterotrophic metabolic processes inoculated into the sediment, and an Archean-like atmosphere, with relatively high $CO_{2(g)}$ and $CH_{4(g)}$, was added above the mat surface.

2.2 Methods

Experimental design and abiotic additions

Experiments were performed in two 11 900 cm^3 air-tight plexiglass chambers. One chamber contained an oxygenic cyanobacterial mat plus iron reducing bacteria, sulphate reducing bacteria, and methanogens (OCM); the other chamber was an un-inoculated baseline for mineral-water interactions (BASE). Each chamber contained 3600 cm^3 of forsterite sand (Fo_{90}) plus artificial seawater in the pore space, five 3 cm^3 fayalite-magnetite mineral keys, 4700 cm^3 of artificial seawater above the sand and 3600 cm^3 of gaseous headspace (Figure 2.1). Sampling ports composed of a ball valve and

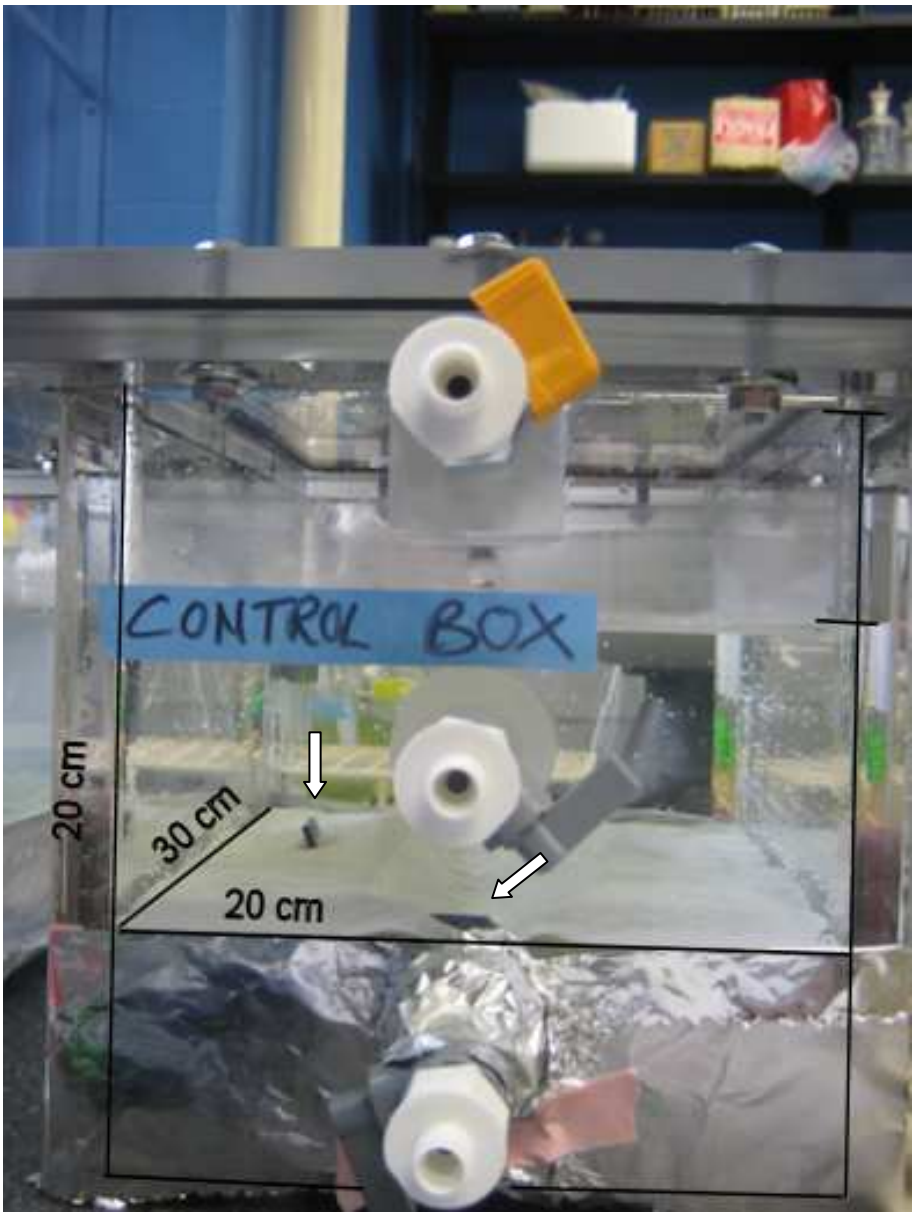

Figure 2.1 Dimensions and set up of airtight chamber with forsterite sand, fayalite mineral keys (white arrows), artificial seawater and low oxygen headspace.

13 mm septa (typically used on crimp top vials) were placed to sample the middle depth of the sediment pore water, surface water and atmosphere while maintaining the gas composition within the chamber during and between periods of sampling.

The forsterite sand was ordered from OptaMineral Inc. and is normally used as a foundry additive. Fusion x-ray fluorescence determined the chemical composition of the forsterite sand to be $Mg_{1.8}Fe_{0.2}SiO_4$ (Fo_{90}) (Table 2.1). Pressed pellet x-ray fluorescence (XRF) determined the forsterite had high concentrations of the trace elements of Cr (2350 ppm), Ni (2663 ppm) and Co (124 ppm) (Appendix A-1 for complete trace elements). XRF was completed by Biotron Analytical Laboratory at the University of Western Ontario, London, Canada. The forsterite sand had a relatively uniform grain size, between 75 and 212 μm (OptaMineral Inc.; Appendix A-2). Smaller, < 5 μm, forsterite grains were electrostatically attached to these larger grains. Some of the grains have more of these small grains attached, suggesting the forsterite had already undergone some alteration. The pore space was determined by weighting 10 ml of sand in a volumetric flask, filling the pore space with de-water and then re-weighting the flask. The pore water volume was measured twice and both times had a value of 36%.

In addition, five fayalite-magnetite mineral keys, sourced from the Forsythe Iron Mine, Quebec, Canada (Ward Scientific), were placed on top of and within the sand. These samples contained fayalite intergrown with magnetite plus minor components of pyrite and chalcopyrite, suggesting some serpentinization in the original rock had already occurred. The fayalite had a composition of $Fe_{1.8}Mg_{0.17}Mn_{0.03}SiO_4$ (Fo_8) (Kueber et al. 2006; Table 2.1). Pieces of the rock were cut into 5 mm thick, 6 cm^2 squares and were polished on one side.

Table 2.1 Major elemental composition of olivine sand and forsterite from fayalite-magnetite mineral keys (wt% oxide).

Element (wt%)	**Fo_{90} Optamineral sand (n=1) XRF (this study)**	**Fo_8 Ward sample from Forsyth Mine (n=2) EMPA (Kueber et al. 2006)**
SiO_2	42.35	29.62
TiO_2	0.01	< 0.06
Al_2O_3	0.07	< 0.04
Fe_2O_3	8.41	
FeO		65.64
MnO	0.11	0.94
MgO	47.46	3.32
CaO	0.23	< 0.03
K_2O	< 0.01	
Na_2O	< 0.01	
P_2O_5	0.01	
Cr_2O_3	0.38	< 0.11
LOI	0.75	
Total	**99.78**	**99.6**

Microbial cultures

Cyanobacteria, *Oscillatoria* sp., were originally collected from the Basque Lakes, British Columbia, Canada. The cyanobacteria were cultured in Erlenmeyer flasks containing 100 ml of an autoclaved mixture of artificial seawater (Harrison et al. 1980) and BG-11 media (Appendix B-1 and B-2). A fresh culture of cyanobacteria was started five weeks prior to the experiment. The cyanobacteria mat contained closely associated aerobic heterotrophs. Prior to the addition into the experiment, healthy mats were cut into 1 cm^2 pieces in a dish of seawater.

The *Shewanella oneidensis* MR-1 culture of FeRB was provided courtesy of Dr. Yuri Gorby and was stored in liquid nitrogen. Twenty hours prior to the start of the experiment, FeRB were cultured in a 100 ml autoclaved solution containing 3.01 g of Bacto Trypic Soy Broth.

The *Desulfovibrio* sp. culture of SRB was originally collected from the Basque Lakes, British Columbia, Canada (Foster et al. 2010) and was cultured in Postgate media in 15 ml crimp top vials. Four weeks prior to the experiment start, a fresh batch of SRB was cultured in a Postgate media modified to exclude iron and iron sulphides (Appendix B-3).

Methanococcus voltae, a methanogenic bacterium, was originally collected from an estuary in Florida and provide courtesy of Dr. Ken Jarrell. Methanogens were cultured in Balch media with a 20% CO_2/80% $H_{2(g)}$ head space, with 10 ml of media in a 100 ml crimp-top serum vial (Appendix B-4). Fresh cultures were started 2 to 3 weeks prior to being added to the experiment.

Microorganisms examined using scanning electron microscopy could be identified by species with some degree of confidence because the morphology of the bacteria in the culture has been characterized by previous researchers. Each known bacterial species added to the system were morphologically unique from each other. *Shewanella* sp. are rod-shaped; *Desulfovibrio* sp. are usually vibroid, sigmoid or spillrilloid; and *Methanococcus* sp. are coccoid (Bergey et al. 2001).

Using a Petroff Hausser counting chamber, microbial counts of each of the heterotrophic cultures were completed to add 10^6 cells of each culture per 1 cm^3 of forsterite sand in the OCM experiment (Appendix C). Microbial counts were completed by staining live cells with SYTO9 and dead cells with propidium iodide using the LIVE/DEAD BacLight Bacterial Viability Kit. Stains were made by mixing 3 µl each of SYTO9 and propidium iodide in 1 ml of de-ionized water. Then 180 µl of the stain was mixed with 20 µl of microbial culture and reacted for 15 minutes. Ten µl of this mixture was placed on a Petroff Hauser counting chamber and examined under a florescence microscope (Zeiss Axio Imager Z1 microscope) at 40x magnification.

FeRB trapped in biofilm were difficult to count, thus microbial counts were only done on planktonic FeRB cells. As such, reported FeRB concentrations are only a minimum for the added concentration of FeRB. In addition, all methanogen cells fluoresced both red and green in all samples. Red florescence is most likely due to florescence of resazurin in the Balch mixture, in addition to the propidium iodine stain. During growth, bacteria can convert resazurin in the cell to its fluorescent reduced state (Shiloh et al. 1997). Thus red florescence by the methanogens could indicate either cell death or cell metabolic activity. As such, 50% of the total methanogens counted were

assumed to be viable to determine a concentration of live methanogens to add to the experiment. This is reasonable given than methanogens are unable to tolerate oxygen and are more sensitive than SRB or FeRB, and therefore, are more likely to die during the experimental set up.

Before the experiment, forsterite sand was not sterilized. The sand could not be sterilized in an autoclave because the steam and high temperature would have oxidized the iron in the forsterite and perhaps would have induced some serpentinization. The sand could not be chemically sterilized as this would have left a chemical residue that would have affected microbial growth during the experiment. However, an agar plate test of uninoculated sand determined that the sand contained very low numbers of aerobic and anaerobic bacteria. In this test, 0.1 g of forsterite sand was sprinkled onto triplicate R2A agar plates and cultured for 7 days. Triplicate anaerobic plates were cultured in an anaerobic jar using an BD GasPak EZ anaerobic sachet to remove $O_{2(g)}$ and increase $CO_{2(g)}$. After 7 days no colony forming units (CFU) were detected on the 3 anaerobic plates. One of the aerobic plates had two CFU and the other aerobic plates had no CFU. This plate test suggests approximately 10 aerobic heterotrophs/g forsterite sand were added to both experiments.

Experimental set-up

The plexiglass chamber and all mineral components were washed before starting the experiment. The plexiglass chambers were washed with de-ionized water and Sparkleen detergent (Fisher Scientific), rinsed three times in sterile deionized water and then air-dried. The fayalite-magnetite mineral keys soaked in ethanol for approx. 1 hour,

sonicated in ethanol for 15 minutes and then air-dried overnight. The forsterite sand was rinsed three times in anoxic artificial seawater (0.1 g ascorbic acid/L).

In setting up the chamber, 3600 cm^3 of the wet forsterite sand was packed into the bottom of the chamber. Four fayalite-magnetite minerals keys were placed at the top of the sand and one was placed at least 2 cm deep into the sand. Five hundred millilitres of anoxic seawater (0.2 g ascorbic acid/L) was then poured onto the sand. In the OCM experiment, three 1 cm^2 pieces of cyanobacterial mat were placed in the shallow pool of water. Then the lid of the chamber was sealed and the headspace was flushed for 5 minutes with 100% N_2 gas through the top two sampling ports. In the OCM experiment, 50 ml of methanogens, 18 ml of SRB and 30 ml FeRB were added through the middle sampling port, producing a cell concentration of approx. 10^6 cells/cm^3 in the sediment (Appendix C). Then 4.7 L of filtered anoxic seawater (0.1 g ascorbic acid/L) containing 1/100 dilute BG-11 media was added through chamber sampling ports, while trying to maintain the 100% N_2 atmosphere. Because the 1 cm^2 cyanobacterial mats became covered in sand during the addition of seawater, 15 ml slurry of loose cyanobacteria was also added to the OCM experiment. The chamber was then flushed again with 100% N_2 for 5 minutes through the top two valves. After fitting 11 mm airtight septa in front of the valves, 18 ml of 20% CO_2/80% $N_{2(g)}$ and 3.6 ml of 100% $CH_{4(g)}$ was added to the headspace with a gas tight syringe (Hamilton Company).

At day 7, the BASE experiment had a much higher $O_{2(g)}$ concentration than the OCM experiment, over 9% O_2 compared to less than 0.2% O_2, due to a slow leakage around the lid of the BASE chamber. As such the BASE atmospheric composition was re-started by opening and then successfully resealing the lid of the chamber. The BASE

headspace was then flushed with 100% $N_{2(g)}$ for 5 minutes and 18 ml of 20% CO_2/80% $N_{2(g)}$ was added with a gas tight syringe; 100% $CH_{4(g)}$ was not re-added. The OCM experiment was not modified at day 7. As a result of the leakage, the OCM experiment was run for 110 days and the BASE experiment was run for 117 days.

Gas analysis

Gas samples of the OCM and BASE chambers were taken weekly to determine the influence of microbial growth on the gas chemistry. Samples were collected and analyzed in triplicate. The concentrations of $O_{2(g)}$, $CO_{2(g)}$, $CH_{4(g)}$ and $H_{2(g)}$ determined using micro-gas chromatography (μGC) with a Mole Sieve 5A and a Plot U column (Hewlett Packard Micro-GC P 200 with Aglent Cerity software). Gas samples were transferred to the μGC in fifteen millilitre crimp top vials with butyl stoppers that had been flushed for 2 minutes with 100% $He_{(g)}$ at 13 kPa through two 25 gauge needles. Using a 22 gauge flame sterilized cannula and 1 ml gas tight syringe with sample lock (Model 1001; Hamilton Company), 2 ml of atmosphere was removed from the chamber through gas sampling port and was injected into the 15 ml vial. Samples were taken from the vial by pulling each gas sample through a 25 gauge needle into the μGC. The μGC was calibrated with a laboratory standard composed of 1% each of $H_{2(g)}$, $O_{2(g)}$, $N_{2(g)}$, $CH_{4(g)}$, $CO_{(g)}$, and $CO_{2(g)}$. Reported gas concentrations were multiplied by a dilution factor, 7.05, to determine the gas concentration in the experiment. All calculations used the ideal gas law. Only 1 sample out of more than 100 had an obvious major leakage of atmospheric oxygen into the vial and thus was removed from the analysis.

Samples of 100% $He_{(g)}$ in the 15 ml crimp top vials were analyzed at every time point to determine the average leakage of oxygen into the sample vials. Fifteen millilitre

vials flushed with 100% $He_{(g)}$ had $O_{2(g)}$ values between 61 to 3374 ppm, with an average value of 642 ppm. This leakage into the 100% $He_{(g)}$ flushed vials was not accounted for in experimental samples. This experimental procedure could not accurately determine oxygen concentrations below 0.25 % or carbon dioxide concentrations below 100 ppm.

Aqueous chemistry analysis

Samples of both the surface and pore water were collected weekly. To eliminate water trapped in the sampling port, 5 ml of water was removed and discarded using a sterile 25 gauge needle and 10 ml syringe. Then 18 ml of water was taken as sample using a new sterile 25 gauge needle and 30 ml syringe. To determine the dissolved oxygen concentration, 4 ml of sample was immediately placed in a 7 ml shell vial and a 1-8 ppm ChemMets dissolved oxygen ampoule was broken into the sample. After mixing the sample in the ampoule the colour of the solution was compared to a 1-8 ppm ChemMets dissolved oxygen reference kit. Two ml of sample was used to determine pH using pH strips with a range of 6.5-10. The remaining 12 ml of sample was filtered through a 0.2 or 0.45 μm membrane into a falcon tube and stored in the fridge until hydrogeochemical analysis could be completed. Cation concentrations were determined using ion coupled plasma atomic emission spectrometry (ICP-AES) (Perkin-Elmer Optima 3300DV) and phosphate and sulphate concentrations were determined using ion cathode spectrometry (IC) (Dionex IC-3000) at the Biotron Analytical Laboratory, University of Western Ontario, London, Canada.

Mat and sediment sampling

Biological and mineralogical samples were only collected at the end of the experiment. From the OCM experiment, pieces of cyanobacteria mat, fayalite-magnetite

mineral keys and forsterite sand were removed using autoclaved scoopulas and tweezers and sterile pipettes. All samples were fixed in an anoxic solution of 2% glutaraldehyde and 20 mM HEPES buffer adjusted to pH 8.2. Small samples were stored in 15 ml crimp top vials under 100% $N_{2(g)}$. Fayalite-magnetite mineral keys covered in the glutaraldehyde solution were stored in an anaerobic jar with a BD GasPak EZ anaerobic sachet.

To produce whole mount scanning electron microscopy (SEM) images, samples were dehydrated with ethanol, 25%, 50%, 75%, 100%, 100%, and 100% ethanol each for 15 minutes. Then samples were filtered on to a 0.45 μm membrane and critical point dried (Samdri PVT 3B critical point drier, Tousimis Research). Once dry, samples were attached to a SEM stub with carbon tape and were coated with 5 nm of osmium in an osmium plasma coater (Filgen Plasma Coater 80T) to prevent electrical charging of the sample. Samples were imaged at 3 kV on a Leo Ziess 1530 SEM. Imaging (3 kV) and elemental analysis (10 kV) was also done on Leo Ziess 1540 SEM with a INCA x-sight energy dispersive spectrophotometer (EDS) (Oxford Instruments). Electrons counts from EDS are not quantitative and only show the presence or absence of a specific element. All imaging was completed at the University of Western Ontario Nanofabrication Facility.

Geochemical modeling

Aqueous geochemical equilibria were determined using the computer model PHREEQC version 2.18 (Parkhurst and Appelo 1999). Geochemical model parameters followed the procedure of Hellevang et al. (2011). The model used thermodynamic data from the phreeqc.dat database with additional thermodynamic constants sourced from

phreeqc llnl.dat database for forsterite (Mg_2SiO_4), fayalite (Fe_2SiO_4), magnetite (Fe_3O_4), brucite ($Mg(OH)_2$), diopside ($CaMgSiO_6$), magnesite ($MgCO_3$) and hydromagnesite ($Mg_5(CO_3)_4(OH)_2 \cdot 4H_2O$). The forsterite sand ($Fo_{90}$) was modeled as a solid solution with 90% pure forsterite and 10% pure fayalite. The modeling did not consider biologically mediated reactions, adsorption-desorption reactions or reactions with organic carbon. Serpentinization was not modeled as a surface limited reaction. The concentration of species in the model solution was based on calculated additions to the chamber and geochemical results (Appendix D-1).

Abiotic forsterite serpentinization

To determine the morphology of abiotically serpentinized forsterite grains, a small-scale experiment was conducted in three 20 ml crimp top vials. 10 g of forsterite sand was washed and vortexed twelve times in filtered artificial seawater and then washed three times in 100% ethanol. Samples were then sonicated for 15 minutes in 100% ethanol and 15 minutes in artificial seawater. Finally samples were washed three times in seawater, sonicated in seawater for an additional 15 minutes and then sealed under anoxic seawater in a crimp top vial with no headspace for 112 days. At the end of the experiment, samples were fixed in 2% glutaraldehyde and then processed and imaged using the same procedure as used for the OCM and BASE solid samples.

2.3 Results

Atmospheric change in baseline experiment (BASE)

The BASE atmospheric composition was restarted at day 7 because of a leakage around the lid. For six weeks, $O_{2(g)}$ in the baseline experiment was below 0.3% but at

week 8, an unintentional break in the chamber seal increased $O_{2(g)}$ to 1.9% (Figure 2.2). By week 11, $O_{2(g)}$ decreased to below 0.3% again and then from week 12 to 17 $O_{2(g)}$ slowly increased up to 1.3%. In the first two weeks, $CO_{2(g)}$ in the BASE experiment decreased from 738 ppm to 474 ppm. From week 3 to 12, $CO_{2(g)}$ fluctuated between 357 and 557 ppm and then $CO_{2(g)}$ increased from 390 ppm at week 12 to 1095 ppm at the end of the experiment (Figure 2.3). After week 5, $H_{2(g)}$ was detected in the BASE atmosphere for the remainder of the experiment. $H_{2(g)}$ concentrations ranging between 3000 and 8000 ppm (Figure 2.4). The μGC was likely not sensitive to $H_{2(g)}$ values below 425 ppm (equivalent to 3000 ppm in experiment) and had a large amount of error.

Atmospheric change in cyanobacteria mat experiment (OCM)

At the beginning of the experiment rapid changes in the OCM gas composition occurred. In the first day $O_{2(g)}$ decreased from 0.55% to below 0.20% and remained low for the first week. Also in the first week, $CH_{4(g)}$ decreased from 8582 to 579 ppm and $CO_{2(g)}$ increased from 1308 ppm to 7783 ppm (Figure 2.3).

For the remainder of the experiment further changes, but at a slower rate, occurred in the OCM atmosphere. $O_{2(g)}$ increased to 0.40% by day 12 and to 0.73% by week 4 and then increased rapidly between weeks 5 and 10, climbing from 1.4% to 10.2%. (Figure 2.2). After week 10, $O_{2(g)}$ ranged between 9.4 and 12.9%. From week 1 to 4, $CO_{2(g)}$ decreased from 7783 ppm to 124 ppm and then remained below 110 ppm after week 5 (Figure 2.3). After the rapid change in the first week, $CH_{4(g)}$ fluctuated between 579 and

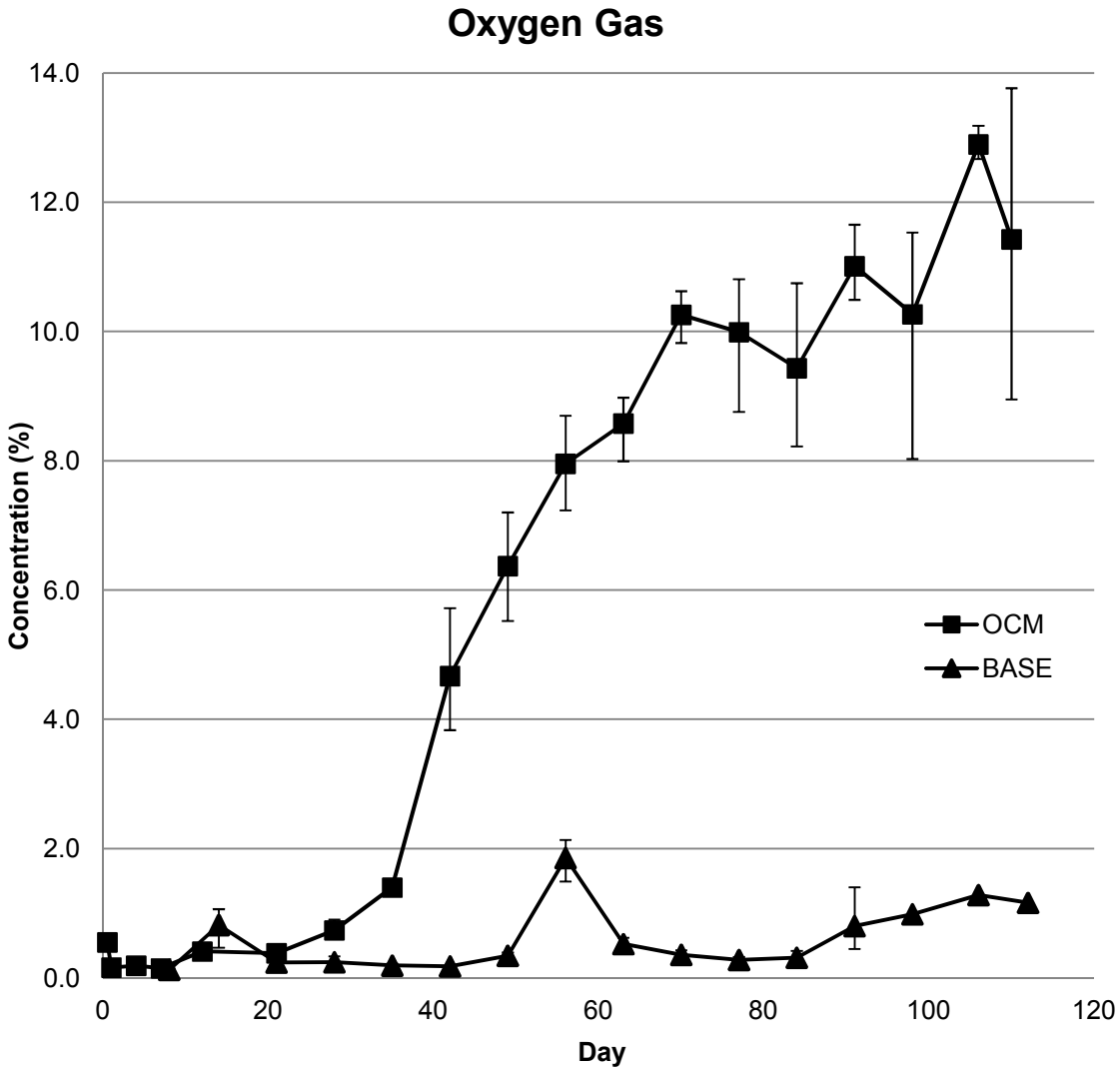

Figure 2.2 Atmospheric oxygen concentrations in the oxygenic cyanobacterial mat experiment (OCM) and baseline for water-mineral interactions experiment (BASE). The BASE atmosphere was restarted at day 7 after a leak in the lid was found. Error bars show minimum and maximum values.

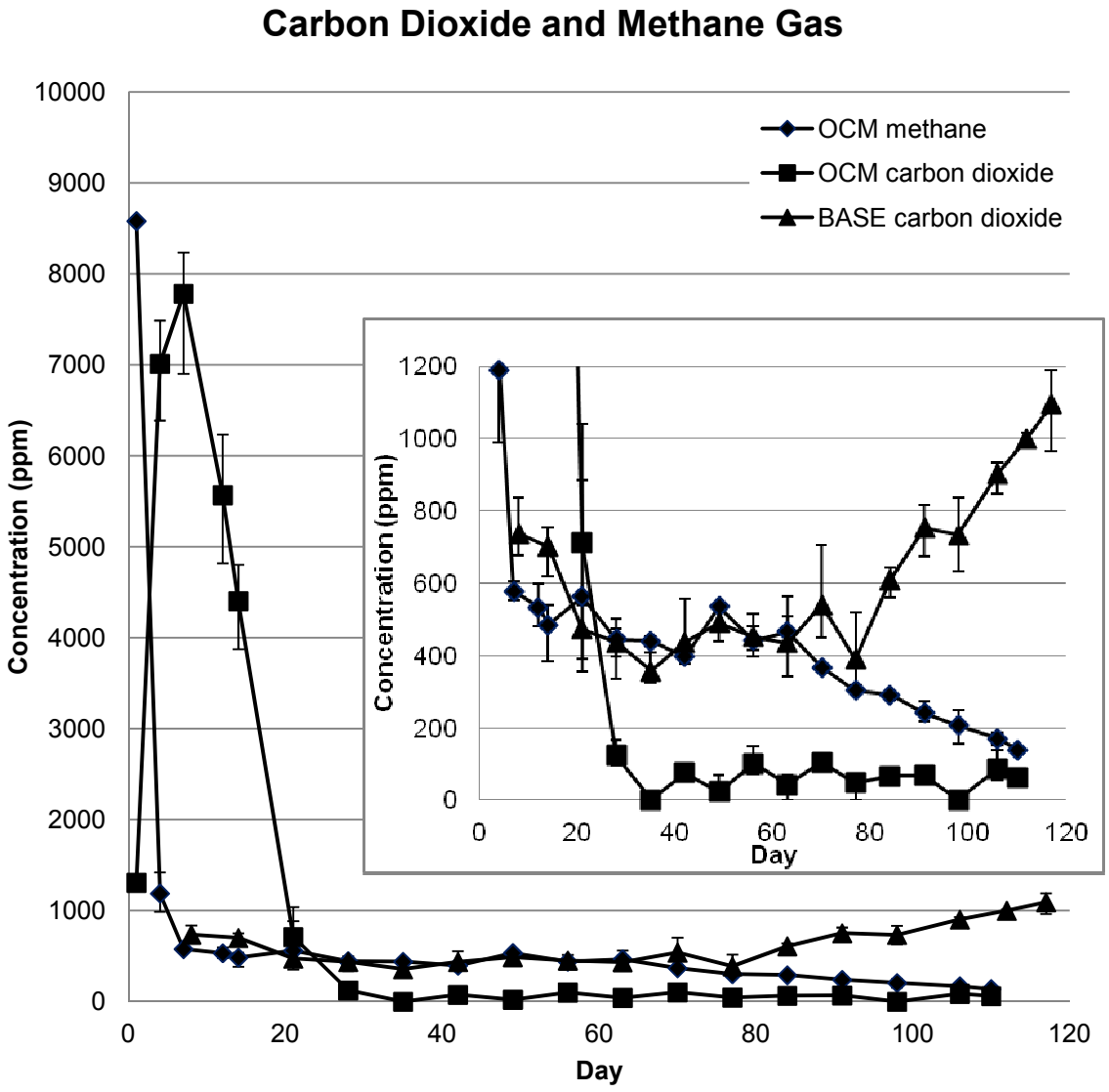

Figure 2.3 Atmospheric carbon dioxide and methane concentrations in OCM and carbon dioxide concentration in BASE. Methane was not added to the BASE experiment after restarting the atmosphere at day 7. Insert shows change in gas composition when concentration was less than 1200 ppm. Error bars show minimum and maximum values.

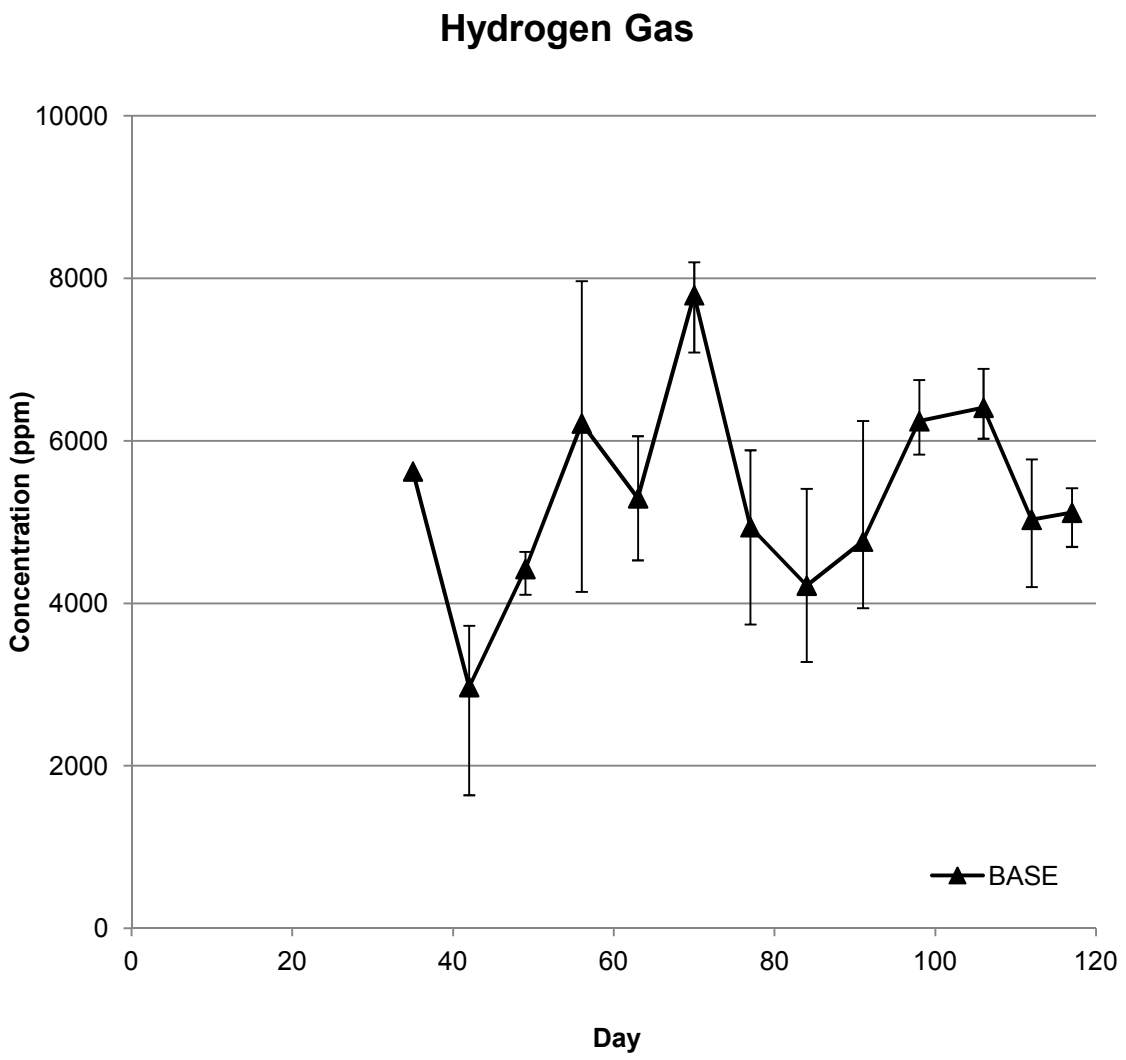

Figure 2.4 Hydrogen concentration in the BASE headspace. No hydrogen was detected in the OCM chamber.

397 ppm for eight weeks then slowly decreased to 140 ppm by the end of the experiment (Figure 2.3).

Dissolved oxygen

The BASE pore and surface water started with a dissolved oxygen concentration of 1.5 ppm. For the remainder of the experiment both pore and surface water had a dissolved oxygen concentration of < 1 ppm, with the exception of the week 8 (1.5 ppm), one week after the leak. In the first four weeks, the dissolved oxygen concentration of the OCM surface water increased from 1 to 3.5 ppm and then for the remainder of the experiment the concentration fluctuated between 3 and 4 ppm (Figure 2.5). The OCM pore water dissolved oxygen concentration increased to 2 ppm by week 2, fluctuated between 2 and 3 ppm between week 2 and 9 and then remained at 2 ppm.

pH

In the BASE experiment, the pore and surface water pH fluctuated around pH 8.0 for the first four weeks then remained almost constant at pH 8.1 (Figure 2.6). In the OCM experiment, pore and surface water pH dropped from 8.0 to 6.8 in the first two weeks. From week 2 to 4, OCM surface water pH increased from 6.8 to 9.0 and OCM pore water pH increased from 6.8 to 8.7. By week 6, OCM surface water pH increased to 9.5 and remained at 9.5 for the remainder of the experiment. Pore water pH increased to 9.0 by week 7 and then slowly decreased to be 8.5 at the end of the experiment.

Silica and iron

The seawater added to the experiments had a silica concentration of < 0.4 μM. At the end of the experiment, silica in the BASE surface water (49.9 μM) was much higher

than the OCM surface water (4.6 μM). Both the BASE pore water, 88.3 μM, and the OCM pore water, 61.2 μM, had higher dissolved silica than the surface water.

While the added artificial seawater had < 0.2 μM dissolved iron, both the BASE and OCM experiments had elevated iron concentrations in the pore water of at day 1: 11.9 and 7.9 μM respectively. In the BASE experiment both the pore water and surface dissolved iron increased between week 1 to 7 and then decreased after week 7. The pore water iron increased from 3.8 to 6.3 μM then decreased to 4.3 μM and surface water dissolved iron increased from 0.8 to 10.5 μM and then decreased to 6.1 μM (Figure 2.7). In the OCM pore water, iron concentrations increased in the first week from 7.8 to 10.0 μM and then rapidly decreased to below 0.2 μM by week 4. OCM surface water iron concentrations increased from 1.5 μM at the start of the experiment to 15.5 μM by week 2 and then decreased to below 0.1 μM by week 5.

Sulphate and phosphate

At day 1 the OCM and BASE pore water sulphate was high (0.81 and 0.50 mM, respectively) and surface water sulphate was low (0.20 and 0.01 mM, respectively). From added microbial media, total S in the OCM experiment should have been ~1.5 mmol, or 0.265 mM. As the BASE experiment was not inoculated with microbial cultures in their media, initial sulphate concentrations should have been lower. In both the BASE and OCM experiments, the pore and surface water converged toward single values as the experiment ran, 0.21 mM in the BASE experiment and 0.23 mM in the OCM experiment (Figure 2.8).

In the BASE experiment, dissolved phosphate started at 0.46 mM in the surface water and dropped to 0.05 mM by week 8 (Figure 2.9). Phosphate concentrations in the

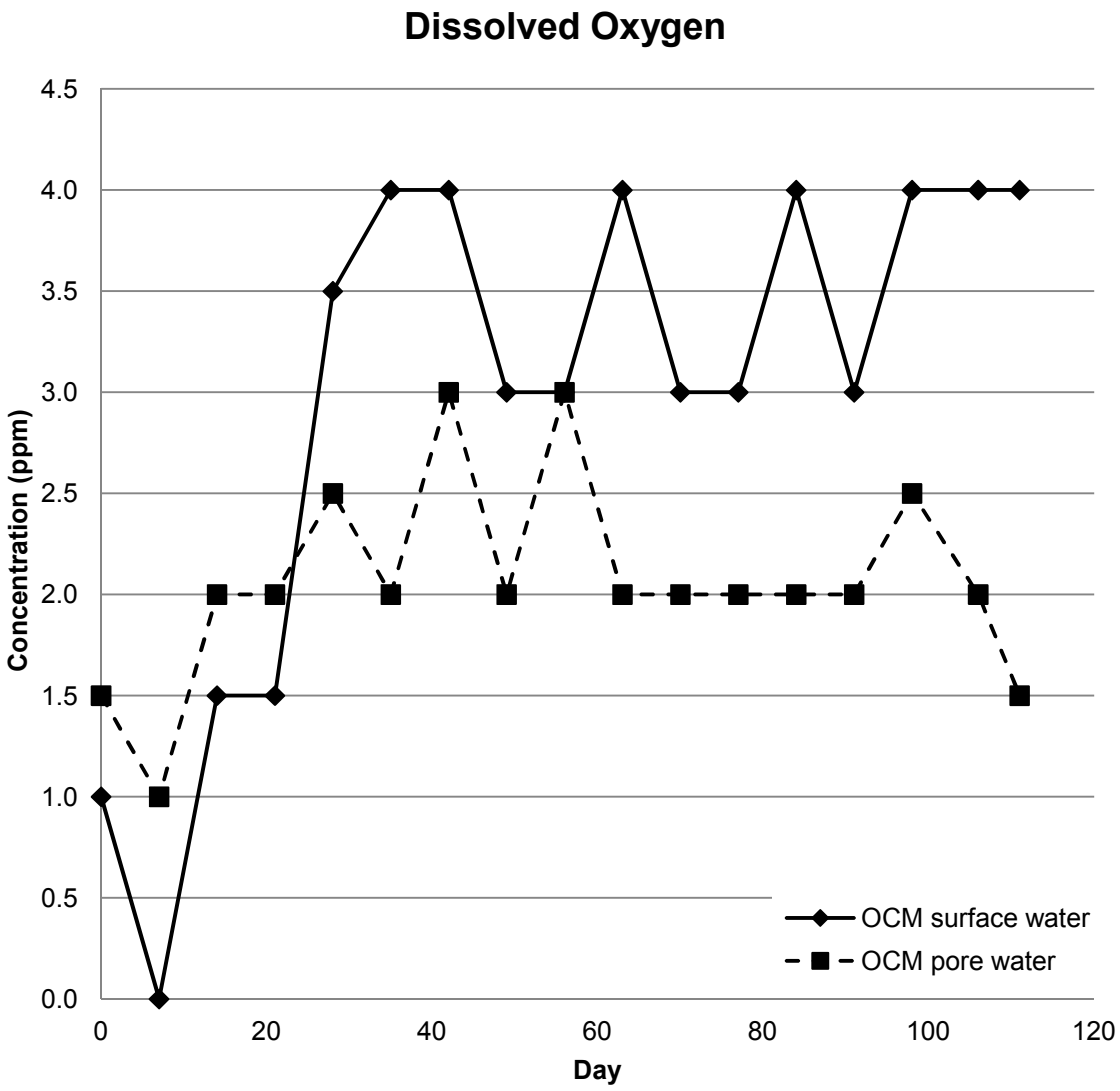

Figure 2.5 Dissolved oxygen in pore and surface water of OCM experiment. In the BASE experiment, pore and surface water dissolved oxygen was 1.5 ppm at the start of the experiment and then mostly remained below 1 ppm (the detection limit) until the end of the experiment.

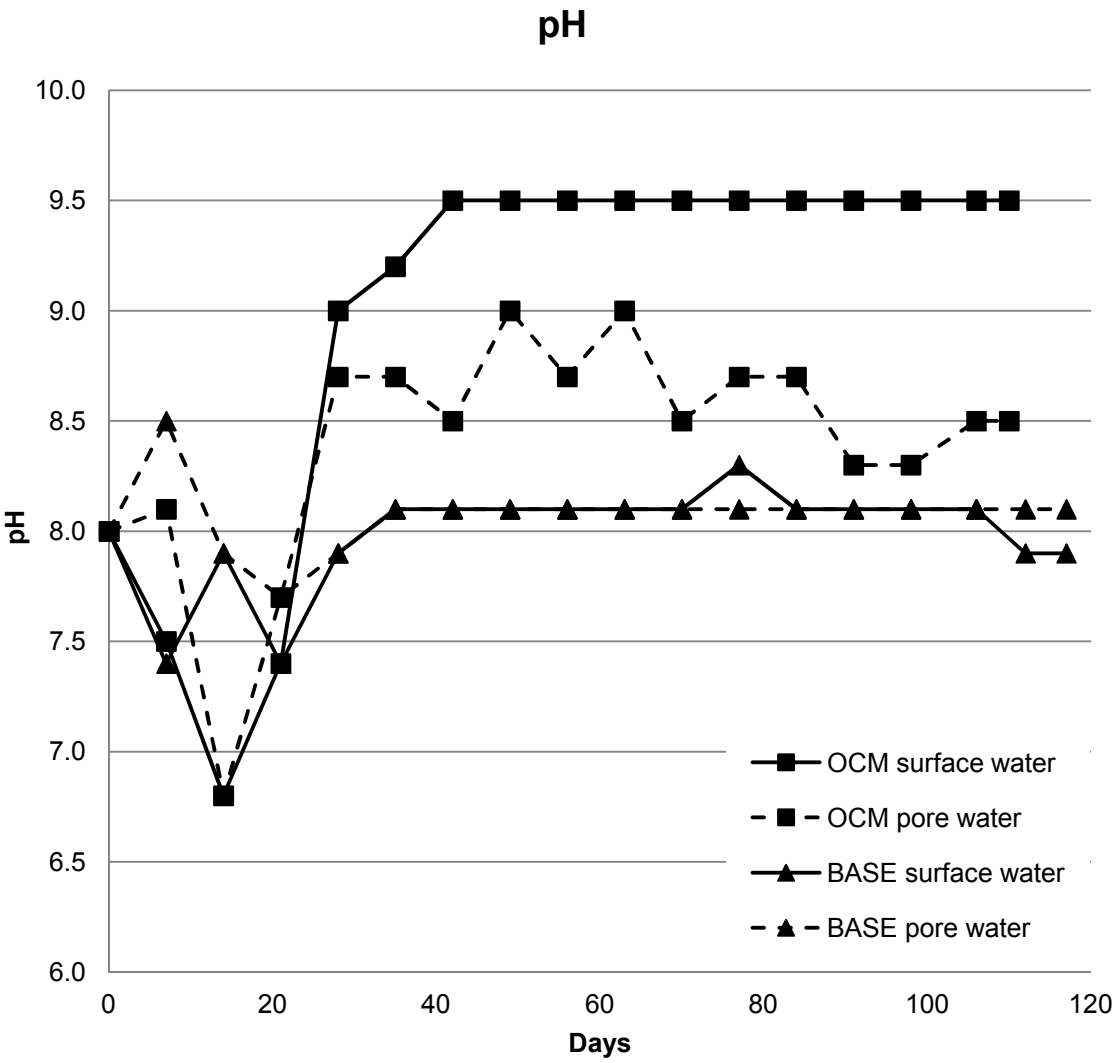

Figure 2.6 pH of pore and surface water in the OCM and BASE experiments.

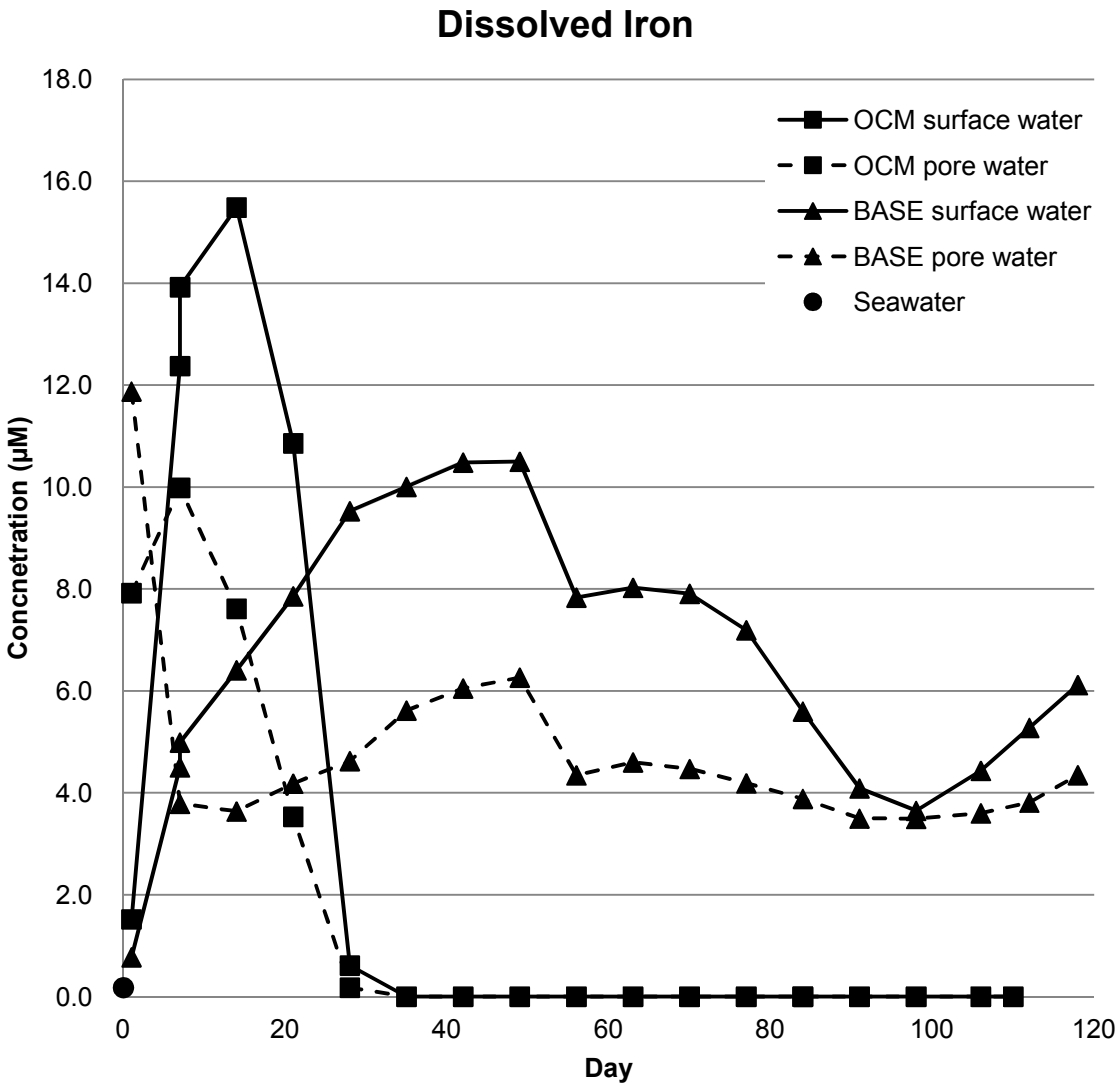

Figure 2.7 Dissolved iron in the pore and surface water in the OCM and BASE experiments.

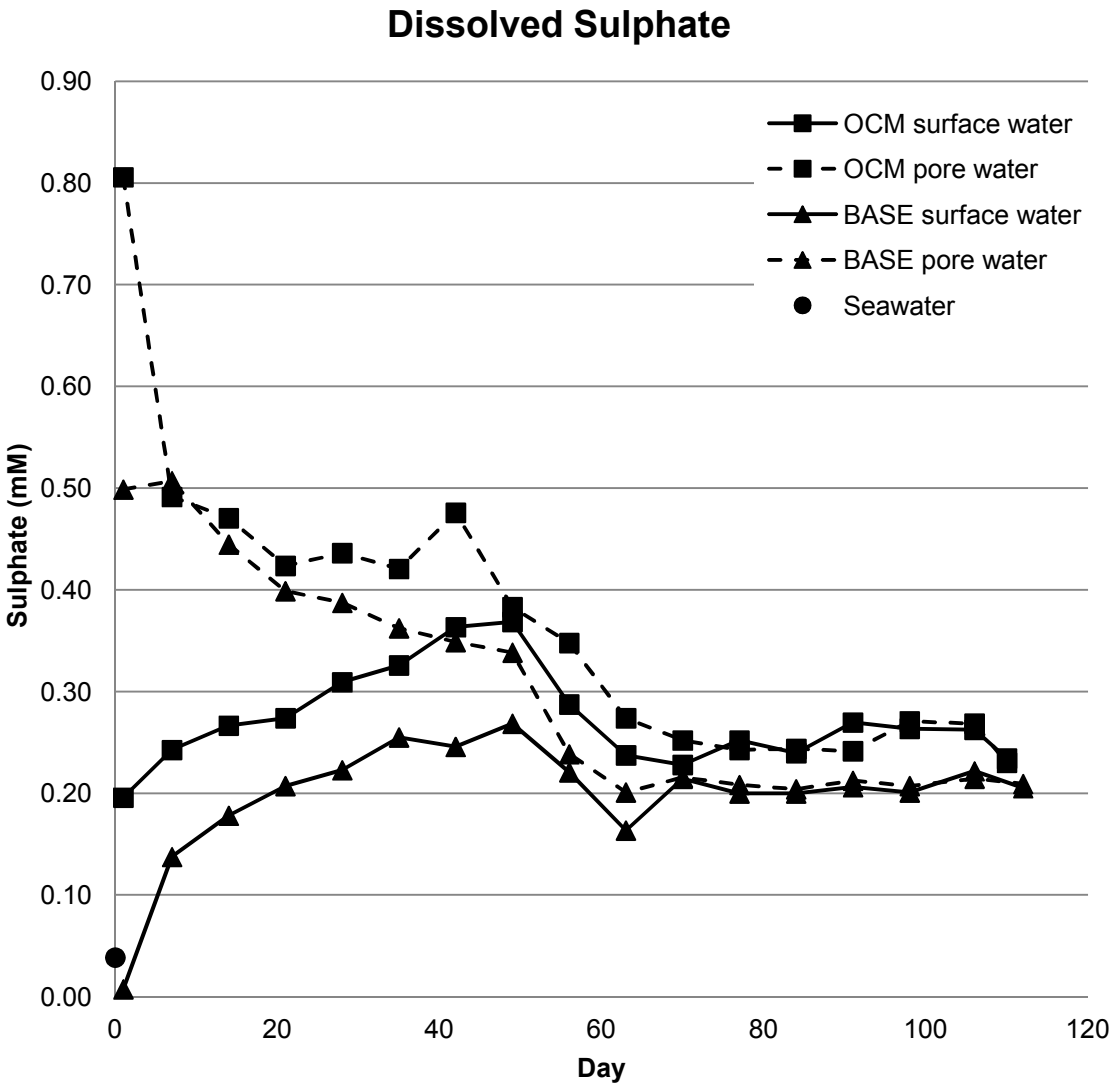

Figure 2.8 Dissolved sulphate in the pore and surface water in the OCM and BASE experiments.

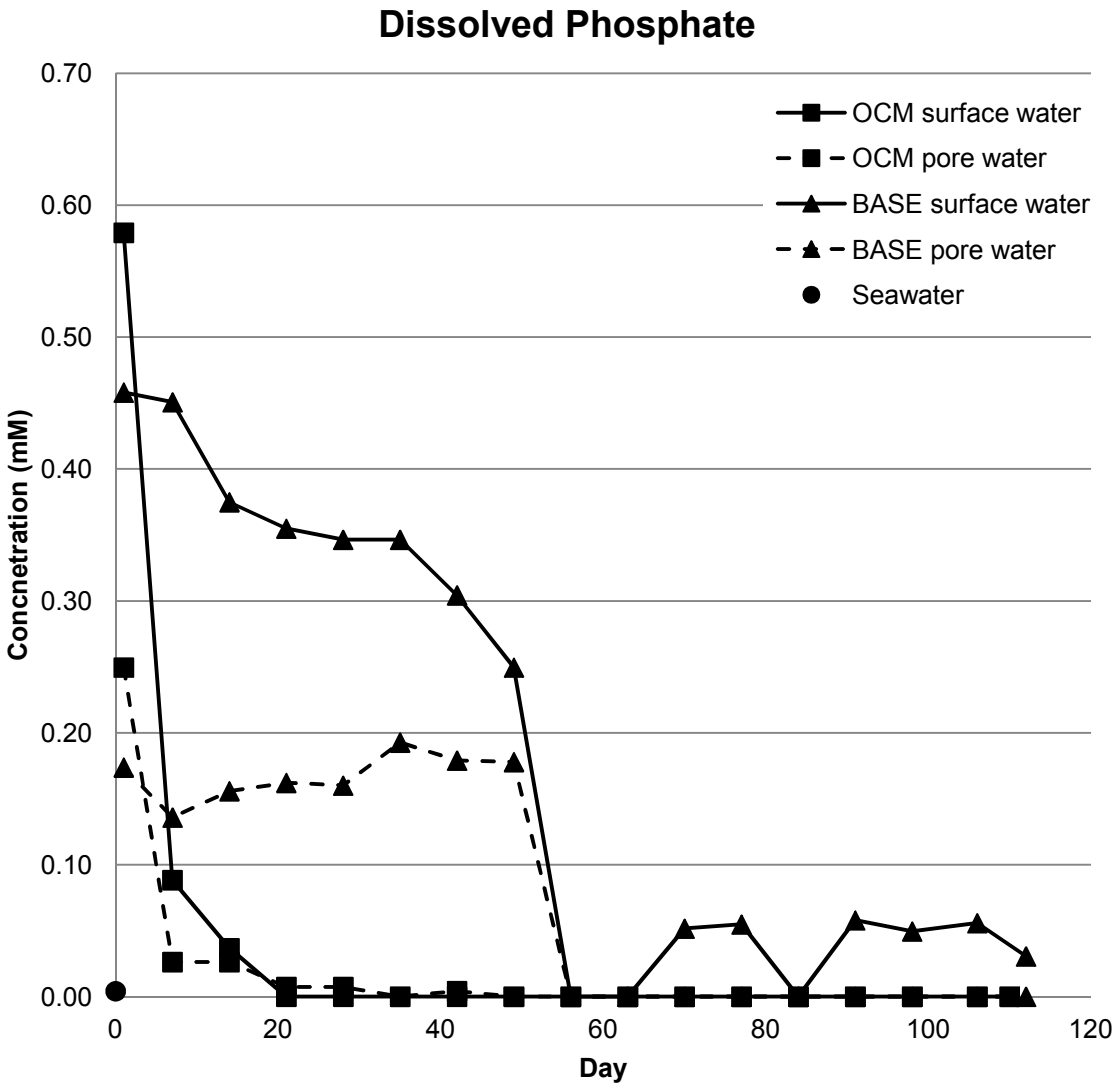

Figure 2.9 Dissolved phosphate in the pore and surface water in the OCM and BASE experiments.

surface water started at 0.58 mM in the OCM experiment and dropped to below detection (0.004 mM) within the first three weeks.

Mineral-aqueous phase equilibrium

At the end of the experiments both the OCM and BASE surface waters were saturated with respect to calcite ($CaCO_3$), aragonite ($CaCO_3$), dolomite ($CaMg(CO_3)_2$), magnesite ($MgCO_3$), chrysotile ($Mg_3Si_2O_5(OH)_4$) and talc ($Mg_3Si_4O_{10}(OH)_2$) (Appendix D-2). The OCM surface water was also saturated with respect to hydromagnesite ($Mg_5(CO_3)_4(OH)_2 \cdot 4H_2O$), brucite ($Mg(OH)_2$), and sepiolite ($Mg_2Si_3O_{7.7}OH \cdot 3H_2O$) whereas BASE surface water was not.

A batch run model in PHREEQC of the solid, aqueous and gaseous components of the experiment showed serpentinization and the formation of $H_{2(g)}$ and $CH_{4(g)}$ was thermodynamically favourable (Appendix D-3). Based on differences in the amount of dissolved oxygen and thus the aqueous phase redox potential at the end of the BASE and OCM experiments, the model showed that at equilibrium, 30 times more $H_{2(g)}$ could be produced in the BASE system.

Abiotic and BASE mineral alteration

The forsterite sand added to the experiments contained some fine-grained minerals but little alteration (Figure 2.10a). Forsterite sand grains in the small scale abiotic serpentinization experiment showed various types of alteration of the mineral surface occurred (Fig. 2.10b-g). Some forsterite grains developed polygons (Figure 2.10d), rills or an egg carton-like surface (Figure 2.10e). Other grains accumulated abundant fine-grained (< 5 μm) mineral precipitates on the surface including rod, platy and blocky grains (Figure 2.10b and 2.10f). Rarely, some grains developed 0.5 μm platy

rosettes on the mineral surface (Figure 2.10g). Large and small scale splitting of some of the forsterite grains also occurred resulting in disintegration of the grain (Figure 2.10b and 2.10c).

The added fayalite-magnetite keys were polished, and as such, had no surface alteration but did have some small scratches (Figure 2.11a). In the BASE experiment, the fayalite-magnetite keys showed macroscopic surface alteration. At week 8, the top surface of one of the fayalite-magnetite mineral keys turned red due to precipitation of iron (oxy)hydroxides. SEM showed surface of the fayalite-magnetite mineral key was covered in abundant platy Mg-silicates where the mineral key sat above the forsterite sand (Figure 2.11c). Bacteria, most of them rod shaped, were seen attached to this fayalite-magnetite surface and to the phyllosilicates coating the fayalite-magnetite key (Fig 2.11d). The maximum bacterial density observed was 5 cells/10 μm^2. Pieces of fayalite-magnetite buried below the sand had cracks in the mineral surface but fewer bacteria and phyllosilicates attached (Figure 2.11b). No bacteria were observed on the BASE forsterite sand.

OCM experiment mat structure, microbial diversity and mineral alteration

By week 2 of the OCM experiment, the cyanobacteria had rapidly grown to cover the forsterite sand with a thin biofilm. In the next few weeks, thick 1 cm diameter hemispherical nodes of cyanobacteria appeared on the thin mat and by week 5 an approximately 1 mm thick cyanobacterial mat covered most of the sand. Cyanobacteria also grew up and down the sides of the plexiglass chamber. In addition to a thick cyanobacteria mat on the sand surface, a discontinuous cyanobacterial pellicle formed on the water surface by week 3. The pellicle contained trapped forsterite sand grains and gas

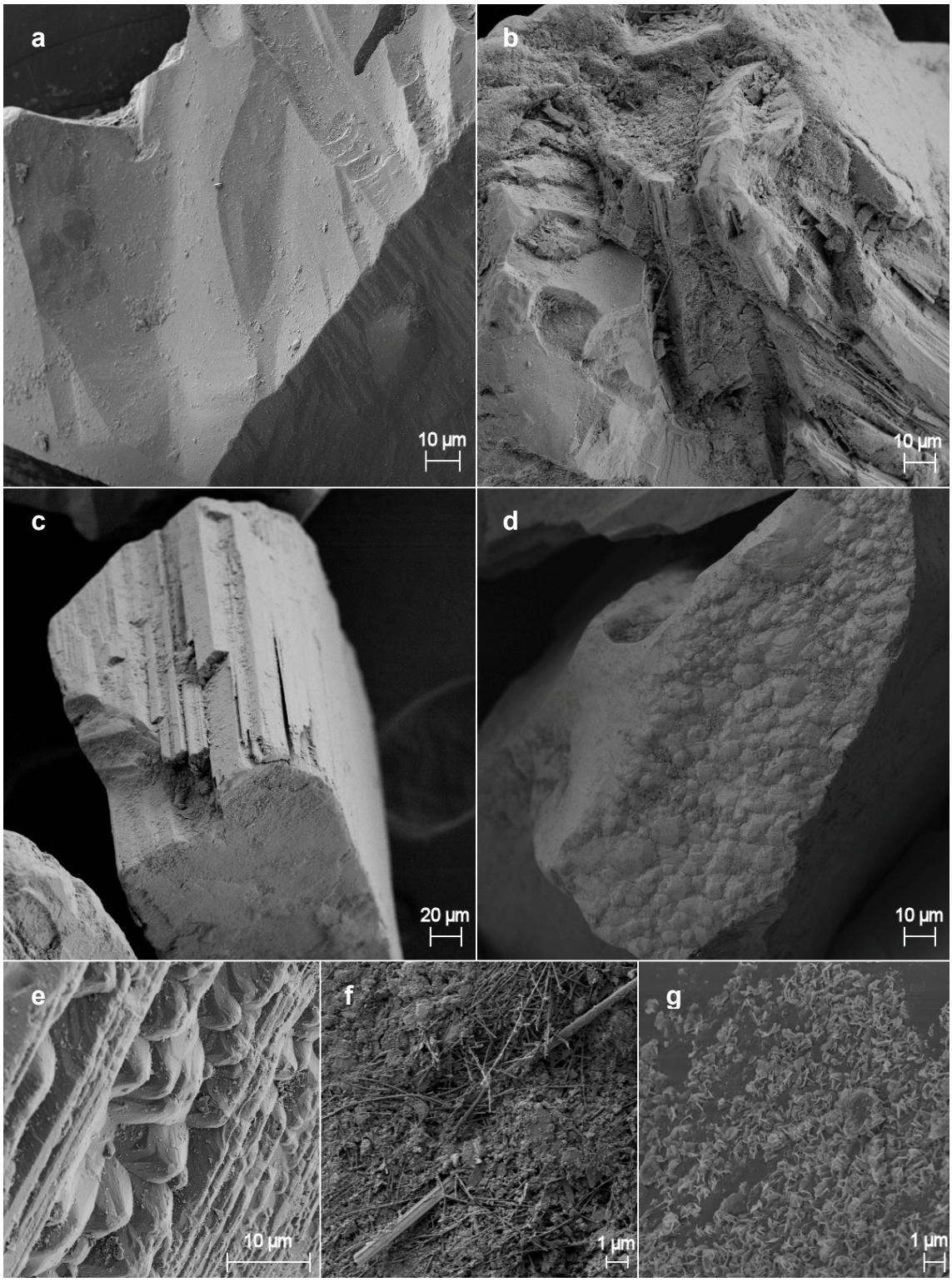

Figure 2.10 a) Unreacted forsterite sand. The forsterite reacted in the small-scale abiotic serpentinization experiment resulted in **b)** abundant < 1 µm precipitates **c)** splitting of the forsterite grains, **d)** formation of polygons, **e)** grooves, **f)** precipitation of rod-shaped minerals, and **g)** precipitation of < 1 µm platy rosettes.

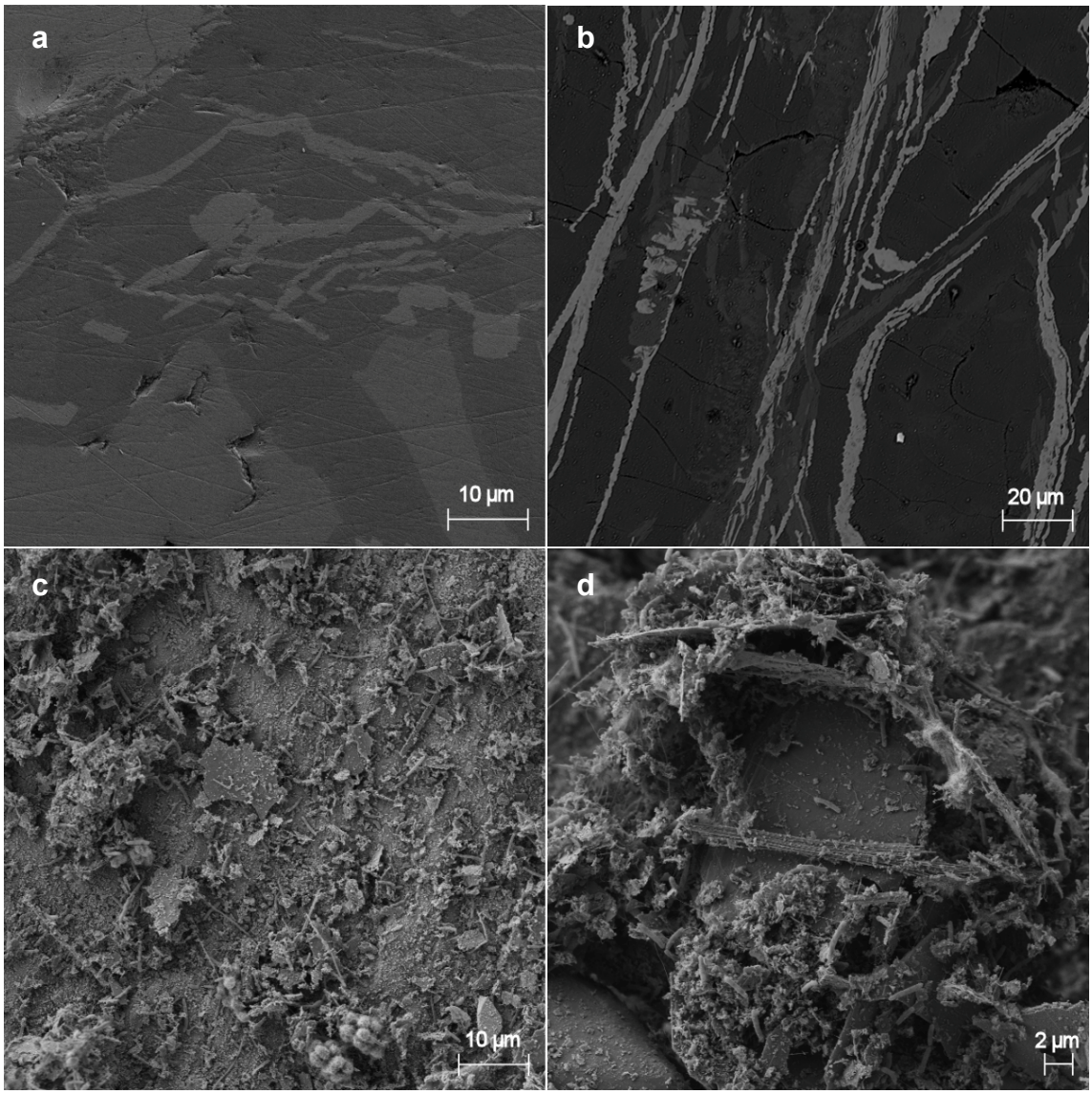

Figure 2.11 a) A polished but un-reacted fayalite-magnetite mineral key. **(b-d)** Fayalite-magnetite mineral keys placed in BASE experiment. **b)** Fayalite (dark) intergrown with magnetite (light) from serpentinization in the original host rock shown using a back scatter electron detector. Dark lines are cracks in the mineral surface. **c)** Mg-silicates and bacteria attached to the top of a fayalite-magnetite key above fosterite sand. An average of 5 cells/10 μm^2 were counted in this photomicrograph. **d)** Close up of Mg-silicate fibers, precipitates and organics on fayalite-magnetite key above fosterite sand.

bubbles. Sampling at the end of the OCM experiment showed that the mat had several unique features in different areas of the chamber. Under the mat, most of the forsterite sand appeared to be unaltered macroscopically but in one area the sand had turned from green to red. In another area close to where the heterotrophs had been injected into the experiment, a black sulphide spot formed under the mat.

SEM showed that some sections of mat were relatively thin and contained few secondary minerals, while other areas contained abundant smaller (< 20 μm) grains of forsterite and secondary minerals trapped in the biofilm (Fig 2.12a and 2.12b). The cyanobacterial mat contained heterotrophs with coccoid, rod, and vibriod morphologies. Secondary minerals (< 10 μm) had a crystal structure of either plates or rods (Figure 2.12c). Abundant < 1 μm-scale minerals with various morphologies were also seen attached to some of the forsterite sand grains (Figure 2.12d). More rarely, the large forsterite grains had surface alteration in the form of pit marks (Figure 2.12d). SEM-EDS showed that all of these minerals had a Mg-silicate geochemical signature (Figure 2.13a). A sample of mat taken from the sulphide spot at the centre of the chamber had an SEM-EDS signal that include S and Ca, as well as the signal of the Mg-silicates (Figure 2.13b).

Minerals without a Mg-silicate geochemical signature were found in a few select locations. One sample of mat contained abundant 1 μm rosette minerals with a very low concentration of Si relative to Mg (Figure 2.14a and 2.14b). Some of the rosettes contained Mn, which was an element not found in other parts of the mat, with up to a 1:1 mole ratio of Mg to Mn. Ca was also detected in some of the rosettes. The mineral precipitates trapped in the cyanobacterial EPS of the pellicle also had the geochemical signature of a carbonate, with very low concentrations of Si relative to Mg and some Mn

and Ca (Figure 2.14c). However, the carbonates in the pellicle had a much smaller grain size, < 0.5 μm, and a blocky texture compared to the carbonates on the sand surface (Figure 2.14d). The pellicle also contained large (75 - 210 μm) and small (< 5 μm) forsterite grains but no heterotrophs were found. Fine-grained, 0.2 μm plates on the surface of some large forsterite grains were similar to the grains in the small-scale abiotic experiment (similar to Figure 2.10g).

The diversity and abundance of heterotrophs in the cyanobacteria mat varied greatly. Most of the mat had a relatively low numbers of heterotrophs and most of the cells were attached to forsterite surface. However, the cyanobacterial mat surrounding the fayalite-magnetite mineral keys (Figure 2.15a) and the mat covering the red, thus likely oxidized, forsterite sand both contained numerous heterotrophs. Pieces of fayalite-magnetite mineral key sitting above the sand surface had an average heterotroph density of ~23 cells/10 μm^2 attached to the forsterite-magnetite surface (Figure 2.15b). In addition, many more heterotrophs were trapped in the EPS above the fayalite-magnetite surface. SEM-EDS showed that rod-shaped cells and EPS adjacent to the fayalite-magnetite mineral key had mineralized or adsorbed iron, which was not seen more distal mat.

Pieces of the fayalite-magnetite key sitting within the sand had a patchwork pattern of cells depending on where the forsterite sand grain touched the mineral key (Fig 2.15c). Organic matter covered the mineral surface to a depth of at least 2.5 mm. Cell had either rod or spirillum morphologies. Dense areas of heterotrophs contained more than 50 cells/10 μm^2 and some less dense areas had only a few cells/10 μm^2. Most of the

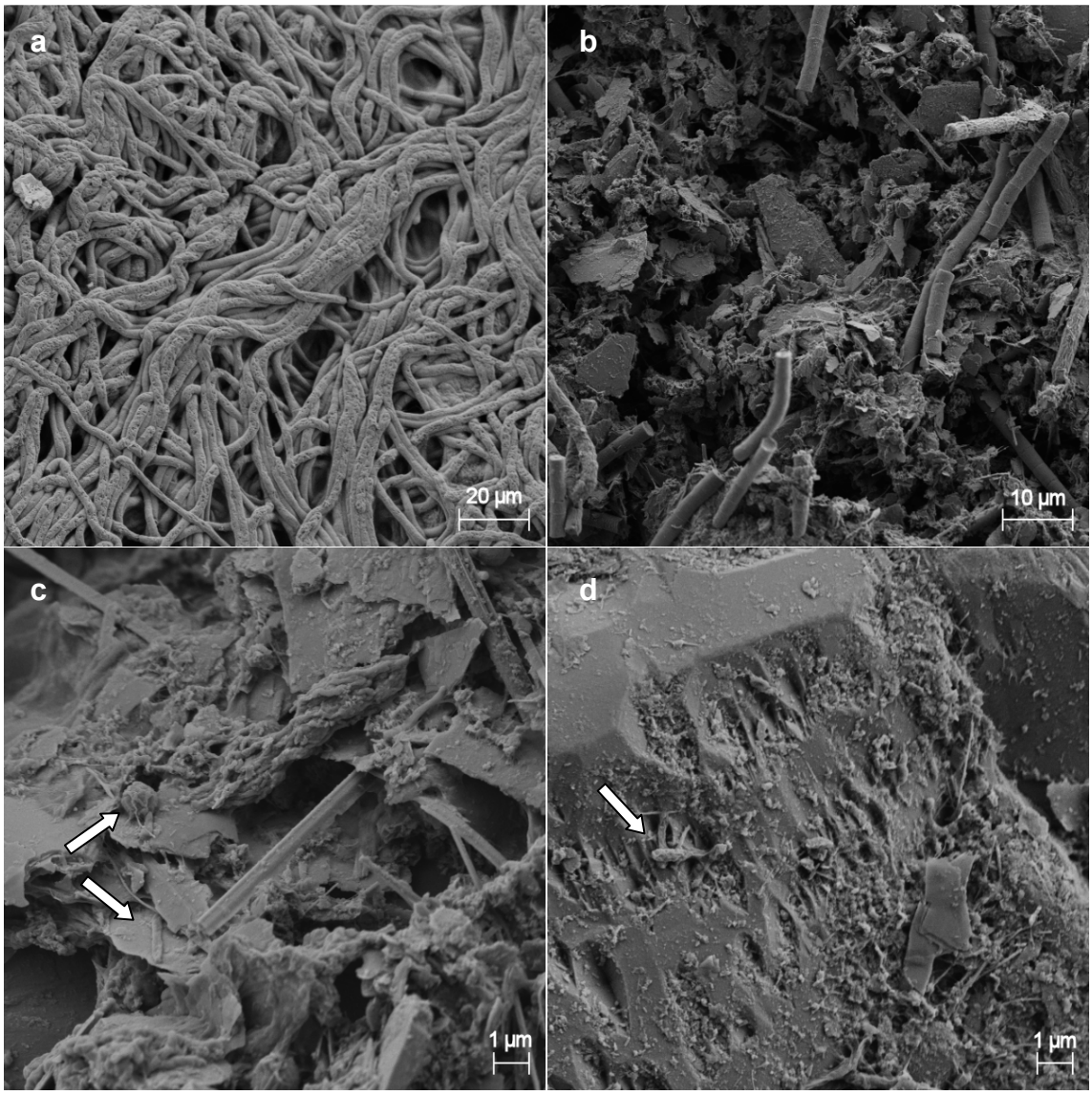

Figure 2.12 Cyanobacteria, bacteria (arrows) and minerals from the mat on the OCM forsterite sand surface. **a)** Top of cyanobacterial mat showing *Oscillatoria* sp. and extracellular polymeric substance (EPS). **b)** Plate and rod- shaped minerals trapped in cyanobacterial mat. **c)** Close up of Mg-silicate minerals, heterotrophs and EPS. **d)** Fine mineral precipitates and pit marks in forsterite sand.

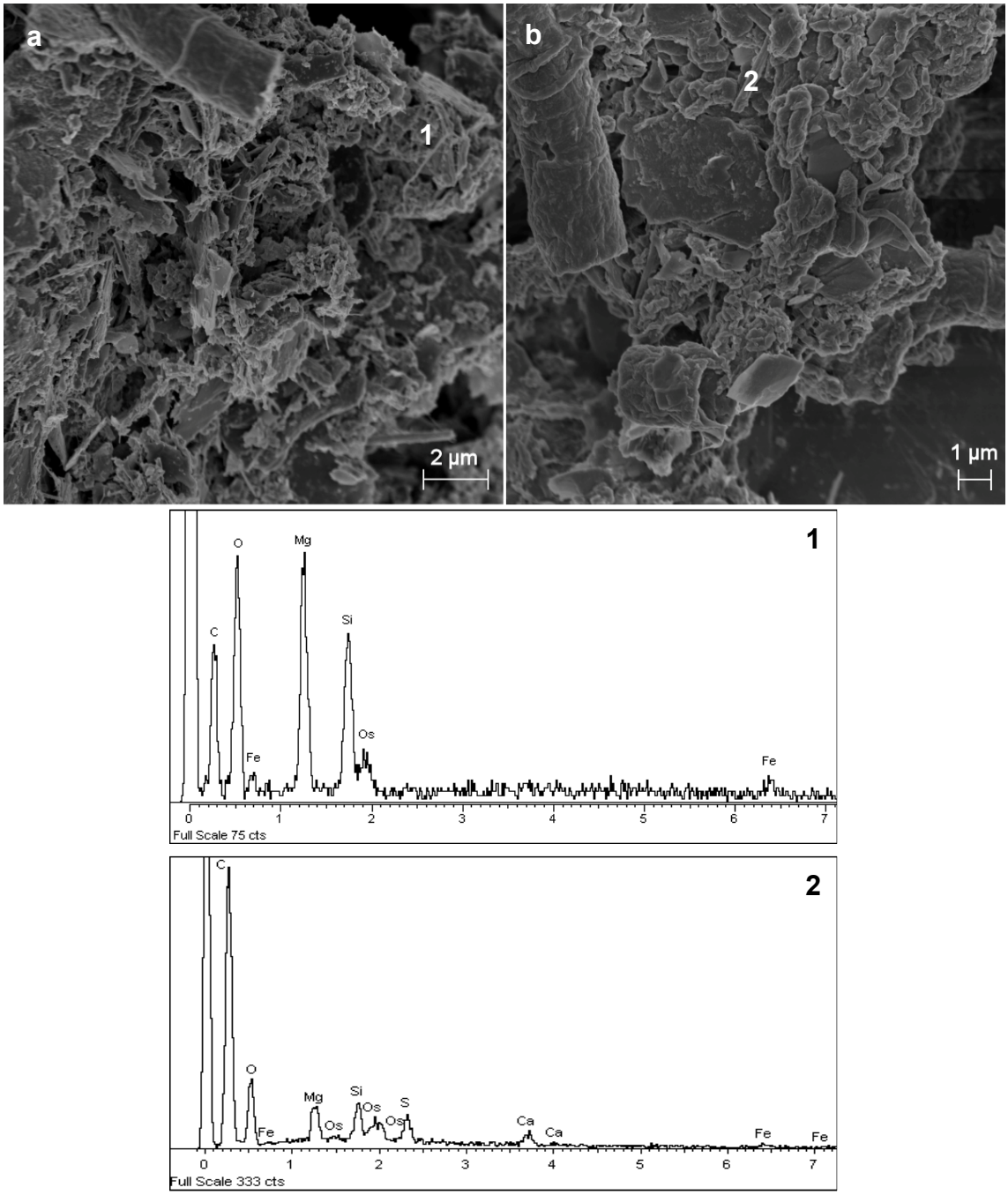

Figure 2.13 a) Precipitates trapped in cyanobacterial mat with typical elemental signature of Mg-silicates and organic carbon using EDS-SEM (1). The Os signal is from the plasma coating rather than the sample **b)** Precipitates and elemental signature Mg-silicates with Ca and S (2) from sulphide spot in the centre of the chamber.

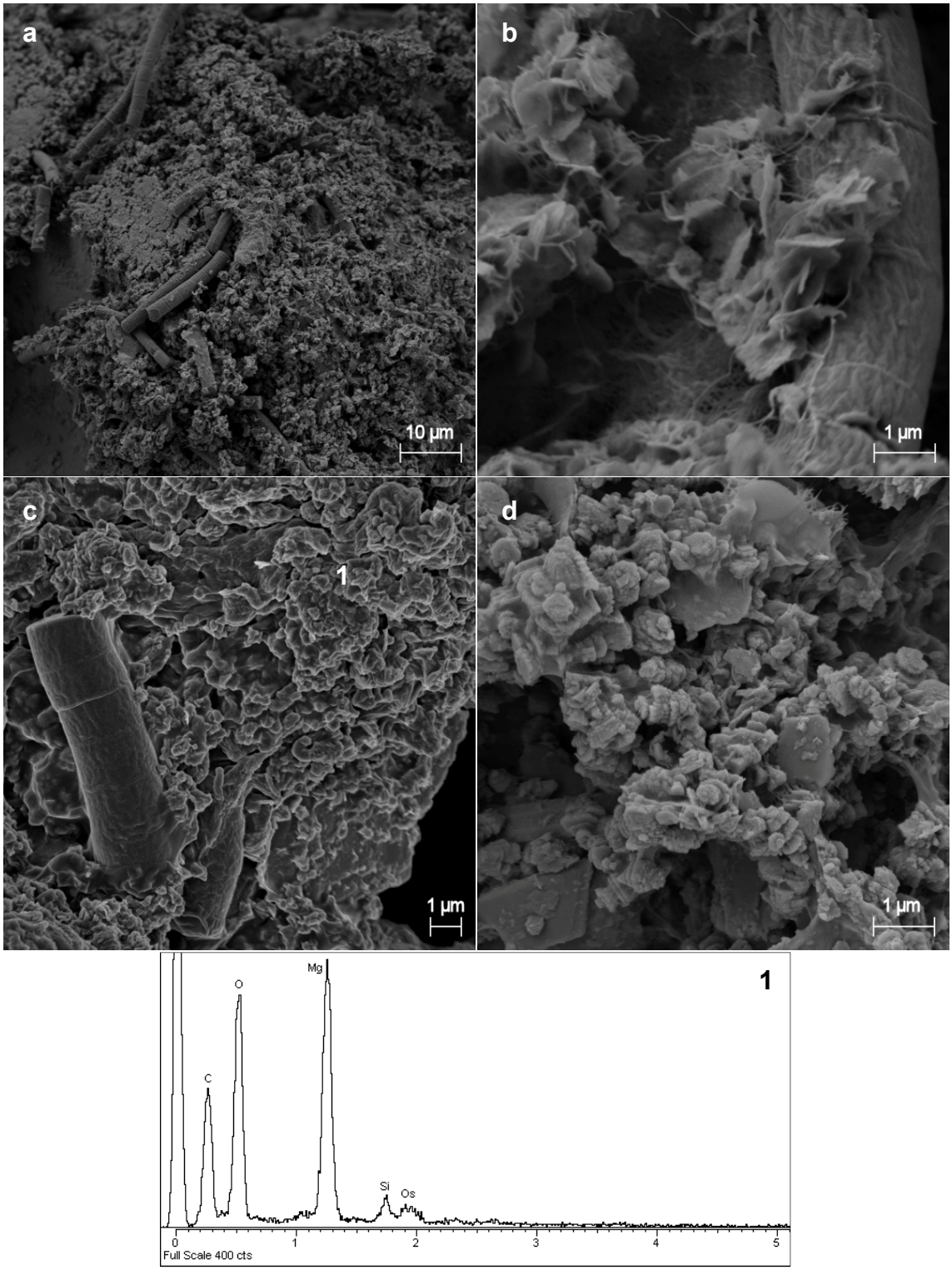

Figure 2.14 Carbonate minerals in OCM experiment. **a)** Si-poor rosettes in a sample of mat growing on the OCM sand surface. **b)** Close up of rosette mineral attached to cyanobacteria. **c)** Trapped Si-poor precipitate in the OCM cyanobacterial pellicle with an EDS signal (1). **d)** Close up of blocky precipitates in cyanobacterial pellicle.

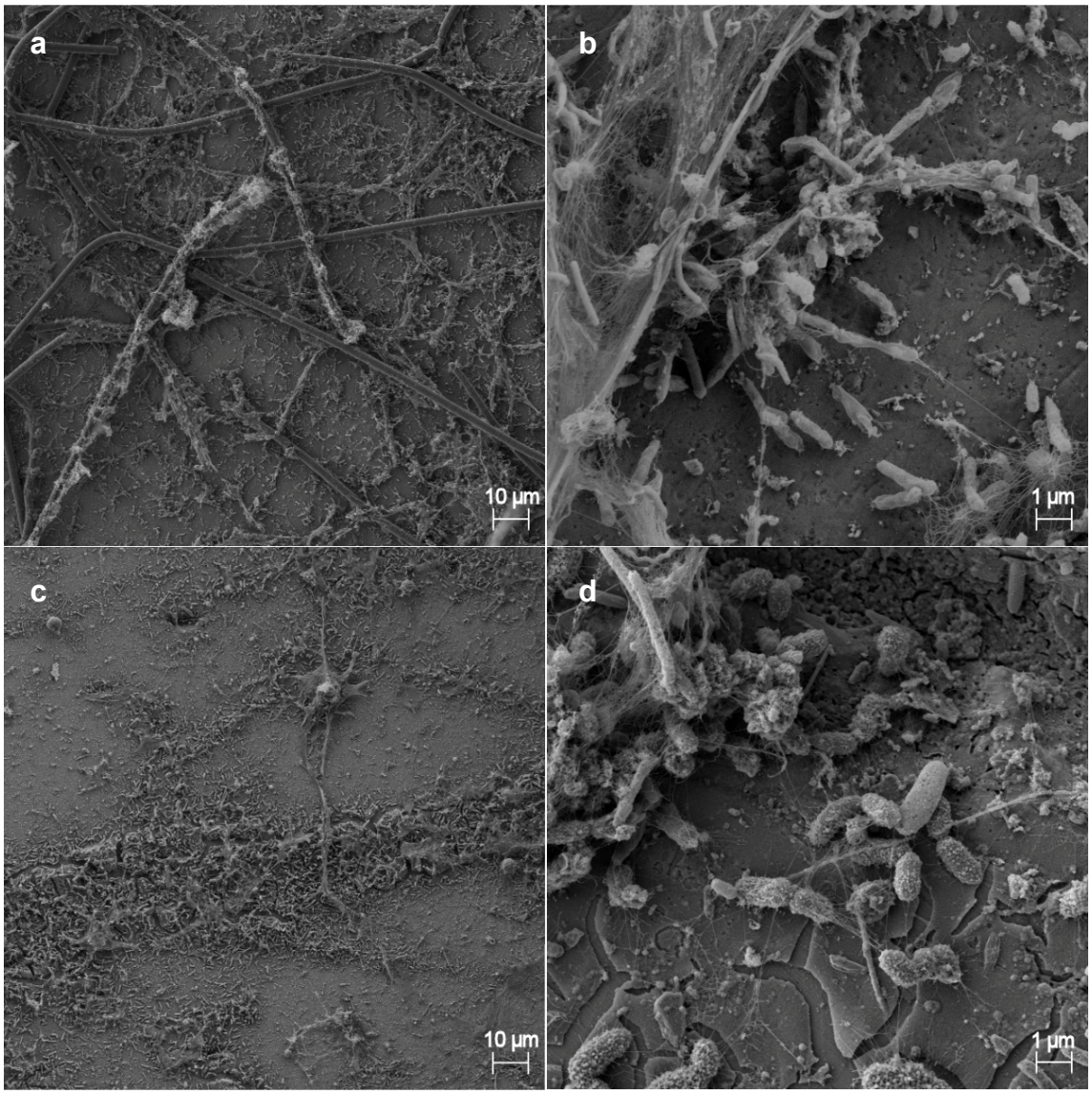

Figure 2.15 Cyanobacterial mat in OCM experiment attached to the fayalite-magnetite mineral key. **a)** Abundant heterotrophs and EPS associated with iron rich minerals. **b)** Close up of heterotrophs caught in EPS and attached to mineral surface. **c)** Abundant heterotrophs attached to iron rich minerals below sand surface. **d)** Close up of rod shaped bacteria, most likely *Shewanella oneidensis*.

rod-shaped heterotrophs were covered in organic surface nodules, which was only rarely seen in other areas of the mat (Figure 2.15d).

2.4 Discussion

BASE geochemical changes

Low temperature serpentinization of either the iron component of the olivine sand (Equation 2.1) or the fayalite mineral key (Equation 2.2) resulted in the production of $H_{2(g)}$ in the BASE experiment. Based on the mole ratio of olivine to hydrogen determined by Bach et al. (2006), 5000 ppm $H_{2(g)}$ (2.0×10^{-4} M) in the headspace is equivalent to 3.04 g of the 7.6 kg of forsterite (Fo_{90}) sand or 0.161 g of pure fayalite (Fe_2SiO_4) being serpentinized.

$$2Mg_{1.8}Fe_{0.2}SiO_4 + 3H_2O \rightarrow Mg_{2.85}Fe_{0.15}Si_2O_5(OH)_4 + Mg_{0.75}Fe_{0.25}(OH)_2 \quad (2.1a)$$

$$57Mg_{0.75}Fe_{0.25}(OH)_2 + 30SiO_2 \rightarrow 15Mg_{2.85}Fe_{0.15}Si_2O_5(OH)_4 + 23H_2O + 4Fe_3O_4 + 4H_{2(g)} \quad (2.1b)$$

$$2Fe_2SiO_4 + 2H_2O \leftrightarrow 2Fe_3O_4 + 3SiO_2 + 2H_2 \quad (2.2)$$

The presence of $H_{2(g)}$ in the BASE experiment is consistent with the results of Neubeck et al. (2011), who produced $H_{2(g)}$ and $CH_{4(g)}$ from the serpentinization of forsterite (Fo_{91}) sand after nine months of incubation at 30˚C. In their experiment, 25 ± 10 ppm of $H_{2(g)}$ was produced in a buffered solution and 10 ± 2 ppm was produced from pure water reacted with 9 g of forsterite sand (Neubeck et al. 2011). A higher concentration of $H_{2(g)}$ in BASE experiment was intuitively due to a greater forsterite surface area available for reactions rather than differences in chemical composition. Serpentinization also resulted in the precipitation of secondary Mg-silicate minerals with

rod and plate morphologies, most likely chrysotile and lizardite, in the small-scale abiotic experiment and on the BASE mineral keys. The splitting of forsterite and fayalite minerals occurred because serpentinization results in volumetric expansion (O'Hanley 1992).

In the first half of the BASE experiment $Fe^{2+}_{(aq)}$ accumulated due to olivine dissolution into an anoxic aqueous phase. The addition of oxygen at week 7 resulted in oxidation of $Fe^{2+}_{(aq)}$ and of the surface of any ferrous minerals and the precipitation of ferric hydroxides, such as the iron oxide observed on the surface of the fayalite-magnetite mineral key. The precipitation of ferric hydroxides on the surface of the fayalite can decrease dissolution and serpentinization rates (Wogelius and Walter 1992).

While some bacteria were observed on the surface of the BASE fayalite-magnetite mineral keys, the limited surface area of the key (0.0006% of total surface area) relative to the surface area of the forsterite sand demonstrates a limited total number of bacteria in the chamber. The preferred bacterial attachment to the iron-rich mineral key suggests the bacteria may be employing a metabolic process that relies on iron–perhaps iron reduction coupled with H_2 oxidation. The presence of some oxygen in the BASE chamber likely had a greater influence on serpentinization than the limited number of cells and organics.

Oxidation of the Archean lithosphere independent of oxygenic photosynthesis

During the early to mid-Archean, processes that oxidized chemical species in the lithosphere would have 'set-up' the Earth's atmosphere for accumulating oxygen in the late Archean by removing oxygen sinks (Petsch 2011). These processes included the loss of hydrogen from Earth into space and the burial of organic matter produced by anoxygenic photosynthesis. Irreversible oxidation of the crust can occur when hydrogen

is transported to the upper atmosphere and then lost to space (Walker 1977). During the Archean this process was enhanced by the anoxic, slightly reducing state of the atmosphere (Walker 1977). The rate of hydrogen loss from Earth was most likely controlled by the mixing ratio of hydrogen containing gases, most importantly $H_{2(g)}$ and $CH_{4(g)}$, and their diffusion rate into the upper atmosphere (Catling and Claire 2005).

Globally the hydrolysis of ferrous iron is the largest source of abiotic H_2 and results in accumulated ferric iron in the lithosphere (Apps and van de Kamp 1993). At serpentine vents Fischer-Tropsch type reactions can abiotically catalyze a small amount of H_2 and CO_2 to form methane but most of the H_2 is released into the ocean (McCollom and Seewald 2001). Several estimates for Archean flux of H_2 production have been calculated from modern serpentinization rates and range from 0.8×10^{11}mol/year (Canfield et al. 2006) to 4.5×10^{11}mol/year (Bach and Edwards 2003). These are low estimates as a higher mantle temperature in the Archean may have resulted in more seafloor ultramafic rocks and higher rates of serpentinization and H_2 production (Kasting 2001).

Pavlov et al. (2000) and Kasting et al. (2001) have hypothesized that throughout the Archean most of the H_2 from serpentinization was consumed by methanogens, resulting in a methane rich atmosphere. This hypothesis was supported by a closed experiment where methanogens were able to draw down $H_{2(g)}$ to 40 ppm (Kral et al. 1998). Archean estimates from a biosphere-atmosphere coupled model determined $CH_{4(g)}$ would be 1000 ppm and $H_{2(g)}$ would range from 50-100 ppm (Kharecha et al. 2005). Thus, autotrophic methanogenesis could have had a primarily production rate of 3.4×10^{12} mol/year or 1% of the total production rate in the early Archean (Canfield et al.

2006). Methane that diffuses into the upper atmosphere is quickly photolysed to $CO_{2(g)}$ and $H_{2(g)}$, which subsequently escapes into space (Catling et al. 2001)

One hydrogen pathway in the Archean environment that needs to be further explored is the possibility of competition between autotrophic methanogenesis and other microbial metabolic processes for H_2 (Canfield et al. 2006). In modern vent systems, Bach and Edwards (2003) have predicted a range of metabolic processes that are more energetically favourable than methanogenesis, i.e., that couple H_2 oxidation with nitrate reduction, iron reduction or sulphate reduction and may produce considerable biomass at vent. Canfield et al. (2006) has also proposed that some of the H_2 may have been used by H_2-based anoxygenic photosynthesis rather than methanogenesis. The portion of organic carbon from these processes that became buried rather than degraded to methane would have diverted hydrogen from entering the atmosphere (Canfield et al. 2006). In contrast, additional production of oxidized species of S and Fe at the Earth's surface can also be produced by anoxygenic photosynthesis (Canfield et al. 2006). These oxidized species could accumulate if the organic matter produced by photosynthesis was buried or the organic matter was degraded to methane, in which the hydrogen ultimately escaped into space.

The net oxidation of minerals was observed on a small scale in the BASE experiment. While the dissolution of olivine resulted in the accumulation of up to 5.6 $x10^{-5}$ mol of $Fe^{2+}_{(aq)}$, the production of $7.2x10^{-4}$ mol $H_{2(g)}$ also resulted in the oxidization of $1.4x10^{-3}$ mol of Fe^{2+} in minerals, which otherwise would have had the potential to draw down $3.6x10^{-4}$ mol of $O_{2(g)}$. The maximum rate of hydrogen production was $2.1x10^{-5}$ mol/day.

OCM geochemical changes

The large decrease in $CH_{4(g)}$ in the first week of the OCM experiment was presumably due to microbial processes. Aerobic methane oxidation likely consumed the methane and remnant or photosynthetic oxygen in the chamber and producing $CO_{2(g)}$. While anaerobic methane oxidation coupled with sulphate reduction is possible in modern marine environments (Hoehler et al. 1994; Boetius et al. 2000), based on the extremely rapid disappearance of methane, this likely did not occur in the OCM experiment. Also, over the first four weeks, the very limited total sulphate in the OCM aqueous phase remained constant, whereas, O_2 in the atmosphere and the aqueous phase decreased in the first week. The maximum rate of methane consumption during this period was 0.10 mM/day. The addition of $CO_{2(g)}$ from methanotrophy decreased the pH from 8.0 to 6.8, supporting the concept of an early slightly acidic ocean (Grotzinger and Kasting 1993).

After the first week, the growth of cyanobacteria using oxygenic photosynthesis resulted in a large increase in oxygen and decrease in carbon dioxide and had the greatest influence on geochemical changes. Increasing dissolved and gaseous O_2 coupled with a constantly low $CO_{2(g)}$ concentration during weeks 3 to 10 implies a tight carbon cycling between respiration and photosynthesis within the mat. Concentrations of inorganic carbon in cyanobacteria can be up to 1000 greater than in solution due to carbon concentrating mechanisms (Merz 1992). The non-linear increase and then plateau in $O_{2(g)}$ is similar to a typical biologic growth curve. The plateau in growth and $O_{2(g)}$ was most likely due to limited availability of inorganic carbon in the closed system. The theoretical total oxygen produced by all inorganic carbon in the OCM experiment (13.5 mmol total)

is 9% $O_{2(g)}$, however, ascorbic acid could be used as an extra source of carbon if it is respired by heterotrophs. In particular, *S. oneidensis* can use ascorbic acid as an electron donor (Biffinger et al. 2008) bringing this initial reducing agent into the ecosystem.

Because oxygenic photosynthesis preferentially removes $H_2CO_{3(aq)}$ and $HCO_3^-{}_{(aq)}$, the pH increased from 6.8 to 9.5 after week 3. Even in open systems, modern marine cyanobacterial mats can increase the pH of the surrounding water to > 9 (Revsbech et al. 1983). After week 7, increased respiration below the mat decreased the pore water pH from 9 to 8.5. The combination of increased pH and alkalinity due to photosynthesis and respiration induced the precipitation of the Mg-carbonates in the mat (Thompson and Ferris 1990; Dupraz et al. 2009), which would have limited primary productivity.

Rod, vibroid and coccoid morphologies observed under SEM are consistent with the inoculum of FeRB, SRB and methanogens, respectively. The FeRB morphotype was primarily found attached to the fayalite-magnetite minerals surface within the anoxic sediment. The presence of a sulphide spot (indicated by blackening) in the centre of the mat shows that SRB were active despite a low sulphate concentration. The SRB may have also been limited by the high pH in the mat because the growth of *Desulfovibrio* is inhibited above pH 8.5 (Birnbaum and Wireman 1984). Fluctuating methane concentrations between week 1 and 10 were most likely due to a balance between rates of methanogenesis and methanotrophy. However, decreasing $CH_{4(g)}$ in the last seven weeks of the experiment shows that the rate of methanotrophy was greater than methanogenesis. Low rates of methanogenesis have also been found in other laboratory model cyanobacterial mats, with methanogenesis only accounting for 0.4% of total carbon released (Bebout et al. 2004). Dissolved iron from the fayalite-magnetite key that

accumulated at the start of the experiment when oxygen concentrations were low decreased quickly in response to increased oxygen and microbial biomass. The difference in heterotroph abundance between the forsterite and fayalite mineral surfaces at the end of the experiment suggests aerobic heterotrophic growth may have been limited by iron availability. Modern ocean planktonic heterotrophs uptake ~7.5 μmol Fe/mol of C compared to cyanobacteria that contain 19 μmol Fe/mol of C and have a higher uptake rate (Tortell et al. 1996).

The presence of lizardite and chrysotile on the forsterite suggests low temperature serpentinization also occurred in the OCM experiment. The etch pits observed on the forsterite grains were similar to other forsterite-bacteria alteration and abiotic forsterite dissolution experiments (Shirokova et al. 2012). If $H_{2(g)}$ was produced, it would have been rapidly consumed by bacteria as an additional energy source rather than accumulating in the headspace. FeRB, SRB and methanogens can all use $H_{2(g)}$ in their metabolic processes (Lovley 1991; Bergey et al. 2001). At standard state, iron reduction, sulphate reduction and methanogenesis coupled with hydrogen oxidation all provide more energy per mol of electron acceptor than acetate oxidation (Amend and Shock 2001).

While serpentinization in the OCM sediment likely occurred, geochemical modelling shows the amount of $H_{2(g)}$ produced in the OCM experiment was less than the BASE experiment. Cyanobacterial growth can indirectly change the rate of serpentinization by changing the redox potential of the solution and increasing the pH. First, serpentinization would have been inhibited by higher oxygen activities as ferrous iron is more rapidly oxidized by the O_2 rather than by the hydrolysis by water (Neal and

Stanger 1983). The resulting Fe^{3+} on the olivine surface would further inhibit dissolution (Santelli et al. 2001). Second high pH may have hydrated Mg surface sites inhibiting dissolution of forsterite (Pokrovsky and Schott 2000). In contrast to this study, Shirokova et al. (2012) determined that in basic solutions the presence of bacteria and organics had no direct affect on forsterite dissolution.

The increase in dissolved silica has been a proxy for the amount of the serpentinization in other experiments (Neubeck et al. 2011). As such, the difference in final pore water silica concentration between the OCM (7.9 μM) and BASE (11.9 μM), may be due to differences in the amount of serpentinization that occurred at depth in the sand. Alternatively the silica in the OCM experiment could be adsorbed to organics coating the sand as in the surface water. Low silica in the OCM surface water was most likely due to silica adsorption onto cell surfaces and EPS, thus limiting the diffusion of silica from the pore water to the surface water. The adsorption of $H_4SiO_{4(aq)}$ to carboxyl and hydroxyl functional groups on organic matter and subsequent polymerization into crystalline silica is a passive process (Westall et al. 1995).

Some of the geochemical changes in the OCM system can be applied to predict reactions in an Archean oxygen oasis, whereas others cannot because the OCM was a closed experiment. In particular the production of Mg-carbonates, the tight cycling of sulphur, the rate of oxygen production, and the rate of methanotrophy from OCM experiment can be compared and applied to the Archean geologic record.

Potential biosignatures produced in OCM experiment

The precipitation of carbonates in the OCM experiment shows the potential for fossilization and the preservation of biotic structures. Within microbial mats, oxygenic

photosynthesis, iron reduction, sulphate reduction and methanogenesis promote the precipitation of carbonates, whereas aerobic respiration and fermentation result in carbonate dissolution (Visscher and Stolz 2005). The precipitated Mg-carbonates in the OCM experiment had a similar morphology to the dypingite precipitated from a cyanobacterial mat in a Mg-rich playa (Power et al. 2007) but the precipitates were too small to determine the exact composition using x-ray diffraction. The carbonates in the OCM may be showing early stages of carbonate precipitation leading to the construction of stromatolites, particularly for Mg-rich carbonate stromatolites. While magnesite is relatively rare compared to dolomite and calcite in the rock record, it has been found in several Archean and Proterozoic stromatolites (Schidlowski et al. 1975; Mekezhik et al. 2001). Interestingly, a well described magnesite stromatolite in the ~2.0 Ga Tulomozerskaya Formation, Russia also had an unexpected high Mn concentration (Mekezhik et al. 2001). The Mg-carbonates in the OCM experiment suggest can Mg and Mn co-precipitate and that Mn does not need to be added in a secondary fluid.

The low sulphate concentration (~0.3 mM) in the OCM experiment was a good model for the Archean ocean as S isotopes suggest the sulphate concentration was < 0.2 mM (Canfield and Raiswell 1999; Habicht et al. 2002). The growth of an iron sulphide spot under the cyanobacterial mat suggests a S cycling link between SRB and oxygen was occurring in the mat. Several studies have determined that sulphur cycling occurred where biogenic pyrite was partially oxidized by oxygen and then re-reduced by SRB in the 2.65 to 2.5 Ga Campbellrand-Malmani platform, South Africa (Kamber and Whitehouse 2006; Zerkle et al. 2012). In the OCM experiment SEM-EDS showed that a small amount of sulphur had precipitated in this area, however, crystals were too small to

be distinguished. SEM-EDS spectra with a sulphur signal also often contained calcium, which was most likely from a calcium magnesium carbonate. Alternatively the calcium signal may be from gypsum precipitation, but this is less likely as gypsum is undersaturated in the solution (Appendix D-2). In modern marine mats SRB are often closely associated with carbonates (Dupraz et al. 2004) and dissimilatory sulphate reduction is known to induce precipitation of low temperature dolomite (van Lith et al. 2003a). Sulphate reduction increases dolomite precipitation, in particular, by removing SO_4^{2-} from Mg-sulphate complexes, thus increasing the Mg^{2+} concentration (van Lith et al. 2003b). This close association between Ca-Mg carbonates, biogenic pyrite and SRB has been observed in modern stromatolites and may have also occurred in Precambrian stromatolites (Vasconcelos et al. 2006; Spadafora et al. 2010).

Interestingly, the iron phenotype of a more oxidized environment, the presence ferric hydroxides resulting in a red precipitate, was preserved on one of BASE fayalite-magnetite mineral keys but not on any of the OCM fayalite-magnetite mineral surfaces despite a large difference in oxygen concentration. This was likely due the abundance of FeRB in the OCM metabolizing ferric hydroxides and other bacteria chelating iron. This suggests the preserved ratio of Fe(II) to Fe(III) from the Archean does not have a simple relationship with the amount of oxygen but is also dependent on the amount of iron reduction by bacteria.

The amount of oxygen in Late Archean oxygen oasis

Most estimates for the Archean rate of oxygenic photosynthesis are based on modern laboratory and environmental cyanobacterial mats. The maximum rate of net $O_{2(g)}$ production in the OCM experiment was 0.081 mM per day or 4.9 mmol $O_{2(g)}/m^2$ per

day. In contrast, modern well established cyanobacterial mats have an oxygen production rate of 156-190 mmol O_2/m^2 per day (Stal 2000). The oxygen production rate used in the Kasting et al. (2001) atmospheric model was 83 mmol O_2/m^2 per day. In another laboratory grown cyanobacterial mat, the net photosynthesis was 60 mmol O_2/m^2 per day (Fenchel 1998). The relatively low rate of net oxygen production in the OCM experiment may be due to limited light intensity associated with the plexiglass chamber or less than optimal nutrient conditions. For example an *Oscillatoria* mat had an oxygen production range from 6.5 to 121 mmol O_2/m^2 per day when the amount of solar irradiance was varied (Kuhl et al. 1996). The slower rate of oxygen accumulation may also be due to tight coupling between photosynthesis and aerobic heterotrophy. Oxygen production rates in the Archean have been hypothesized to be lower than modern due to a faint young Sun, high rates of cellular damage by high UV intensities (Phoenix et al. 2001) or limited nutrients (Fennel et al. 2005; Zerkle et al. 2006; Anbar 2008).

Despite a lower net oxygen production rate, the concentration of oxygen in the OCM surface water falls within the range of oxygen concentrations predicted for Archean oxygen oasis conditions, as the OCM chamber was a closed system. As such the OCM experiment, with 0.13mM of dissolved oxygen in the surface water, is an applicable analogue for oxidation reactions, such as methanotrophy and iron oxidation. As a low estimate, Brocks et al. (2003) determined from molecular markers in 2.7-2.5 Ga kerogen that the minimum dissolved oxygen concentrations that could support aerobic respiration was 0.003 mM. Based on the oxygen diffusion rate, Kasting et al. (2001) determined the steady-state dissolved O_2 above a late Archean mat would be 0.021 mM. Whereas a more comprehensive numerical model predicted O_2 concentrations of 0.45- 0.65 mM at

the top of the mat, showing that oxygen concentration in the mat was independent of atmospheric oxygen concentration (Herman and Kump 2005). In addition, oxygen supersaturation and trapped oxygen bubbles in modern marine cyanobacterial mats during the day is common (Stal 2000) and similar conditions were most likely present in the Archean.

The OCM experiment could not be used to predicted the accumulation rate of oxygen in the Archean because oxygen accumulation depends on the rate of organic burial. The rate of organic burial is dependent on both the rate of primary productivity and the rate of heterotrophy and organic degradation, which consume oxygen. The OCM experiment did not run for a long enough time period to determine relative rates of primary productivity and heterotrophy in an established mat. However, at in the beginning of the OCM experiment oxygen was taken up quicker by methanotrophy and heterotrophy rather than abiotically reacting with iron, allowing for continued $Fe^{2+}_{(aq)}$ accumulation despite rapid cyanobacterial growth.

Changes in late Archean methane concentration

In the OCM experiment, rapid aerobic methanotrophy was an unexpected geochemical change. Determining the presence, amount and rate of methanotrophy in Archean oxygen oasis is challenging as the both the reactants and products of the reaction are not preserved in the geologic record. The best evidence for methanotrophy in Archean shallow waters is the $\delta^{13}C$ values of organic carbon. Throughout Earth's recorded geologic history, the difference in carbon isotopic fraction between carbonates (average $\delta^{13}C$= 0‰) and organic carbon (average $\delta^{13}C$= -30 to -25‰) has mostly remained constant and primarily reflects the isotopic signature of photosynthesis

(Schidlowski 1987). Between 2.8 to 2.5 Ga an excursion with very low organic $\delta^{13}C$ values (~ -50 ‰) occurred without a corresponding change in carbonate isotopic values (Hayes 1983). Highly depleted carbon can occur where highly depleted carbon from methanogenesis is incorporated into organic biomass by methanotrophy and subsequently buried (Hayes 1983). Archean organics with highly depleted $\delta^{13}C$ values was first reported in graphites from iron formations of the Superior Province, Canada (Schoell and Wellmer 1981). To preserve a $\delta^{13}C$ value of -50 ‰ in kerogen, Hayes (1994) calculated that at least one third of the preserved organics must have come from methanotrophs. The OCM experiment could not accurately model factors limiting the incorporation of methane into biomass in a methane rich environment because it was a closed system, where methane accounted for < 5% of the total carbon.

While some researchers have prescribed an abiotic origin to the highly depleted carbon from the late Archean (Pavlov et al. 2001), spatial differences in $\delta^{13}C$ values from rocks of the same age strongly suggests a biotic process rather than atmospheric source for depleted $\delta^{13}C$ values (Thomazo et al. 2009). In the 2.72 Ga Hamersley Basin, Eigenbrode and Freeman (2006) found shallow water kerogen $\delta^{13}C$ values ranged from -57 to -28 ‰, whereas deep-water kerogen $\delta^{13}C$ values ranged from -40 to -45 ‰. The shallow marine $\delta^{13}C$ values are interpreted as being influence by both aerobic heterotrophy and methanogenesis and the deep marine $\delta^{13}C$ values are interpreted as being somewhat influenced by methanogenesis but mostly to be a product of anaerobic respiration (Eigenbrode and Freeman 2006). Thomazo et al. (2009) also found variations in $\delta^{13}C$ values within the shelf environment, as organics with highly depleted $\delta^{13}C$ values often occurred in mudstones but were less depleted in nearby siltstones and stromatolites.

While the presence of highly depleted $\delta^{13}C$ records the incorporation of methane into organic carbon, carbon isotopes cannot be used to determine if methanotrophy was aerobic, like the OCM experiment, or due to anaerobic oxidation of methane (AOM). In modern marine systems, AOM is completed by a consortia of methanogenic and sulphate reducing bacteria, although the exact mechanisms are unknown (Boetius et al. 2000). The reaction can be simplified as Equation 2.3 (Amend and Shock 2001). Hinrichs (2002) has determined that AOM in the Archean is theoretically possible even with limited oceanic sulphate. Aerobic methanotrophy can be completed by some members of the α- and γ-proteobacteria classes (Hanson and Hanson 1996) by the reaction in Equation 2.4 (Amend and Shock 2001). 3β-methylhopane is a unique biomarker to γ-proteobacteria methylotrophs that has been found in shallow marine rocks from the late Archean (Brocks et al. 2003; Eigenbrode et al. 2008). Thus, the organisms responsible for anaerobic and aerobic methanotrophy are generally considered to have been present in the late Archean.

$$CH_{4(aq)} + SO_4^{-2} + 2\,H^+ \rightarrow H_2S_{(aq)} + CO_{2(aq)} + 2\,H_2O_{(l)} \quad \Delta Gr^\circ = -109.35\frac{kJ}{mol} \quad (2.3)$$

$$CH_{4(aq)} + 2\,O_{2(aq)} \rightarrow CO_{2(aq)} + 2\,H_2O_{(l)} \quad \Delta Gr^\circ = -858.97\frac{kJ}{mol} \quad (2.4)$$

In modern marine environments, methane is primarily sourced from methanogenesis of organics that occurs in the sediment once all other electron acceptors have been depleted (*e.g.,* Canfield and Thamdrup 2009). This methane diffuses through an anaerobic, sulphate rich layer before reaching aerobic waters, allowing for anaerobic methane oxidizers to access the methane before aerobic methanotrophs. In the late Archean, abundant atmospheric methane and methanogenesis was present. In contrast,

$O_{2(aq)}$ likely had a gradient with high concentrations above or nearby a cyanobacterial mat and low concentration in deeper water environments. Within the oxygen oasis, aerobic methanotrophy would likely outcompete anaerobic methanotrophy. At standard state, aerobic methanogenesis (Equation 2.4) can potentially provide much more energy than anaerobic methanogenesis (Equation 2.3), iron reduction, sulphate reduction or methanogenesis (Amend and Shock 2001). Anaerobic methane oxidation was likely more prevalent in deeper water environments where oxygen was limited but sulphate concentrations were elevated due to oxidative sulphide weathering on continents, near-shore environments and subsequently on continental shelves . This may explain the difference in depleted $\delta^{13}C$ values between shallow marine and deep marine sediments noted by Hinrichs (2002), and Eigenbrode and Freeman (2006). For example organic carbon from the Tumbina Formation (shallow marine) has a $\delta^{13}C$ = -60.9 to -28.5 ‰ with an average of -47.9 ‰ and Jeerinah Formation (deep marine) has a $\delta^{13}C$ = -48.6 to -27.9 ‰ with an average of -40.0 ‰ (Strauss and Moore 1992). The presence of aerobic methanotrophs on Archean shallow marine shelves is supported by a greater concentration of aerobic methanotrophs molecular biomarkers in this environment (Eigenbrode et al. 2008).

Because the irreversible oxidation of the crust by hydrogen loss is dependent on the atmospheric mixing ratio of H-bearing species, constraining late Archean methane flux is important for understanding the accumulation of oxygen (Catling et al. 2001). From the mid to late-Archean the amount of methane from abiotic sources and autotrophic methanogenesis previously described was unlikely to have changed. Conversely, the amount of methane from acetoclastic methanogens likely increased with

the advent of oxygenic photosynthesis due to an increase in the amount primary productivity (Catling et al. 2001). The sinks for methane in the late Archean would have included aerobic methane oxidation, anaerobic methane oxidation and abiotic photochemical reactions between atmospheric oxygen and methane. The change in methane flux was likely dominated by the ratio between 1) increased primary productivity that increased organic carbon and thus methanogenesis and 2) an increase in biological methane oxidation. Determining the amount of change in sources and sinks of methane is difficult as some processes would have occurred on a global-scale, where as others would have been highly localized. In particular, aerobic methanotrophy would have occurred in close association with cyanobacterial mats whereas methanogesis could have occurred wherever organic carbon was transported.

The assumption that methanotrophy does not affect Archean atmospheric methane flux needs to be re-evaluated because 1) $\delta^{13}C$ of organics shows abundant methanotrophy during the Archean and 2) the rate of methanotrophy and the factors influencing the rate are poorly constrained. In the OCM experiment aerobic methanotrophy occurred rapidly in response to available methane and oxygen. In this closed system, the maximum rate of methanotrophy was slightly greater than the maximum rate of oxygenic photosynthesis and methanogenesis. Aerobic methanotrophy was more likely limited by oxygen rather than methane during the initial period of the experiment. Even starting at lower methane concentration (< 500 ppm), methanotrophs steadily drew down atmospheric methane concentrations at rate of > 1.72×10^{-7} M/day to below 150 ppm. The fast rate of methanotrophy at high methane concentrations and slow rate at low concentrations is consistent with reported values. The methanotrophy K_m value for methane is ~1 μM,

equivalent to ~ 700 ppm $CH_{4(g)}$ in the atmosphere (Joergensen and Degn 1983) but the metabolic limits for methanotrophs is 20 nM dissolved CH_4 (18 - 22 μatm $CH_{4(g)}$) (Hayes 1994). The methanotrophy K_m value for oxygen is 0.14 μM (Joergensen 1985). Thus methane and oxygen concentrations high enough for methanotrophic growth could be fulfilled at Archean microbial mats however, oxygen would become limiting further away from the mat.

While mass independent fractionation of sulphur (MIF-S) shows that Archean atmospheric O_2 concentration was < 10^{-5} present atmospheric level (PAL) (Farquhar et al. 2000; Pavlov and Kasting 2002), several researchers had noted that amount of MIF-S, measured as $\Delta^{33}S = \delta^{33}S - 0.515 \times \delta^{34}S$, has varied through the Archean (Ono et al. 2003). In particular, between 3.2 and 2.7 Ga $\Delta^{33}S$ has a reduced range, ~2 ‰, whereas between 2.7 and 2.45 Ga , the $\Delta^{33}S$ has a large range, ~12 ‰ (Domagal-Goldman et al. 2008). The amount of MIF-S variation in the anoxic Archean was most likely due to the thickness of organic haze present in the atmosphere (Domagal-Goldman et al. 2008). Atmospheric models have predicted that when CH_4/CO_2 mixing ratios are > 0.1 in an anoxic atmosphere organic haze decreases the $\Delta^{33}S$ range (Domagal-Goldman et al. 2008). In the 2.72 Ga Tumbiana Formation, Australia, Thomazo et al. (2009) found that changes in a greater range of MIF-S values were positively correlated to highly depleted $\delta^{13}C$ in organics. This suggests that the methane concentration and the amount of methanotrophy are related.

One other factor influencing the rate and amount of methanotrophy in the Archean may have been the concentration of dissolved copper. The enzyme methane monooxygenase (pMMO), which converts methane to methanol in all marine

methanogens, requires copper concentrations above 0.8 μM or a mineralogical source of copper to be expressed (Fru 2011). Models of the Precambrian ocean metal chemistry have predicted copper concentrations in the bulk ocean to be very low because of complexation to sulphides and oxides (Saito et al. 2003). Interestingly, in modern marine environments methanotrophy is greater where ferrihydrite is deposited because copper has a high affinity for ferrihydrate (Fru 2011). If a similar relationship existed in the Archean, this would support the original hypothesis of Schoell and Wellmer (1981) that highly depleted $\delta^{13}C$ in iron formations was from methanotrophy. In the modern seafloor, high concentrations of copper in basalts and hydrothermal vents may be key in the enhanced methanotrophy found there (Fru 2011). This limit on methanotrophy was unlikely present in the OCM experiment as chalcopyrite was present in the fayalite-magnetite mineral keys.

2.5 Conclusion

The geochemistry of the OCM experimental system was initially dominated by methanotrophy, which decreased the methane concentrations, increased the carbon dioxide concentration and decreased pH. Once methane was depleted, oxygenic photosynthesis dominated the system and decreased the carbon dioxide concentration, increased the oxygen concentration and increased the pH, which resulted in the oxidation of ferrous iron and carbonate precipitation. Similar metabolic processes and geochemical changes may have occurred in an Archean cyanobacterial mat undergoing oxygenic photosynthesis. The precipitation of pyrite and Mg-carbonates may be potentially used as biosignatures for life in the Archean.

2.6 References

Amend, J. and Shock, E. 2001. Energetics of overall metabolic reactions of thermophilic and hyperthermophilic Archaea and Bacteria. FEMS Microbiology Reviews, **25**: 175-243.

Anbar, A.D. 2008. Elements and evolution. Science, **322**: 1481-1483.

Apps, A.A., and Van de Kamp, P.C. 1993. Energy gases of a "biogenic" origin in the Earth's crust. *In* The Future of energy gases *Edited by* D.G. Howell. United States Government Printing Office, Washington, pp. 81-132.

Bach, W. and Edwards, K. 2003. Iron and sulfide oxidation within the basaltic ocean crust: Implications for chemolithoautotrophic microbial biomass production. Geochimica et Cosmochimica Acta, **67**: 3871-3887.

Bach, W., Paulick, H., Garrido, C.J., Ildefonse, B., Meurer, W.P., and Humphris, S.E. 2006. Unraveling the sequence of serpentinization reactions: Petrography, mineral chemistry, and petrophysics of serpentinites from MAR 15 degrees N (ODP leg 209, site 1274). Geophysical Research Letters, **33**: L13306.

Bebout, B., Carpenter, S., Des Marais, D., Discipulo, M., Embaye, T., Garcia-Pichel, F., Hoehler, T., Hogan, M., Jahnke, L., Keller, R., Miller, S., Prufert-Bebout, L., Raleigh, C., Rothrock, M., and Turk, K. 2002. Long-term manipulations of intact microbial mat communities in a greenhouse collaboratory: Simulating Earth's present and past field environments. Astrobiology, **2**: 383-402.

Bebout, B.M., Hoehler, T.M., Thamdrup, B., Albert, D., Carpenter, S.P., Hogan, M., Turk, K., and Des Marais, D.J. 2004. Methane production by microbial mats under low sulphate concentrations. Geobiology, **2**: 87-96.

Bergey, D.H., Garrity, G.M., Boone, D.R., Castenholz, R.W., Brenner, D.J., Krieg, N.R., and Staley, J.T. 2001. Bergey's manual of systematic bacteriology. Springer, New York.

Biffinger, J.C., Byrd, J.N., Dudley, B.L., and Ringeisen, B.R. 2008. Oxygen exposure promotes fuel diversity for *Shewanella oneidensis* microbial fuel cells. Biosensors & Bioelectronics, **23**: 820-826.

Birnbaum, S.J. and Wireman, J.W. 1984. Bacterial sulfate reduction and pH: Implications for early diagenesis. Chemical Geology, **43**: 143-149.

Boetius, A., Ravenschlag, K., Schubert, C., Rickert, D., Widdel, F., Gieseke, A., Amann, R., Jorgensen, B., Witte, U., and Pfannkuche, O. 2000. A marine microbial consortium apparently mediating anaerobic oxidation of methane. Nature, **407**: 623-626.

Brocks, J., Logan, G., Buick, R., and Summons, R. 1999. Archean molecular fossils and the early rise of eukaryotes. Science, **285**: 1033-1036.

Brocks, J.J., Buick, R., Summons, R.E., and Logan, G.A. 2003. A reconstruction of Archean biological diversity based on molecular fossils from the 2.78 to 2.45 billion-year-old Mount Bruce Supergroup, Hamersley Basin, Western Australia. Geochimica et Cosmochimica Acta, **67**: 4321-4335.

Canfield, D.E. and Thamdrup, B. 2009. Towards a consistent classification scheme for geochemical environments, or, why we wish the term 'suboxic' would go away. Geobiology, **7**: 385-392.

Canfield, D. and Raiswell, R. 1999. The evolution of the sulfur cycle. American Journal of Science, **299**: 697-723.

Canfield, D.E., Rosing, M.T., and Bjerrum, C. 2006. Early anaerobic metabolisms. Philosophical Transactions of the Royal Society Biological Sciences, **361**: 1819-1834.

Catling, D. and Claire, M. 2005. How Earth's atmosphere evolved to an oxic state: A status report. Earth and Planetary Science Letters, **237**: 1-20.

Catling, D., Zahnle, K., and McKay, C. 2001. Biogenic methane, hydrogen escape, and the irreversible oxidation of early Earth. Science, **293**: 839-843.

Domagal-Goldman, S.D., Kasting, J.F., Johnston, D.T., and Farquhar, J. 2008. Organic haze, glaciations and multiple sulfur isotopes in the Mid-Archean Era. Earth and Planetary Science Letters, **269**: 29-40.

Dupraz, C., Visscher, P., Baumgartner, L., and Reid, R. 2004. Microbe-mineral interactions: Early carbonate precipitation in a hypersaline lake (Eleuthera Island, Bahamas). Sedimentology, **51**: 745-765.

Dupraz, C., Reid, R.P., Braissant, O., Decho, A.W., Norman, R.S., and Visscher, P.T. 2009. Processes of carbonate precipitation in modern microbial mats. Earth-Science Reviews, **96**: 141-162.

Eigenbrode, J.L. and Freeman, K.H. 2006. Late Archean rise of aerobic microbial ecosystems. Proceedings of the National Academy of Sciences, **103**: 15759-15764.

Eigenbrode, J.L., Freeman, K.H., and Summons, R.E. 2008. Methylhopane biomarker hydrocarbons in Hamersley Province sediments provide evidence for Neoarchean aerobiosis. Earth and Planetary Science Letters, **273**: 323-331.

Farquhar, J., Bao, H.M., and Thiemens, M. 2000. Atmospheric influence of Earth's earliest sulfur cycle. Science, **289**: 756-758.

Fenchel, T. 1998. Artificial cyanobacterial mats: Cycling of C, O, and S. Aquatic Microbial Ecology, **14**: 253-259.

Fennel, K., Follows, M., and Falkowski, P. 2005. The co-evolution of the nitrogen, carbon and oxygen cycles in the Proterozoic ocean. American Journal of Science, **305**: 526-545.

Foster, I.S., King, P.L., Hyde, B.C., and Southam, G. 2010. Characterization of halophiles in natural $MgSO_4$ salts and laboratory enrichment samples: Astrobiological implications for Mars. Planetary and Space Science, **58**: 599-615.

Fru, E.C., Piccinelli, P., and Fortin, D. 2012. Insights into the global microbial community structure associated with iron oxyhydroxide minerals deposited in the aerobic biogeosphere. Geomicrobiology Journal, **29**: 587-610.

Grotzinger, J.P. and Kasting, J.F. 1993. New constraints on Precambrian ocean composition. Journal of Geology, **101**: 235-243.

Habicht, K., Gade, M., Thamdrup, B., Berg, P., and Canfield, D. 2002. Calibration of sulfate levels in the Archean ocean. Science, **298**: 2372-2374.

Hanson, R. and Hanson, T. 1996. Methanotrophic bacteria. Microbiological reviews, **60**: 439-+.

Harrison, P.J., Waters, R.E., and Taylor, F.J.R. 1980. A broad spectrum artificial sea water medium for coastal and open ocean phytoplankton. Journal of Phycology, **16**: 28-35.

Hayes, J.M. 1983. Geochemical evidence bearing on the origin of aerobiosis. *In* The Earth's earliest biosphere: Its origin and evolution *Edited by* J.W. Schopf. Princeton University Press, Princeton, pp. 291-301.

Hayes, J. 1994. Global methanotrophy at the Archean-Proterozoic transition. *In* Early life on Earth: Nobel Symposium No. 84 *Edited by* S. Bengtson. Columbia University Press, New York, pp. 220-236.

Hellevang, H., Huang, S., and Thorseth, I.H. 2011. The potential for low-temperature abiotic hydrogen generation and a hydrogen-driven deep biosphere. Astrobiology, **11**: 711-724.

Herman, E.K. and Kump, L.R. 2005. Biogeochemistry of microbial mats under Precambrian environmental conditions: A modelling study. Geobiology, **3**: 77-92.

Hinrichs, K. 2002. Microbial fixation of methane carbon at 2.7 Ga: Was an anaerobic mechanism possible? Geochemistry, Geophysics, Geosystems, **3**: 1042.

Hoehler, T., Alperin, M., Albert, D., and Martens, C. 1994. Field and laboratory studies of methane oxidation in an anoxic marine sediment: Evidence for a methanogen-sulfate reducer consortium. Global Biogeochemical Cycles, **8**: 451-463.

Hoehler, T.M., Bebout, B.M., and Des Marais, D.J. 2001. The role of microbial mats in the production of reduced gases on the early Earth. Nature, **412**: 324-327.

Holland, H.D. 2011. Discovering the history of atmospheric oxygen. *In* Frontiers in geochemistry: Contribution of geochemistry to the study of the Earth *Edited by* R.S. Harmon and A. Parker. Blackwell Publishing Ltd., West Sussex, pp. 43-60.

Holland, H. 2002. Volcanic gases, black smokers, and the Great Oxidation Event. Geochimica et Cosmochimica Acta, **66**: 3811-3826.

Joergensen, L. 1985. The methane mono-oxygenase reaction system studied invivo by membrane-inlet mass-spectrometry. Biochemical Journal, **225**: 441-448.

Joergensen, L. and Degn, H. 1983. Mass-spectrometric measurements of methane and oxygen utilization by methanotrophic bacteria. FEMS Microbiology Letters, **20**: 331-335.

Kamber, B.S. and Whitehouse, M.J. 2007. Micro-scale sulphur isotope evidence for sulphur cycling in the late archean shallow ocean. Geobiology, **5**: 5-17.

Kasting, J.F. 1993. Earth's early atmosphere. Science, **259**: 920-926.

Kasting, J. 2001. The rise of atmospheric oxygen. Science, **293**: 819-820.

Kasting, J., Pavlov, A., and Siefert, J. 2001. A coupled ecosystem-climate model for predicting the methane concentration in the Archean atmosphere. Origins of Life and Evolution of the Biosphere, **31**: 271-285.

Kendall, B., Reinhard, C.T., Lyons, T., Kaufman, A.J., Poulton, S.W., and Anbar, A.D. 2010. Pervasive oxygenation along late Archaean ocean margins. Nature Geoscience, **3**: 647-652.

Kharecha, P., Kasting, J., and Siefert, J. 2005. A coupled atmosphere-ecosystem model of the early Archean earth. Geobiology, **3**: 53-76.

Kral, T.A., Brink, K.M., Miller, S.L., and McKay, C.P. 1998. Hydrogen consumption by methanogens on the early Earth. Springer Netherlands, .

Kuebler, K.E., Jolliff, B.L., Wang, A., and Haskin, L.A. 2006. Extracting olivine (Fo-Fa) compositions from Raman spectral peak positions. Geochimica et Cosmochimica Acta, **70**: 6201-6222.

Kuhl, M., Fenchel, T., and Kazmierczak, J. 2003. Growth, structure and calcification potential of an artificial cyanobacterial mat. .

Kuhl, M., Glud, R., Ploug, H., and Ramsing, N. 1996. Microenvironmental control of photosynthesis and photosynthesis-coupled respiration in an epilithic cyanobacterial biofilm. Journal of Phycology, **32**: 799-812.

Lovley, D.R. 1991. Dissimilatory Fe(III) and Mn(IV) reduction. Microbiological Reviews, **55**: 259-287.

McCollom, T. and Seewald, J. 2001. A reassessment of the potential for reduction of dissolved CO_2 to hydrocarbons during serpentinization of olivine. Geochimica et Cosmochimica Acta, **65**: 3769-3778.

Melezhik, V., Fallick, A., Medvedev, P., and Makarikhin, V. 2001. Palaeoproterozoic magnesite: Lithological and isotopic evidence for playa/sabkha environments. Sedimentology, **48**: 379-397.

Merz, M. 1992. The biology of carbonate precipitation by cyanobacteria. Springer, Berlin.

Neal, C. and Stanger, G. 1983. Hydrogen generation from mantle source rocks in Oman. Earth and Planetary Science Letters, **66**: 315-320.

Neubeck, A., Nguyen Thanh Duc, Bastviken, D., Crill, P., and Holm, N.G. 2011. Formation of H_2 and CH_4 by weathering of olivine at temperatures between 30 and 70 ˚C. Geochemical Transactions, **12**: 6.

O'Hanley, D.S. August, 1992. Solution to the volume problem in serpentinization. Geology, **20**: 705-708.

Ono, S., Eigenbrode, J., Pavlov, A., Kharecha, P., Rumble, D., Kasting, J., and Freeman, K. 2003. New insights into Archean sulfur cycle from mass-independent sulfur isotope records from the Hamersley Basin, Australia. Earth and Planetary Science Letters, **213**: 15-30.

Parkhurst, D.L. and Appelo, C.A.J. 1999. User's guide to PHREEQC (version 2) - A computer program for speciation, batch-reaction, one-dimensional trasnport and inverse geochemical calculations. Water-Resources Investigations Report 99-4259, U.S. Geologic Survey, Denver.

Pavlov, A. and Kasting, J. 2002. Mass-independent fractionation of sulfur isotopes in Archean sediments: Strong evidence for an anoxic Archean atmosphere. Astrobiology, **2**: 27-41.

Pavlov, A., Kasting, J., Eigenbrode, J., and Freeman, K. 2001. Organic haze in Earth's early atmosphere: Source of low-^{13}C Late Archean kerogens? Geology, **29**: 1003-1006.

Pavlov, A., Kasting, J., Brown, L., Rages, K., and Freedman, R. 2000. Greenhouse warming by CH_4 in the atmosphere of early Earth. Journal of Geophysical Research, **105**: 11981-11990.

Petsch, S.T. 2003. The global oxygen cycle. *In* Geochemistry of Earth Surface Systems *Edited by* H.D. Holland and K. Turekian. Elsevier Science & Technology, , pp. 511-550.

Phoenix, V.R., Konhauser, K.O., Adams, D.G., and Bottrell, S.H. 2001. Role of biomineralization as an ultraviolet shield: Implications for archean life. Geology, **29**: 823-826.

Pokrovsky, O. and Schott, J. 2000. Kinetics and mechanism of forsterite dissolution at 25 ˚C and pH from 1 to 12. Geochimica et Cosmochimica Acta, **64**: 3313-3325.

Power, I.M., Wilson, S.A., Thom, J.M., Dipple, G.M., Gabites, J.E., and Southam, G. 2009. The hydromagnesite playas of Atlin, British Columbia, Canada: A biogeochemical model for CO_2 sequestration. Chemical Geology, **260**: 286-300.

Reid, R., Visscher, P., Decho, A., Stolz, J., Bebout, B., Dupraz, C., Macintyre, L., Paerl, H., Pinckney, J., Prufert-Bebout, L., Steppe, T., and DesMarais, D. 2000. The role of microbes in accretion, lamination and early lithification of modern marine stromatolites. Nature, **406**: 989-992.

Revsbech, N., Jorgensen, B., Blackburn, T., and Cohen, Y. 1983. Microelectrode studies of the photosynthesis and O_2, H_2S, and pH profiles of a microbial mat. Limnology and Oceanography, **28**: 1062-1074.

Saito, M.A., Sigman, D.M., and Morel, F.M.M. 2003. The bioinorganic chemistry of the ancient ocean: The co-evolution of cyanobacterial metal requirements and biogeochemical cycles at the Archean-Proterozoic boundary? Inorganica Chimica Acta, **356**: 308-318.

Santelli, C., Welch, S., Westrich, H., and Banfield, J. 2001. The effect of Fe-oxidizing bacteria on Fe-silicate mineral dissolution. Chemical Geology, **180**: 99-115.

Schidlowski, M. 1987. Application of stable carbon isotopes to early biochemical evolution on Earth. Annual Review of Earth and Planetary Sciences, **15**: 47-72.

Schidlowski, M., Eichmann, R., and Junge, C.E. 1975. Precambrian sedimentary carbonates: Carbon and oxygen isotope geochemistry and implications for the terrestrial oxygen budget. Precambrian Research, **2**: 1-69.

Schoell, M. and Wellmer, F. 1981. Anomalous ^{13}C depletion in early Precambrian graphites from Superior Province, Canada. Nature, **290**: 696-699.

Shiloh, M., Ruan, J., and Nathan, C. 1997. Evaluation of bacterial survival and phagocyte function with a fluorescence-based microplate assay. Infection and Immunity, **65**: 3193-3198.

Shirokova, L.S., Benezeth, P., Pokrovsky, O.S., Gerard, E., Menez, B., and Alfredsson, H. 2012. Effect of the heterotrophic bacterium *Pseudomonas reactans* on olivine dissolution kinetics and implications for CO_2 storage in basalts. Geochimica et Cosmochimica Acta, **80**: 30-50.

Spadafora, A., Perri, E., McKenzie, J.A., and Vasconcelos, C. 2010. Microbial biomineralization processes forming modern Ca:Mg carbonate stromatolites. Sedimentology, **57**: 27-40.

Stal, L.J. 2000. Cyanobacterial mats and stromatolites. *In* The Ecology of Cyanobacteria *Edited by* B.A. Whitton and M. Potts. Kluwer Academic, the Netherlands, pp. 61-120.

Strauss, H. and Moore, T.B. 1992. Abundances and isotopic compositions of carbon and sulfur species in whole rock and kerogen samples. *In* The Proterozoic Biosphere *Edited by* J.W. Schopf and C. Klein. Cambridge University Press, Cambridge, pp. 709-800.

Thomazo, C., Ader, M., Farquhar, J., and Philippot, P. 2009. Methanotrophs regulated atmospheric sulfur isotope anomalies during the Mesoarchean (Tumbiana Formation, Western Australia). Earth and Planetary Science Letters, **279**: 65-75.

Thompson, J. and Ferris, F. 1990. Cyanobacterial precipitation of gypsum, calcite, and magnesite from natural alkaline lake water. Geology, **18**: 995-998.

Tortell, P., Maldonado, M., and Price, N. 1996. The role of heterotrophic bacteria in iron-limited ocean ecosystems. Nature, **383**: 330-332.

Van Lith, Y., Warthmann, R., Vasconcelos, C., and Mckenzie, J.A. 2003a. Sulphate-reducing bacteria induce low-temperature Ca-dolomite and high Mg-calcite formation. Geobiology, **1**: 71-79.

Van Lith, Y., Warthmann, R., Vasconcelos, C., and McKenzie, J. 2003b. Microbial fossilization in carbonate sediments: A result of the bacterial surface involvement in dolomite precipitation. Sedimentology, **50**: 237-245.

Vasconcelos, C., Warthmann, R., McKenzie, J., Visscher, P., Bittermann, A., and van Lith, Y. 2006. Lithifying microbial mats in Lagoa Vermelba, Brazil: Modern Precambrian relics? Sedimentary Geology, **185**: 175-183.

Visscher, P. and Stolz, J. 2005. Microbial mats as bioreactors: Populations, processes, and products. Palaeogeography Palaeoclimatology Palaeoecology, **219**: 87-100.

Walker, J.C.G. 1977. Evolution of the atmosphere. Macmillan, New York.

Walker, J. 1987. Was the Archean biosphere upside down? Nature, **329**: 710-712.

Westall, F., Boni, L., and Guerzoni, E. 1995. The experimental silicification of microorganisms. Palaeontology, **38**: 495-528.

Wogelius, R. and Walther, J. 1992. Olivine dissolution kinetics at near-surface conditions. Chemical Geology, **97**: 101-112.

Zerkle, A.L., House, C.H., Cox, R.P., and Canfield, D.E. 2006. Metal limitation of cyanobacterial N_2 fixation and implications for the Precambrian nitrogen cycle. Geobiology, **4**: 285-297.

Zerkle, A.L., Claire, M., Domagal-Goldman, S.D., Farquhar, J., and Poulton, S. 2012. A bistable organic-rich atmosphere on the Neoarchaean Earth. Nature Geoscience, **5**: 359-363.

Chapter 3 A laboratory model of an Archean oxygen oasis with additions of ferrous iron

3.1 Introduction

In the Archean, the ocean was anoxic and contained a high concentration of dissolved iron, somewhere between 0.018 and 0.12 mM Fe^{2+} (Holland 1984; Canfield 2005). Oceanic iron sources included continental weathering, which most likely occurred at a rate similar to modern (Canfield 1998) and iron-rich hydrothermal vents, which are hypothesized to have been present during the Archean (Kump and Seyfried 2005). The largest iron sinks were the Archean and Paleoproterozoic iron formations (IFs) (3.8-1.8 Ga) that were deposited as alternating layers of ferric hydroxide and silica-rich chemical sediment on continental shelves (Trendall 2002). Minerals in IFs contain one of two or a mixture of iron oxidation states from ferrous-rich layers (siderite dominated) to ferric-rich layers (hematite dominated). Magnetite is also an abundant mineral in IFs. The amount of ferric iron in IFs (Fe^{3+}/ (Fe^{3+} + Fe^{2+})) ranges from 0.39 to 0.58, giving an average iron oxidation state for all IFs of +2.4 (Klein and Buekes 1992). Microbial activity has been proposed to play a vital role in the precipitation of both ferric and ferrous minerals in iron formations (Konhauser et al. 2002).

Cloud (1973) was the first to propose that cyanobacteria, using oxygenic photosynthesis, oxidized iron in an anoxic ocean to produce IFs. During periods of growth, excess oxygen from photosynthesis would produce a ferric hydroxide mud. During periods of low biological productivity pure silica was deposited, resulting in alternating iron and silica-rich bands. More recently, several researchers have proposed that oxygen was not needed to produce IFs and that phototrophic bacteria using Fe-based

anoxygenic photosynthesis could havw oxidized enough iron to account for IFs (Konhauser et al. 2002; Kappler et al. 2005).

Most of the ferrous minerals in IFs are the product of ferric hydroxide reduction during diagenesis and metamorphism (Ayres 1972). Thus, dissimilatory iron reduction by bacteria has been proposed as an important mechanism to produce ferrous minerals in Precambrian IFs, particularly for magnetite and some of the siderite (Nealson and Myers 1990; Konhauser et al. 2005). Evidence for the biogenic origin of magnetite includes magnetite overgrowths on hematite grains (Morris 1993; Pecoits et al. 2009) and the presence of carbonates with $\delta^{13}C$ values as low as -10‰ (Walker 1984). The presence of siderite with depleted δ^{56} Fe values in some late Archean IFs has also been interpreted as the result of FeRB (Johnson et al. 2008).

Both laboratory model and field studies have been used to determine potential mechanisms to produce IFs, as there is no modern equivalent process. Terrestrial hot springs have been proposed as one analog environment for the silicification of organisms found in the Gunflint chert (Walter et al. 1972; Konhauser and Ferris 1996). The precipitation and accumulation of iron oxides on a cyanobacterial mat from the Chocolate Pots hot springs of Yellowstone National Park had also been compared to Precambrian IFs (Pierson and Parenteau 2000; Trouwborst et al. 2007; Parenteau and Cady 2010). In a laboratory study, Konhauser et al. (2007) showed that UV photooxidation of iron could not have produced the ferric minerals in IFs but Fe-phototrophs and oxygen could. To test the hypothesis that Fe-phototrophs could produce the morphology of IFs, Posth et al. (2008) grew anoxygenic phototrophs in a silica and Fe-rich solution. The solution

produced bands of iron and silica when the temperature, and thus growth rate of the organisms, was varied (Posth et al. 2008).

The central question in this study is, what happened when average Archean seawater containing high ferrous iron entered oxygen oases present on Archean continental shelves? Using a mid-scale laboratory model, this study will explore the hypothesis that ferric minerals in IFs were produced by a reaction between dissolved ferrous iron and oxygen produced by cyanobacteria and that ferrous minerals were produced by dissimilatory iron reduction. This experiment is somewhat limited as a depositional model for IFs as it only considers the biogeochemistry of iron and not hydrothermally-sourced dissolved silica.

3.2 Methods

Experimental set-up

Experiments were performed in two 11 900 cm^3 air-tight plexiglass chambers (see Chapter 2 for chamber design). One chamber (Fe-OCM) contained an oxygenic cyanobacterial mat with associated aerobic heterotrophs, iron reducing bacteria (FeRB), sulphate reducing bacteria (SRB) and methanogens. The other chamber (Fe-BASE) was a baseline for changes in aqueous chemistry and used to determine a baseline value for atmospheric oxygen 'leakage' into the chamber and subsequent reaction with the added ferrous iron. Both chambers contained 3 600 cm^3 of forsterite sand (Fo_{90}), three 3 cm^3 fayalite-magnetite mineral keys and 4 700 cm^3 of artificial seawater from a previous experiment to model a late Archean oxygen oasis (Chapter 2). In this previous experiment, the cyanobacterial mat in OCM chamber was established over three months

and cyanobacterial growth was eventually limited by the availability of dissolved inorganic carbon. The original inoculated biota included *Oscillatoria* sp. with attached aerobic heterotrophs, *Shewanella oneidensis* MR-1, *Desulfovibrio* sp. and *Methanococcus voltae*. At the end of the previous experiment and at the start of the Fe-OCM experiment, the mat had a pH of 9.5 and contained precipitated Mg/Mn carbonates. A sulphide spot in the sediment had formed in the centre of the chamber. In the BASE chamber, a small amount of dissolution and serpentinization of the forsterite (F_{90}) sand surface had occurred (Chapter 2). In the previous experiment, no additions to either chamber were performed once the experiment was started and all accumulated dissolved iron in the chambers was from mineral dissolution. During sampling for the Chapter 2 experiment, the established atmospheres of both chambers were lost and the surface waters were exposed to oxygen for up to 8 hours.

To start the Fe-OCM experiment an additional litre of artificial seawater (Appendix B-1) was added to the chamber. The geochemistry was modified to create a more Archean-like environment by increasing the DIC (1.0060 g of $NaHCO_3$) and adding small amount of sulphate (0.0813 g of Na_2SO_4). From stock microbial cultures, 11 ml of SRB (*Desulfovibrio* sp.; Foster et al. 2010) in media (Appendix B-3) and 70 ml of methanogens (*Methanococcus voltae*) in media (Appendix B-4) was added directly into the sediment with a syringe to ensure that anaerobic bacteria survived the disturbance to the mat. To start the Fe-BASE experiment, an additional litre of artificial seawater and 0.0800g of Na_2SO_4 was added to the chamber. The oxygen was removed from the aqueous phase of both chambers by adding 0.57 g of ascorbic acid. Finally, both

chambers were sealed and the 3 600 cm^3 gaseous headspace was flushed with 100% $N_{2(g)}$ for 5 minutes.

To create a daily addition of 0.03 mM Fe^{2+} into the 5.78 L of seawater within the chamber, an anoxic concentrated Fe-seawater solution was injected through the surface water sampling port and then mixed with 'wave action'. Artificial anoxic seawater was made in advance and stored in 15 ml Al-crimp top serum vials sealed with butyl rubber stoppers. The seawater was made anoxic by adding 0.21 g ascorbic acid/L. Then, using a needle and syringe, 10 ml of anoxic seawater was injected in a 15 ml crimp top vial that had been flushed with 100% $N_{2(g)}$. Vials of anoxic seawater were stored in the fridge and were used within 15 days. Immediately prior to injection into the chamber, 0.0293 g of $FeCl_2 \cdot xH_2O$ was mixed with 5 ml of anoxic seawater in a 10 ml syringe. The solution was pushed into the chamber through the septa of the middle sampling port and then mixed in the chamber by lifting and lowering one side, which created waves in the surface water. The pH of the anoxic Fe-seawater solution before addition to the chamber was pH 6.5. The concentration of ferrous iron added in 0.0293 g of $FeCl_2 \cdot xH_2O$ was determined by ion coupled plasma atomic emission spectrometry (ICP-AES). The average molecular weight of the $FeCl_2 \cdot xH_2O$ was 187 g/mol(Appendix E), giving daily, added average concentration in the chamber of 0.03 mM Fe^{2+}. 0.03 mM of Fe^{2+} is within the range of dissolved iron calculated for average Archean seawater (0.018-0.072 mM Fe^{2+}) by Holland (1984) and close to the range in concentration (0.04-0.12 mM Fe^{2+}) calculated by Canfield (2005) both based on siderite saturation in the Archean. Over a twenty-four week period, 4.8199 g of $FeCl_2 \cdot xH_2O$ was added to the Fe-OCM chamber and 4.8774 g of $FeCl_2 \cdot xH_2O$ was added to the Fe-BASE chamber in total.

Fluid analysis

From the headspace sampling port, gas samples from both chambers were taken at least once every five weeks using the methodology described in Chapter 2. Gas samples were analyzed using micro-gas chromatography (μGC) with a Mole Sieve 5A and a Plot U column (Hewlett Packard Micro-GC P 200 with Agilent Cerity software). Using this system, the detection limit for $O_{2(g)}$ and $CO_{2(g)}$ was 0.5 % and 100 ppm, respectively.

Water samples were taken weekly from the sampling ports in the middle of the pore water and surface water of both chambers. Using a 20-gauge needle and a 10 ml syringe, 10 ml of water from each sample port was removed and discarded. Then at least 15 ml of sample was pulled through a fresh 20-gauge needle and 0.45 μm filter into a 30 ml syringe. Three ml of sample was used to determine dissolved oxygen concentration with either a 0-1 ppm or 1-8 ppm ChemMets dissolved oxygen ampoule and reference kit. Dissolved oxygen concentrations could not be determined when solutions contained high iron concentrations. Two ml of sample was used to determine pH with ColorpHast pH strips with a range of either 4.0 to 7.0 or 6.5 to 10. The remaining sample, at least 10 ml, was placed in a 15 ml Falcon tube and acidified with 300 μl nitric acid. Cation concentrations were determined by ion coupled plasma atomic emission spectrometry (ICP-AES) (Perkin-Elmer Optima 3300DV); phosphate concentrations and some of the sulphur concentrations were determined using ion cathode spectrometry (IC) (Dionex IC-3000) at the University of Western Ontario Biotron Analytical Chemistry Laboratory.

Mat and sediment sampling

After twenty-four weeks, the Fe-OCM chamber was opened to sample the mat and sediment. Opening the chamber did not result in any visible additional ferric

hydroxide precipitation in the water column. Water samples, the cyanobacterial pellicle, and the iron-enriched cyanobacterial mat were sampled using sterilized pipettes, tweezers and spatulas. Samples where fixed by mixing a 50:50 solution of sample in seawater from the chamber with 4% glutaraldehyde. Samples were stored in 15 ml Falcon tubes and 20 ml scintillation vials. After twenty-four weeks, ferrous iron was not added to the Fe-BASE surface water but the chamber was not opened for sampling until six weeks after the last iron addition.

Embedding samples

Several samples of mat were embedded in plastic using an EMbed 812 plastic kit (Electron Microscopy Sciences). Samples prepared for transmission electron microscopy (TEM) used the chemical ratio for a medium plastic and samples prepared for light microscopy and transmission electron microscopy (SEM) used the chemical ratio for hard plastic according to the manufacturer's instructions. TEM samples were not stained, i.e., fixed with metals during the embedding procedure. Pieces of mat prepared for light microscopy and SEM were stained for 1 hour with a $1\%_{(wt./vol.)}$ aqueous solution of osmium tetraoxide and then thoroughly rinsed with de-ionized water before embedding. All samples were dehydrated in acetone (25%, 50%, 75%, 100%, 100% and 100% acetone for 15 minutes each) and then the acetone was sequentially replaced with liquid plastic (50:50, 25:75 and 10:90 acetone to plastic for 1 hour each). The samples were left in 100% liquid plastic within a vacuum chamber overnight. The next day samples were covered in fresh plastic with the DMP-30 hardening accelerator and then cured in a vacuum chamber in the oven for 48 hr at 60 ˚C.

Microscopy

Two large samples of embedded mat were made into petrographic thin sections. Thin sections were imaged in bright field using a Zeiss Axio Imager Z1 Microscope. Large samples embedded in plastic were also cut and polished for backscatter secondary electron (BSE)-SEM. For BSE-SEM, the surface of the blocks were coated with 5 nm of osmium in a plasma coater (Filgen Plasma Coater 80T). These blocks were imaged at a voltage of 15 kV using the backscattered electron detector (QBSD) in a Leo Ziess 1540 scanning electron microscope (SEM). Scanning electron microscopy was also completed on whole mount mat samples. Pieces of mat were dehydrated with ethanol (25%, 50%, 75% and three times 100% for 15 minutes each) and then samples were then critical point dried (CPD) at 34˚C and 1100 kPa (Samdri PVT 3B critical point drier, Tousimis Research). CPD pieces of mat were mounted onto carbon sticky tape and then coated with 5 nm of osmium. These whole mount samples were imaged with a voltage of 3 kV using a Leo Ziess 1540 scanning electron microscope. The chemical composition of minerals in whole mount and embedded samples was determined at voltage of 15 kV using a INCA x-sight energy dispersive spectrophotometer (EDS) (Oxford Instruments) on the SEM. Electrons counts from EDS are not quantitative. The presence of C, O and Cl EDS peaks in embedded samples is from the plastic rather than the mat sample.

Small samples of mat embedded plastic were made in 100 nm thick thin sections using a diamond knife on an ultramicrotome. Thin sections were mounted on a 100 count Cu-formar grid and imaged at 80 kV on a Philips CM 10 transmission electron microscope (TEM).

3.3 Results

Geochemical changes in baseline experiment (Fe-BASE)

In the Fe-BASE experiment, the reported $O_{2(g)}$ concentration remained below 0.5% (Figure 3.1) but the actual $O_{2(g)}$ concentration was likely much lower as the gas sampling procedure leaked some atmospheric oxygen into samples. The dissolved oxygen concentration for the surface and pore water was < 1 ppm. Dissolved oxygen concentrations, especially low concentrations, were difficult to measure due to accidental inputs of small amounts of atmospheric oxygen, but some samples did report a $O_{2(aq)}$ value of 0.0 ppm. While the Fe-BASE atmosphere started with 100% $N_{2(g)}$, degassing of the aqueous phase towards equilibrium resulted in a $CO_{2(g)}$ concentration of 600 ppm after the first day (Figure 3.2). $CO_{2(g)}$ rose to 1800 ppm by day 7 and then dropped temporarily to 1300 ppm by week 2 and then gradually rose again to 2650 ppm by the end of the experiment.

In the first three weeks, the Fe-BASE surface water remained around pH 7 and the pore water decreased from pH 8.1 to 7.1 (Figure 3.3). From week 5 to 24, the surface and pore water pH was constant at 6.5. With an average daily addition of 0.03 mM of ferrous iron into the chamber, dissolved iron slowly and almost linearly increased from 0.005 to 2.22 mM in the surface water and from 0.006 to 1.26 mM in the pore water (Figure 3.4). The dissolved silica concentration fluctuated around 0.040 mM in the surface water and 0.080 mM in the pore water (Figure 3.5). Dissolved Mn data were only collected after week 5. Pore and surface water Mn exhibited the same trend and increased at a rate of ~$6x10^{-5}$ mM/day (Figure 3.6). The surface and pore water dissolved sulphur

concentration also exhibited the same trend and ranged between 0.15 and 0.20 mM (Figure 3.7).

By the end of the experiment, ~ 50% of the added ferrous iron was mineralized as a black precipitate (Fig 3.8a). The precipitate was not magnetic. Once exposed to oxygen during sampling, the black precipitate oxidized within a few days producing a rust colour. The mineralogy of the precipitate could not be determined due to rapid oxidation of ferrous iron in the solution. Some precipitates on sand grains observed under SEM (Figure 3.8b) appeared like a controlled solution of ferrous chloride in seawater reacted in a Falcon tube with atmospheric oxygen (Figure 3.8c).

Geochemical change in cyanobacterial mat experiment (Fe-OCM)

Starting with 100% $N_{2(g)}$ in the headspace, $O_{2(g)}$ in the Fe-OCM experiment rapidly increased to 4% by week 3 (Figure 3.1). Between week 3 and 24, $O_{2(g)}$ ranged between 3.8 and 4.5%, suggesting that cyanobacterial growth had entered a stationary phase. In the first fifteen weeks, $CO_{2(g)}$ was less than 300 ppm but then, from week 15 to week 24, $CO_{2(g)}$ increased from 130 to 2100 ppm (Figure 3.2).

In the Fe-OCM surface water, pH dropped from 8.1 to 6.5 in the first two weeks, then increased slightly to 7.1 by week 4 (Figure 3.3). After week 6, the pH ranged between 5.8 and 6.1. In the pore water, pH slowly decreased from 8.7 at day 1 to 6.5 at the end of the experiment. In the Fe-OCM surface water, the true concentration of dissolved iron was likely much less than the reported values from ICP-AES (Figure 3.4a). During sampling, small nano-phase iron particles, commonly observed using SEM, could have easily passed through the 0.45 μm filter and thus particles were falsely reported as dissolved iron (Raiswell and Canfield 2012). While collecting water samples from the

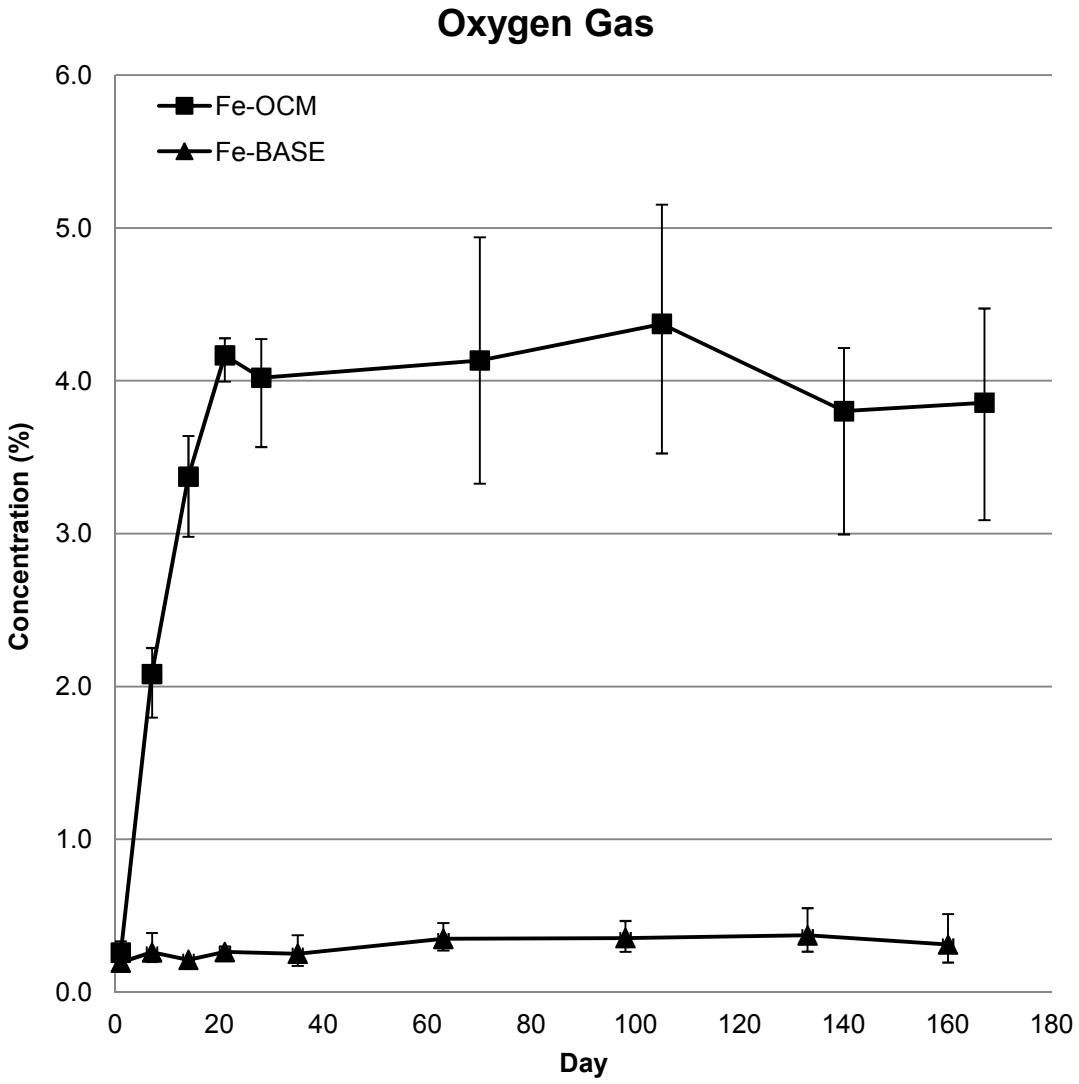

Figure 3.1 Oxygen gas in the headspace of the Fe-OCM chamber rapidly increased and then plateaued after day 21. Oxygen gas in the headspace of the Fe-BASE chamber remained very low throughout the experiment. Error bars show minimum and maximum values.

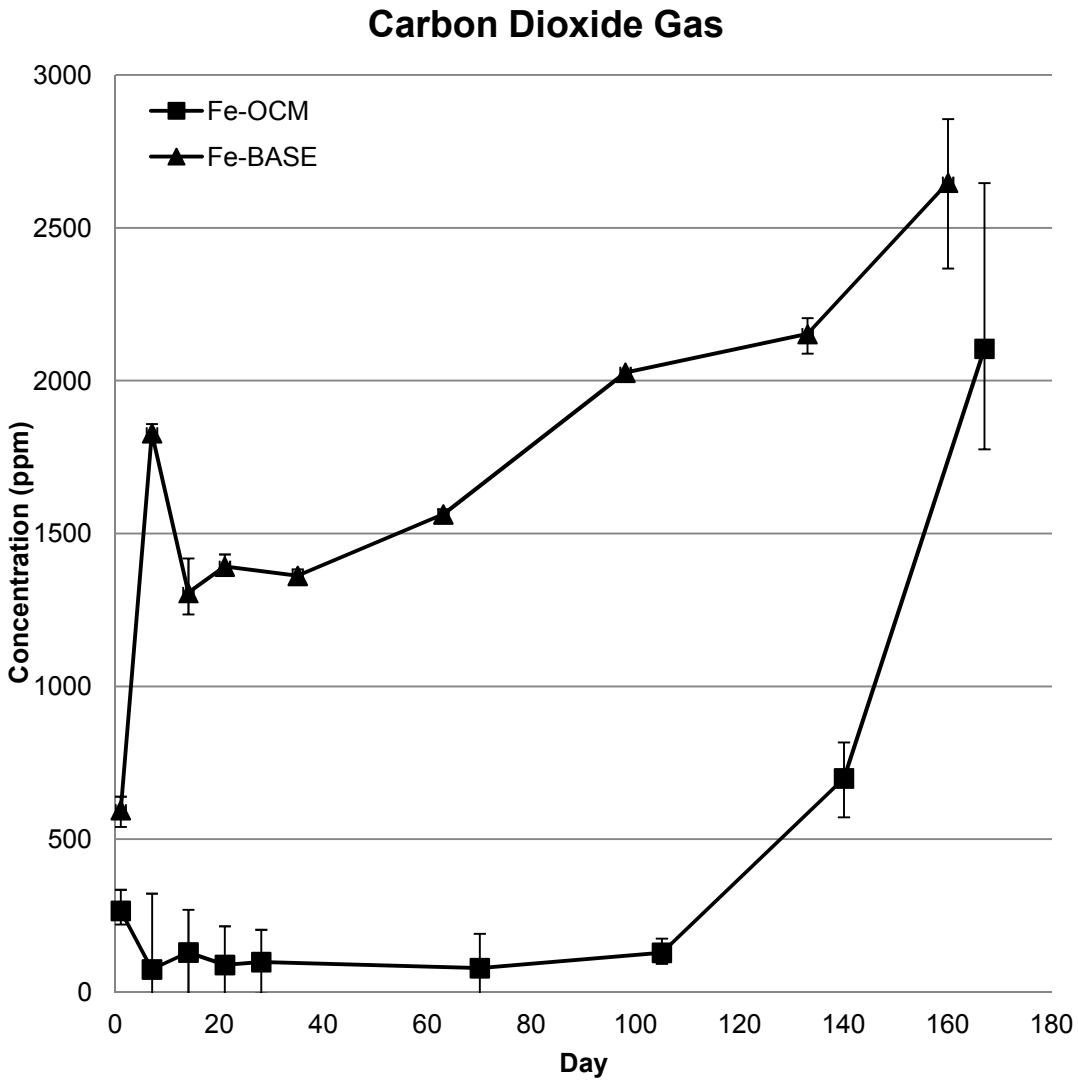

Figure 3.2 Carbon dioxide gas in the headspace of both the Fe-OCM and Fe-BASE chamber increased over the experiment. Error bars show minimum and maximum values.

surface water, filters became covered in a layer of ferric hydroxides. In the Fe-OCM pore water, the reported concentrations of dissolved iron may also be due to 'contamination' by < 0.45 μm ferric hydroxide particles, but as much fewer precipitates were observed on the filter during collection, reported iron values are likely close to true concentrations for the pore water. Dissolved iron in the pore water remained below 0.02 mM until week 15 and then increased to 0.1 mM by week 23 (Figure 3.4b).

The surface water dissolved silica remained below 0.025 mM until week 19 and then increased to 0.055 mM at the end of the experiment. Pore water dissolved silica ranged between 0.04 and 0.11 mM (Figure 3.5). Until week 22, Mn in the surface and pore water remained below 0.02 mM (Figure 3.6). Mn increased slowly between week 17 and 22 and then rapidly increased to 0.04 mM in the last two weeks of the experiment. At day 1, phosphate in the surface water was 0.20 mM and then phosphate decreased below the detection limit. As such, dissolved phosphate was only measured for the first five weeks of the experiment. Dissolved sulphur in surface and pore water ranged between 0.22 and 0.32 mM, decreasing slightly after week 3 (Figure 3.7).

Mat morphology and iron distribution

The wave action method of mixing ferrous iron into the chamber resulted in ~0.5 cm high ripples forming on the Fe-BASE sand surface (Figure 3.8a). In contrast, the presence of a cyanobacterial mat containing ferric hydroxides on the Fe-OCM sand surface prevented the formation of ripples (Figure 3.9a). The cyanobacterial mat extended ~1 mm thick above the sand surface. Below the sand surface, a matrix of extracellular polymeric substances (EPS) held the sand grains together to a depth ranging from 1 to 3 mm. The microbial mat both above and below the sand was much more

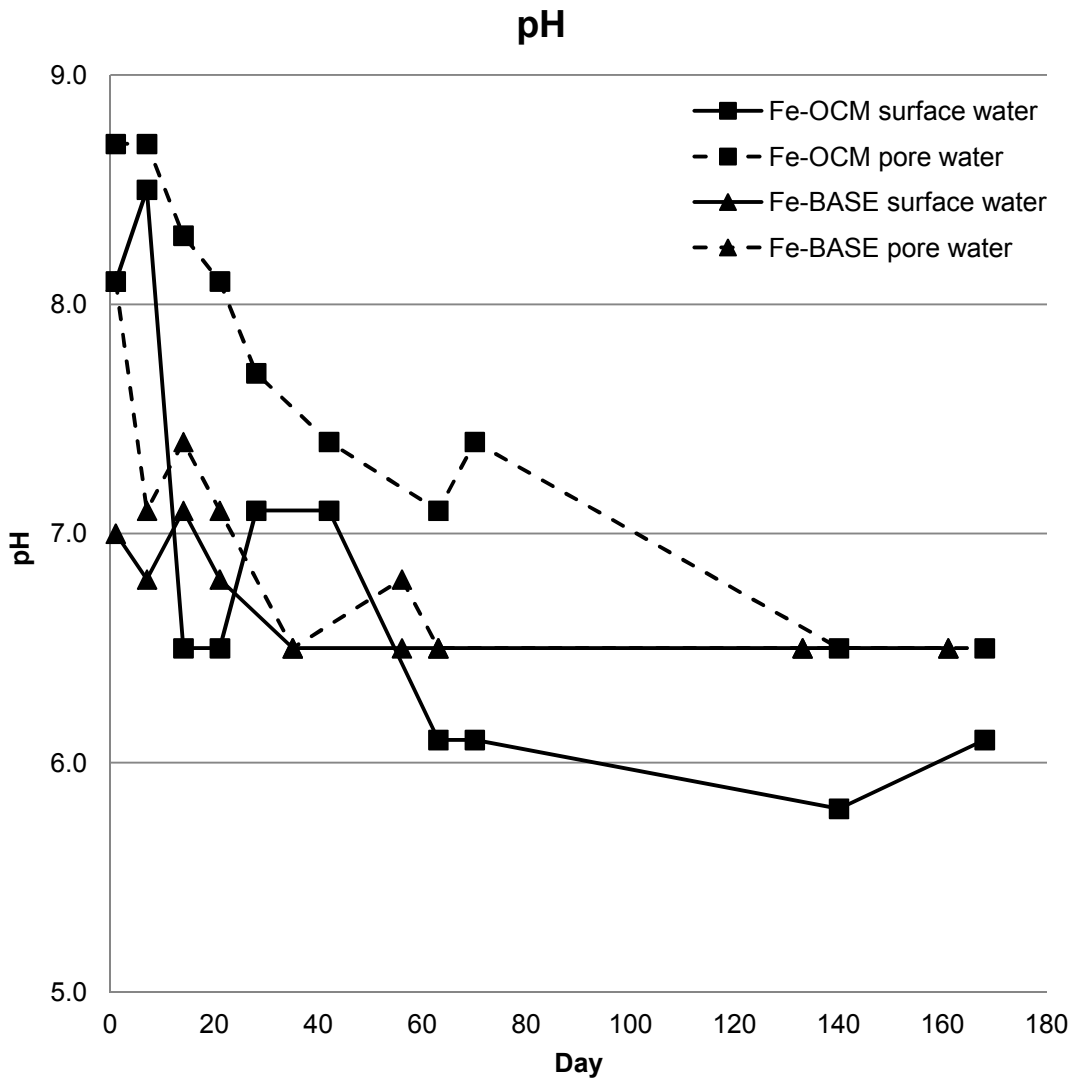

Figure 3.3 The pH of the surface and pore water of the Fe-OCM and Fe-BASE chamber decreased over the experiment.

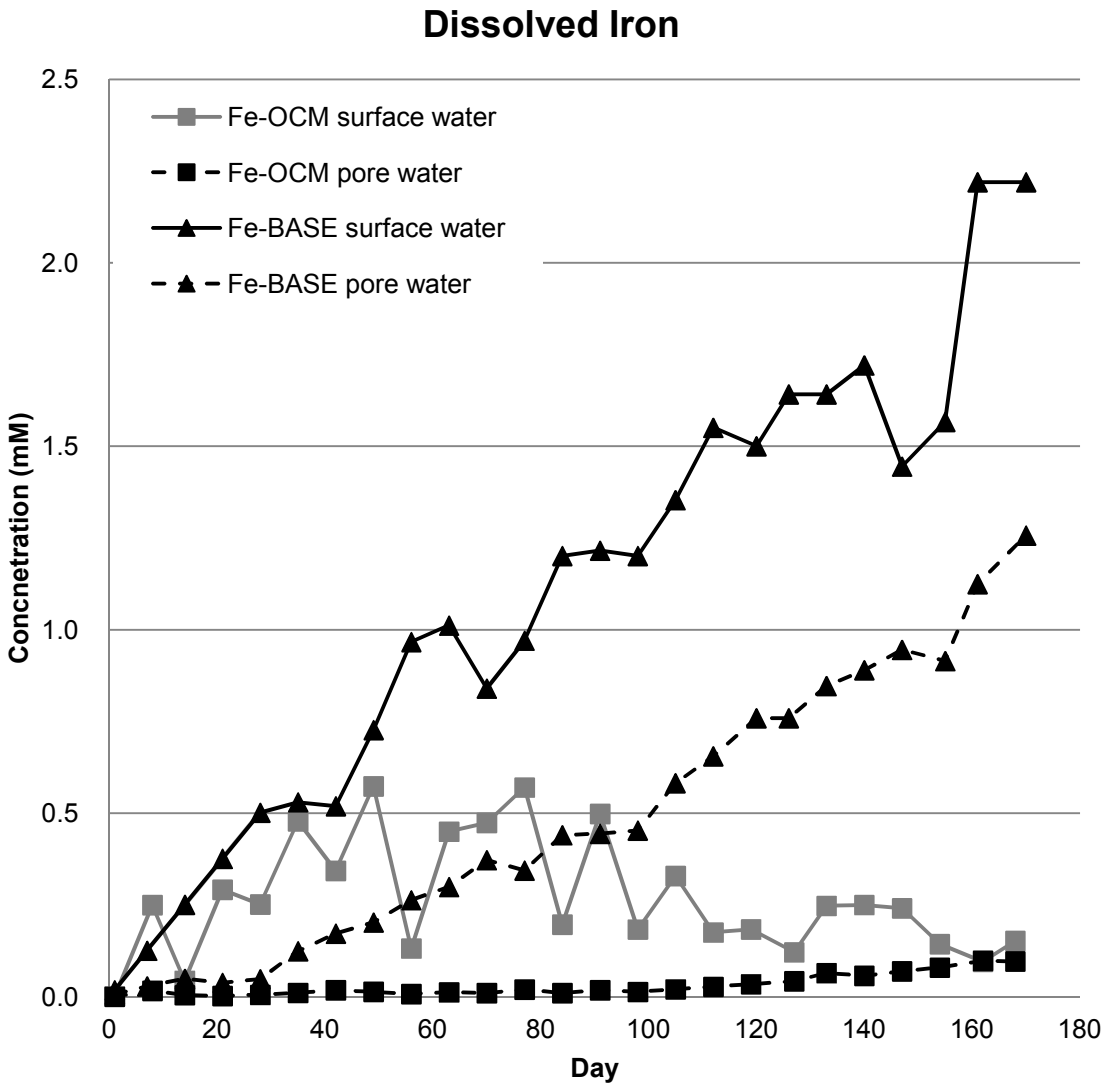

Figure 3.4a The dissolved iron of the surface and pore water of the Fe-OCM and Fe-BASE chamber increased through the experiment. 0.03 mM of Fe^{2+} was added to each chamber daily. The reported surface water values of the Fe-OCM chamber (in grey) is most likely much higher than the true dissolved iron concentration due to nano-sized iron particles going through the filter.

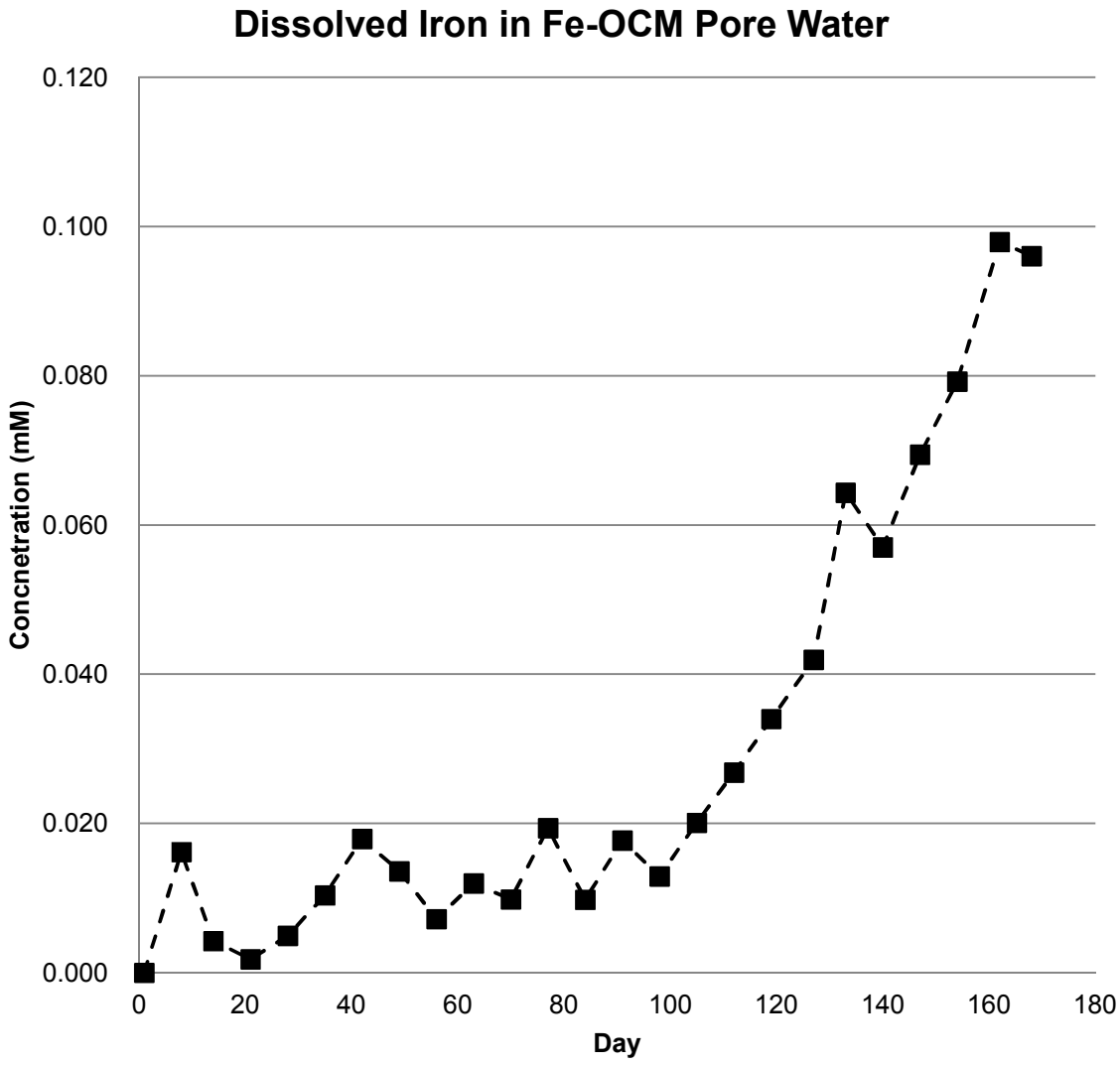

Figure 3.4b A close up of the dissolved iron in the Fe-OCM pore water. The iron concentration increased after day 105.

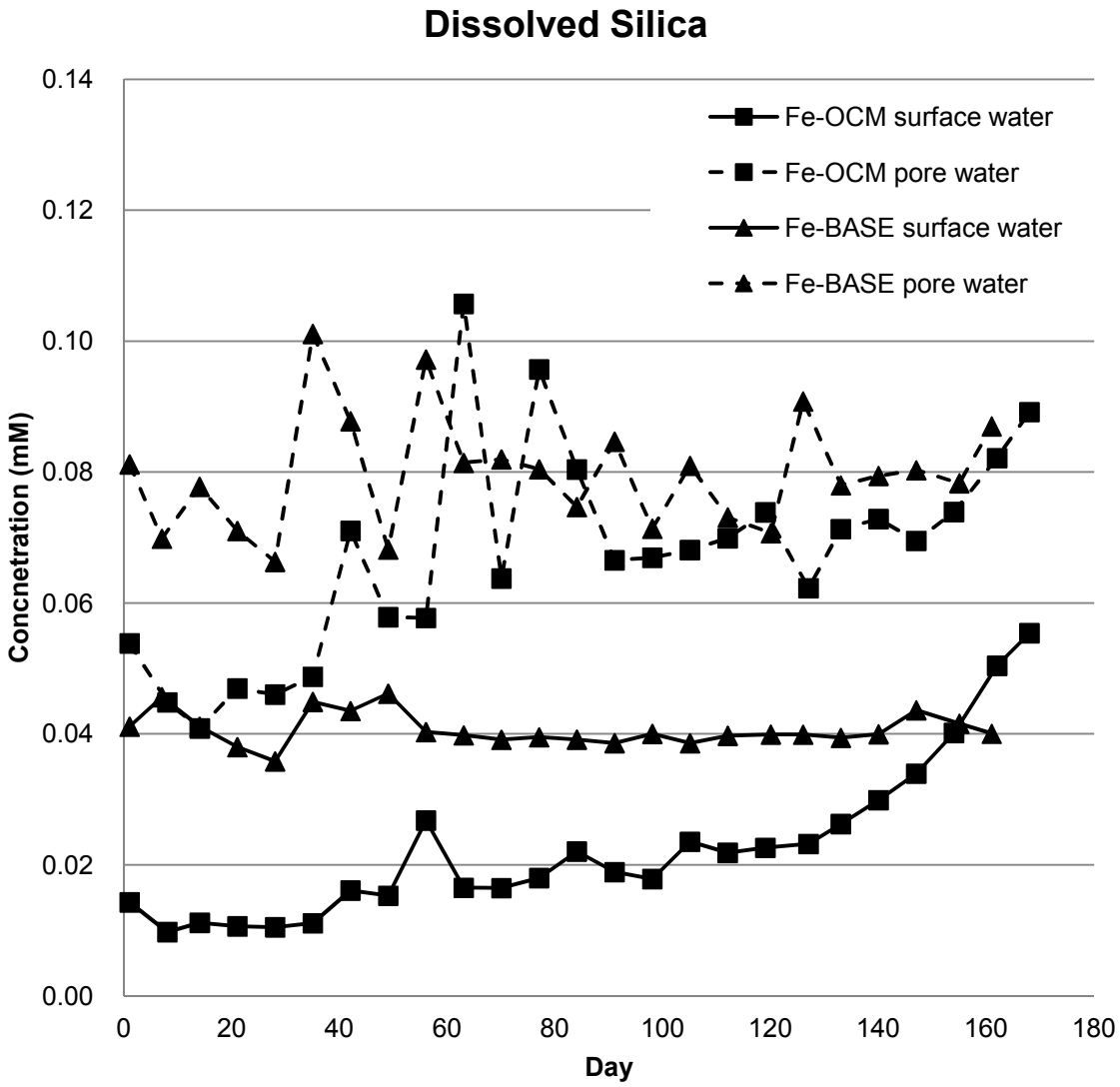

Figure 3.5 Dissolved silica in the surface and pore water of the Fe-OCM and Fe-BASE chamber.

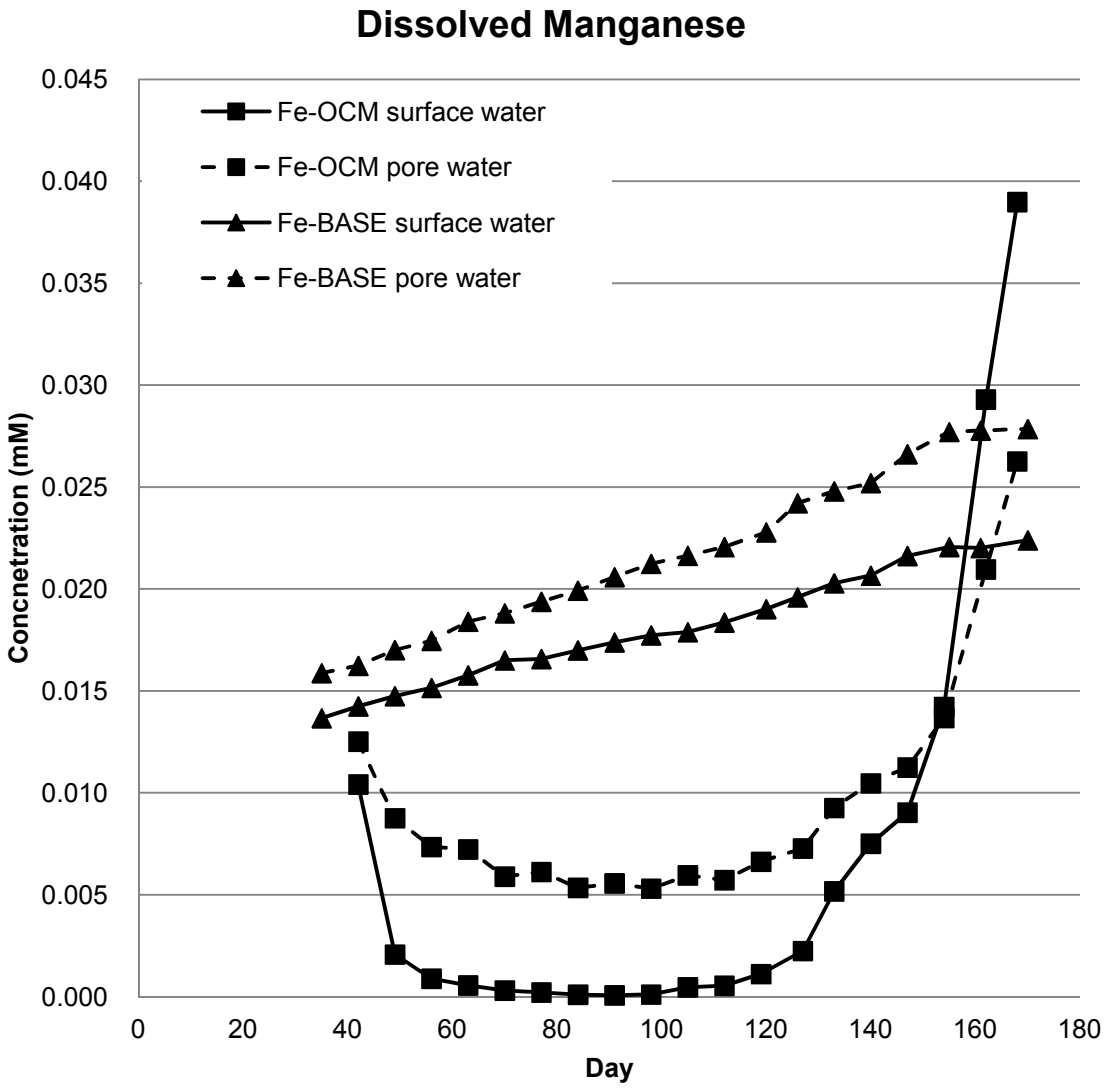

Figure 3.6 Dissolved manganese in the surface and pore water of the Fe-OCM and Fe-BASE chamber.

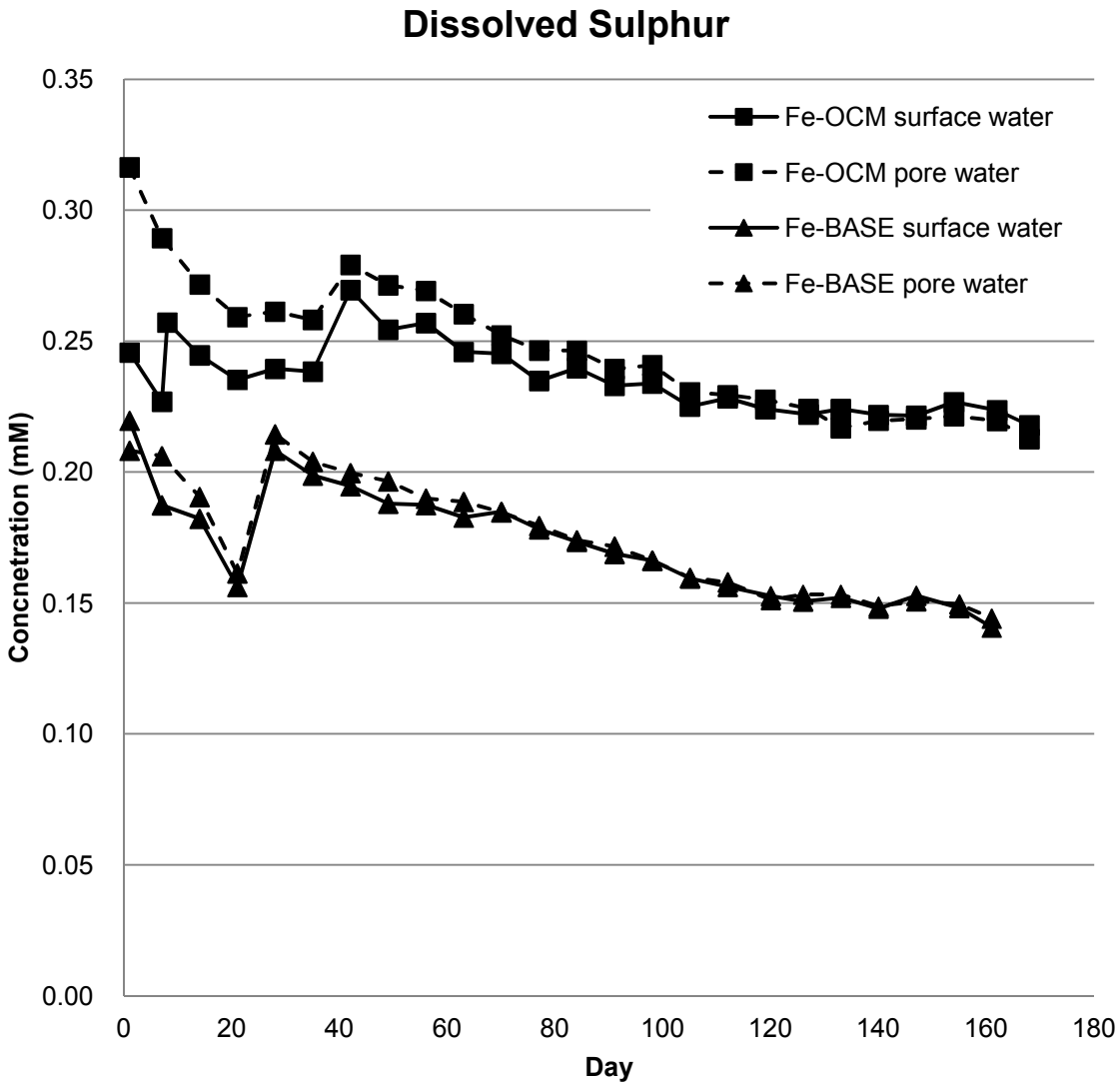

Figure 3.7 Dissolved sulphur in the surface and pore water Fe-OCM and Fe-BASE chamber. The small change in sulphur in the Fe-OCM chamber suggests sulphate reduction and formation of iron sulphide precipitates was limited. For the first five weeks, dissolved sulphur was measured with IC. All other samples were measured with ICP-AES.

rigid and cohesive than at the end of the experiment compared to the start. The surface of the mat also exhibited several macroscopic features that were not present at the start of the experiment, including large and small, trapped air bubbles (Figure 3.9b and 3.9c), and ridges and hollows (Figure 3.9d). Based on the red colour of the surface of the mat, ferric hydroxides were relatively evenly distributed, except few ferric hydroxides were present immediately above the sulphide spot (Figure 3.9a). Cyanobacteria on the top some of the larger trapped air pockets appeared to have slightly less iron on the surface than the surrounding mat (Figure 3.9b), whereas, cyanobacteria on the top of the small trapped bubbles appeared to have more iron (Figure 3.9c). The walls of the chamber also were covered in a layer of cyanobacteria and some pieces of mat were floating within the water column. During sampling, discrete layers of laminated mat could be peeled away in some areas of the chamber, but in general, the mat was completely consolidated. When a piece of mat was dissected under a stereoscopic microscope, bright red nodules were observed at the bottom of a trapped air bubble (Figure 3.9e), at lower depth in the mat within the EPS and attached to sand grains (Figure 3.9f).

Petrographic thin sections of embedded mat showed more ferric hydroxides were present at the top of the mat than at depth (Figure 3.10). The top half of the mat also contained many voids. On the bottom of some of these voids, greater amounts of ferric hydroxides had accumulated relative to the surrounding mat. In general, cyanobacterial filaments were perpendicularly oriented relative to the planar orientation of mat growth.

Embedded mat examined using BSE-SEM also highlighted the iron gradient in the mat (Figure 3.11a). Ferric hydroxide colloids were ubiquitous throughout the biofilm and outlined the cyanobacterial filaments (Figure 3.11b). Some higher density ferric

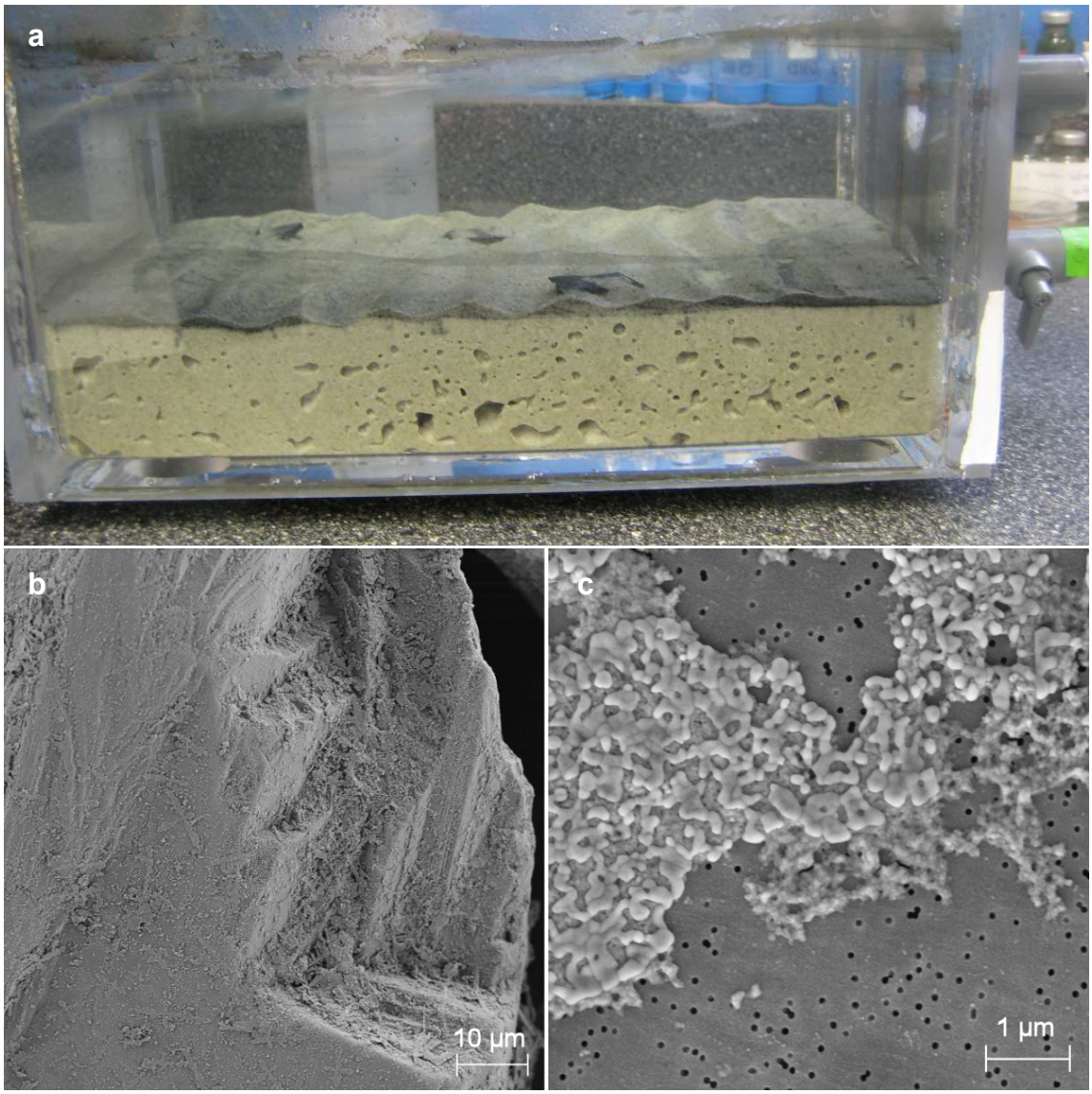

Figure 3.8 a) Side view of chamber and the black precipitate formed in the Fe-BASE experiment. Ripples are formed from the daily mixing process. The chamber length is 30cm. **b)** SEM photomicrograph of sand from black precipitate layer. Surface alteration was cumulative through a three month low iron experiment (Chapter 2), the five month Fe-BASE experiment and oxidation of some ferrous iron and precipitation during sampling. **c)** Precipitates formed when solution of 0.05 g $FeCl_2 \cdot xH_2O$ and 5 ml of artificial seawater were exposed to atmospheric oxygen. Precipitates were filtered onto a 0.1 µm filter and then air dried before imaging.

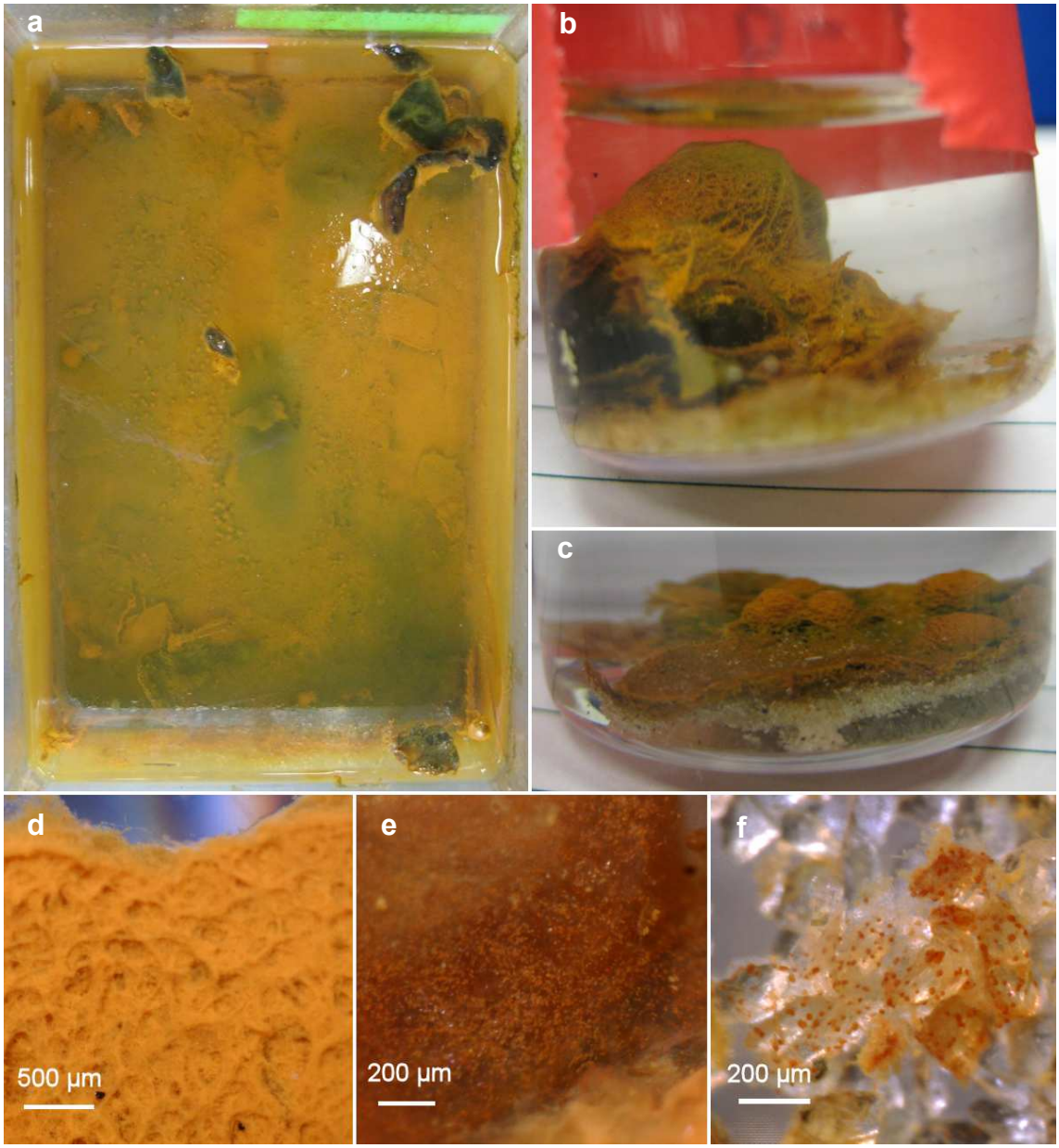

Figure 3.9 a) Top view of the Fe-OCM chamber with an iron mineralized mat on the surface of the sand. The greenish spot in the centre of the chamber is underlain with black sulphidic sediment. Chamber length is 30 cm. **b)** A large cyanobacterial mat enclosed bubble collected from immediately below the ferrous iron injection port. The diameter of the vial is 23 mm. **c)** Small cyanobacterial mat enclosed bubble collected from the middle of the chamber. **d)** Surface of the mat viewed under a stereoscopic microscope. **e)** Iron nodules in EPS from below a small cyanobacterial mat trapped bubble. **f)** Iron nodules attached sand grains that is held in a matrix of EPS.

hydroxide colloids were also observed near the surface of the mat. SEM-EDS showed these ferric hydroxides did not contain any other metals (Figure 3.11c). The iron nodules observed using light microscopy (Fig 3.9e, 3.9f, and 3.10) were shown to be hollow using SEM (Figure 3.11c and 3.11d). Nodules were more common in lower depths of the mat and were also found attached to sand particles. The outer diameter of these nodules ranged in size from 5 to 12 μm. The diameter of the 'hollow' interiors ranged from 3 to 6.5 μm, and contained a slight higher concentration of Os than the surrounding ferric hydroxide colloids and plastic. These nodules were highly concentrated in iron relatively to the ferric hydroxide colloids. Some of the nodules also had substantial amount of manganese (Figure 3.11d), with a Mn:Fe mole ratio of up to 5.7:1. Some of the nodules did not contain any Mn. Most of the nodules had a single ring of concentrated metals but some the nodules contained two rings. Nodules were also observed in the samples of the cyanobacterial mat floating in the water column.

One embedded piece of mat examined using SEM highlighted a deeper section of the mat possessing a concentrated area of iron (Figure 3.12a). Fossilized cells, both cyanobacteria and heterotrophs, and large (> 10 μm) denser iron precipitates were also present in this area (Fig 3.12b-d). In one cross-section of a cyanobacteria fossil, the entire cell envelope had been preserved in iron rather than iron only precipitating on the outside of the cyanobacterial sheath (Figure 3.13). In general, this deep area of mat contained more consolidated, denser iron precipitates than the ferric hydroxides colloids observed at the top of the mat. Some of the precipitates had a blocky texture (Figure 3.12d). This area of mat also contained < 1 μm precipitates high in Ca, likely Ca-carbonates.

In whole mounts imaged by SEM, macroscopic surface hollows were found to be formed by parallel filaments of cyanobacteria (Figure 3.14a). At the surface of the mat, ferric hydroxides colloids (< 500 nm) were trapped in the abundant EPS. Heterotrophs with diverse morphologies were also present. In some locations, cyanobacteria had left their mineralized sheath, resulting in a filamentous cast (Figure 3.14b). At depth in the mat, ferric hydroxide colloids occurred as large clumps or covered sand grains and the sheaths of cyanobacteria (Fig 3.14c and 3.14d). Heterotrophic cells with a rod morphology were closely associated the ferric hydroxides and cyanobacteria, whereas, cells with a coccoid or vibroid morphology were only observed on forsterite sand grains. In some areas of the mat, rod-shaped heterotrophs were abundant (Figure 3.15a and 3.15b). When ferric hydroxide colloids were attached to these cells, there was a preferential attachment to the ends of the rod. Ferric hydroxide colloids collected from the surface water and from within the cyanobacterial mat had a similar morphology. Ferric hydroxides precipitated as < 100 nm crystals, which aggregated to form < 0.5 μm spherical colloids (Figure 3.15c). These colloids were often aggregated together as well. Few iron particles were observed within the sediment under the mat but sand grains were covered in EPS, heterotrophs and organic spheres, as small as 100 nm (Figure 3.15d)

A gradient of high to low amounts of ferric hydroxide precipitates with depth in the mat was also observed in ultra-thin sections imaged using TEM. TEM showed that iron mineralization on cyanobacteria was primarily occurring by attachment of the iron colloids to the outside of cyanobacterial sheaths (Figure 3.16a). Complete mineralization of the exterior of cyanobacteria was rare. Heterotrophs throughout the mat were also

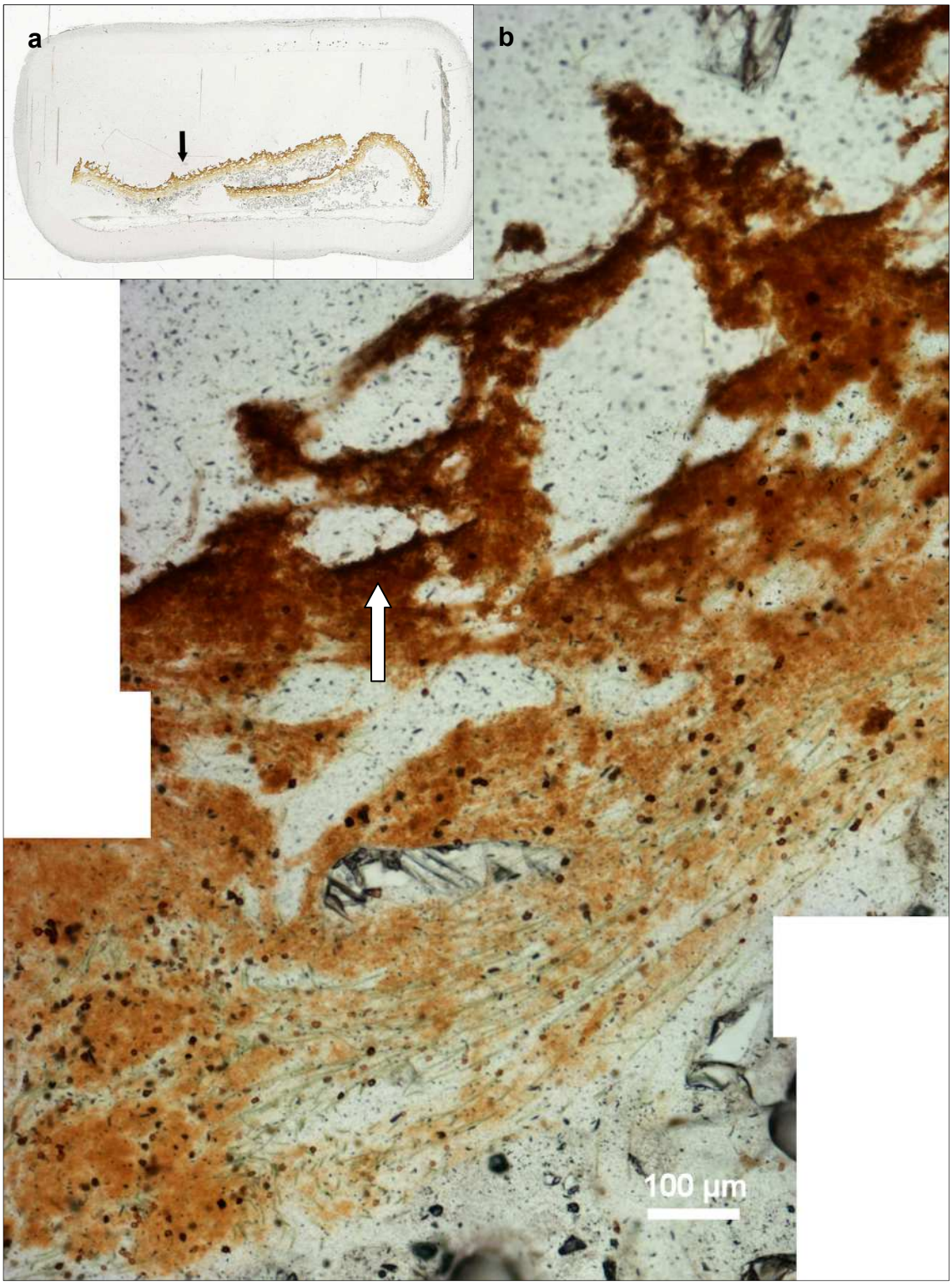

Figure 3.10 a) A petrographic thin section of an embedded cyanobacterial mat. Arrow shows location of the cross section. **b)** A cross section of the mat shows a preferential accumulation of ferric hydroxides in the top portion of the mat. Ferric hydroxides are also accumulated at the bottom of some voids within the mat (white arrow).

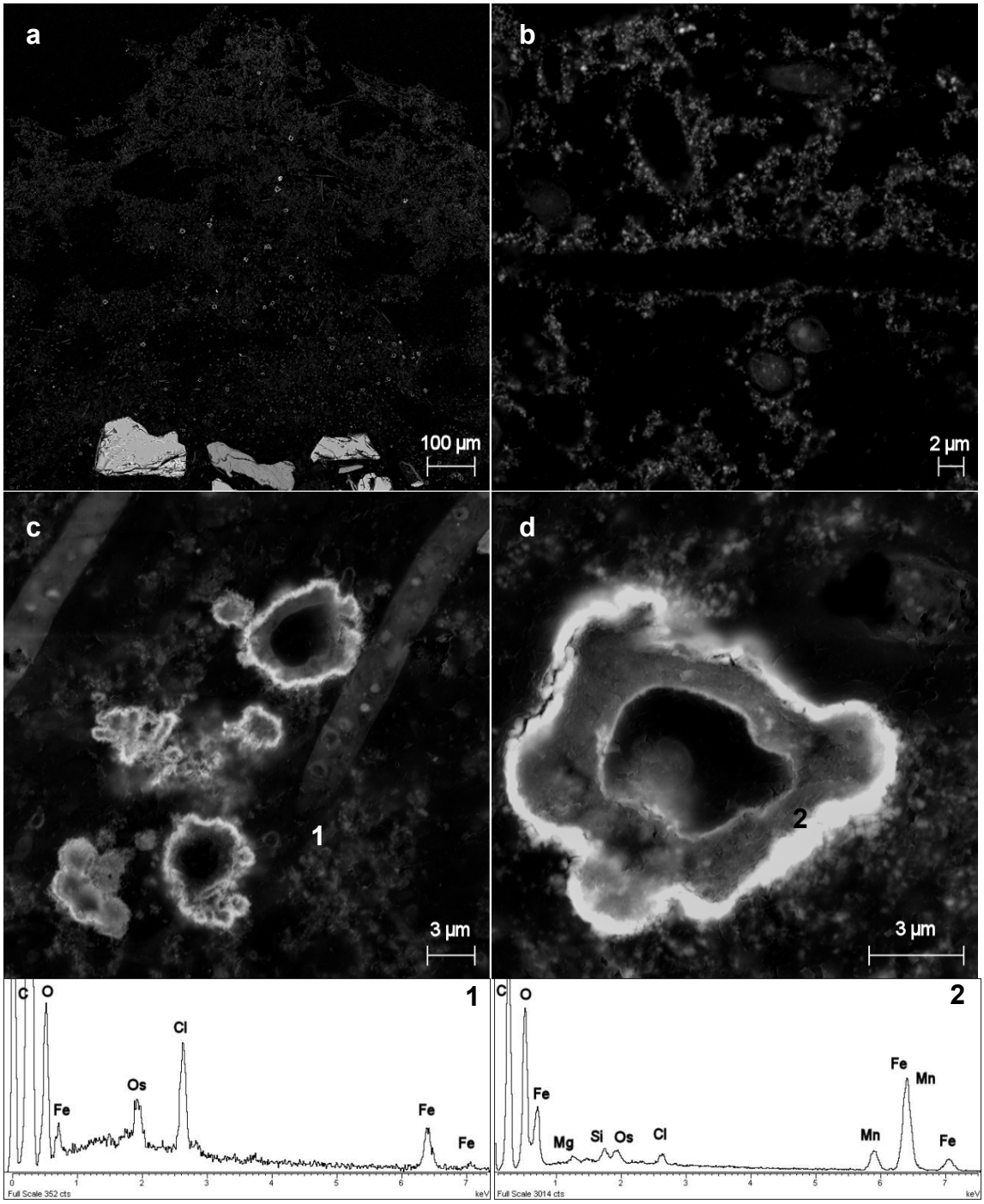

Figure 3.11 a) Cross section of the embedded mat using a back scattered electron detector in SEM. Less dense solids (*i.e.* plastic) appear dark and more dense solids appear bright. **b)** Outlines of cyanobacteria show ferric hydroxides have precipitated on the cyanobacterial sheaths. Cyanobacterial cells appear in polished sections as they were stained with OsO_4. **c)** Nodules of concentrated iron are hollow in cross section. Here nodules are associated with iron mineralized heterotrophs. EDS shows signal of the ferric hydroxides and coated plastic (C, O, Cl and Os) **d)** This double ringed nodule contains organics stained with OsO_4 in the hollow centres and is composed of Fe and Mn.

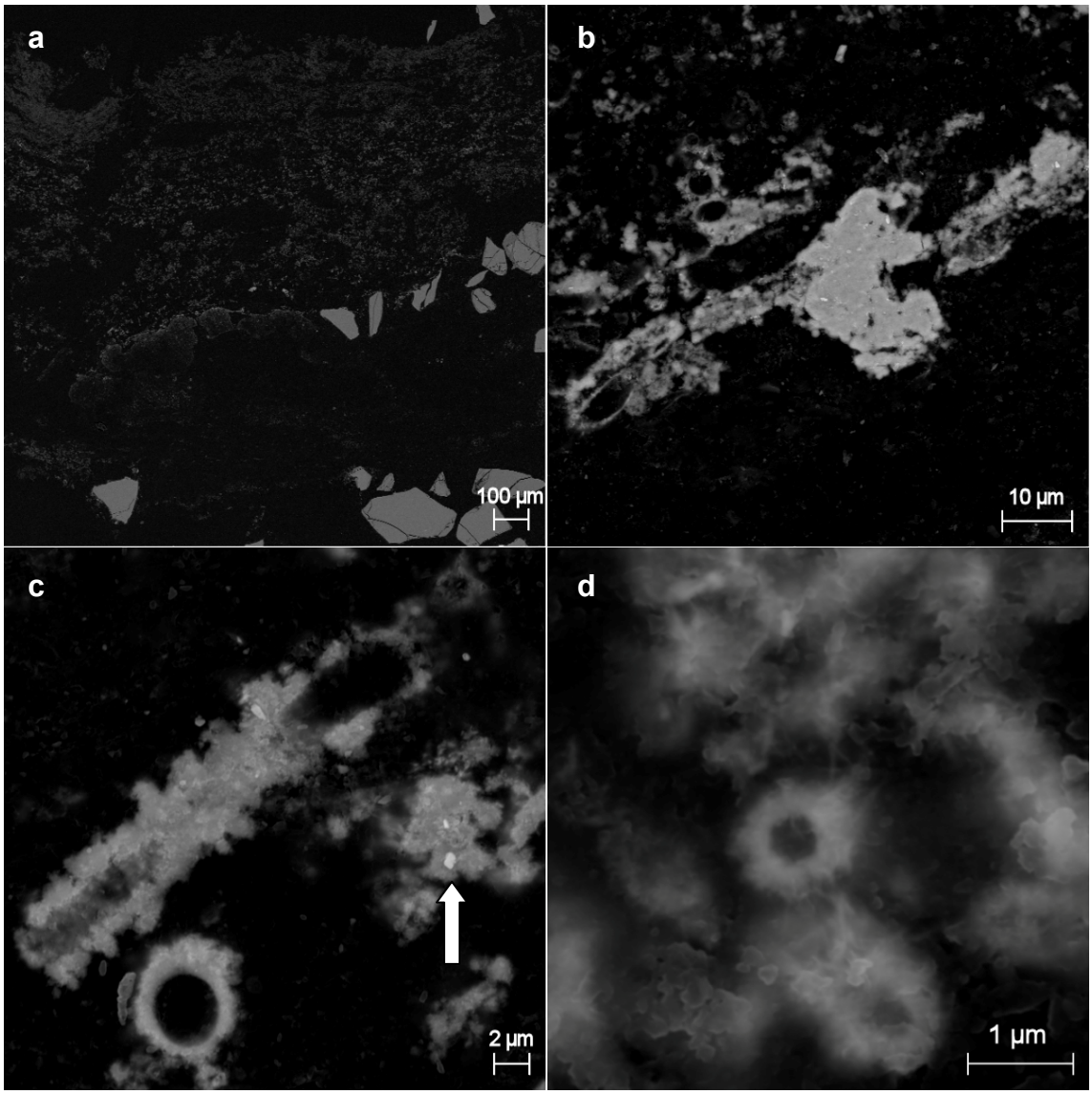

Figure 3.12 a) A cross section of mat shows iron had accumulated at depth, as well as, at the surface of the mat. **b)** A large dense iron precipitate is associated with a fossilized cyanobacteria. Rod-shaped heterotrophs are also preserved in iron adjacent to the cyanobacteria. **c)** Precipitates, including those on cyanobacteria, have a more block texture compared to the iron colloids found near the top of the mat. The spherical feature is cyanobacterial filament oriented perpendicular to the polished surface. Brightest particles (arrow) contains Ca. **d)** Heterotrophs outlined in iron from within the mat.

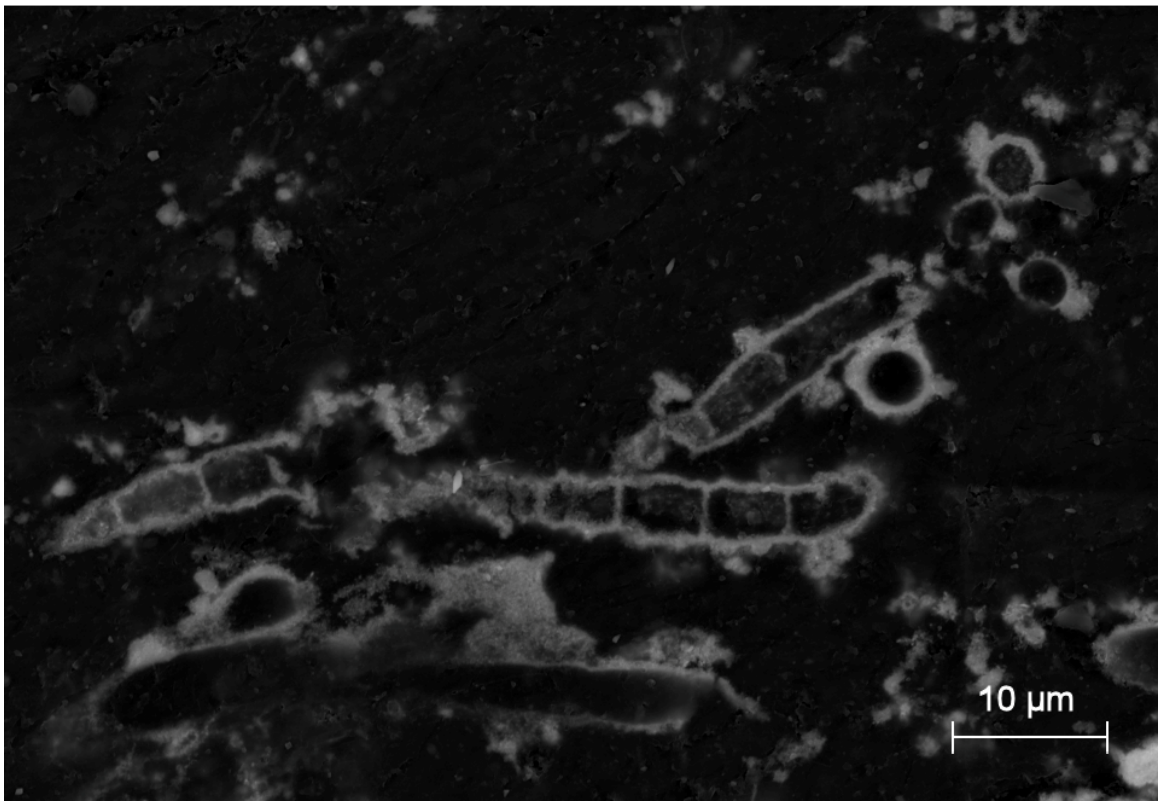

Figure 3.13 Cyanobacteria cells outlined in a relatively thick coating of iron. This photomicrograph is a close up of the area immediately above the iron-rich blobs in Fig. 12a. Area is 0.7 mm into the mat, almost at the sand surface.

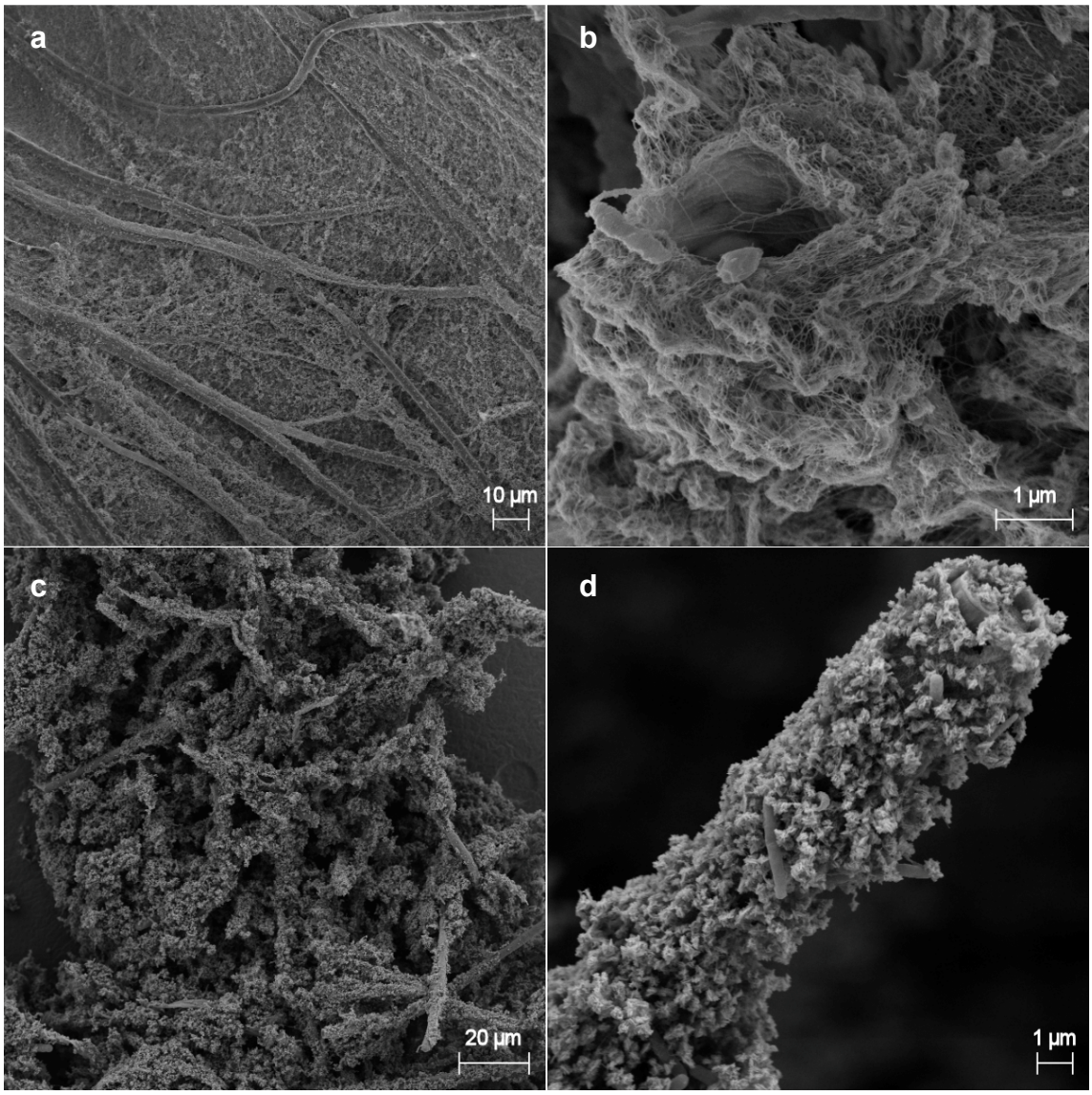

Figure 3.14 a) Whole mount image of top of cyanobacterial mat showing oriented filaments of cyanobacteria **b)** A heterotroph on the mineralized cast of a cyanobacteria. Ferric hydroxides are trapped in the EPS. **c)** Cyanobacteria within the mat are covered in abundant ferric hydroxide precipitates. **d)** The cyanobacterial cell is protected by the growth of a sheath. Two FeRB are attached to the cyanobacteria.

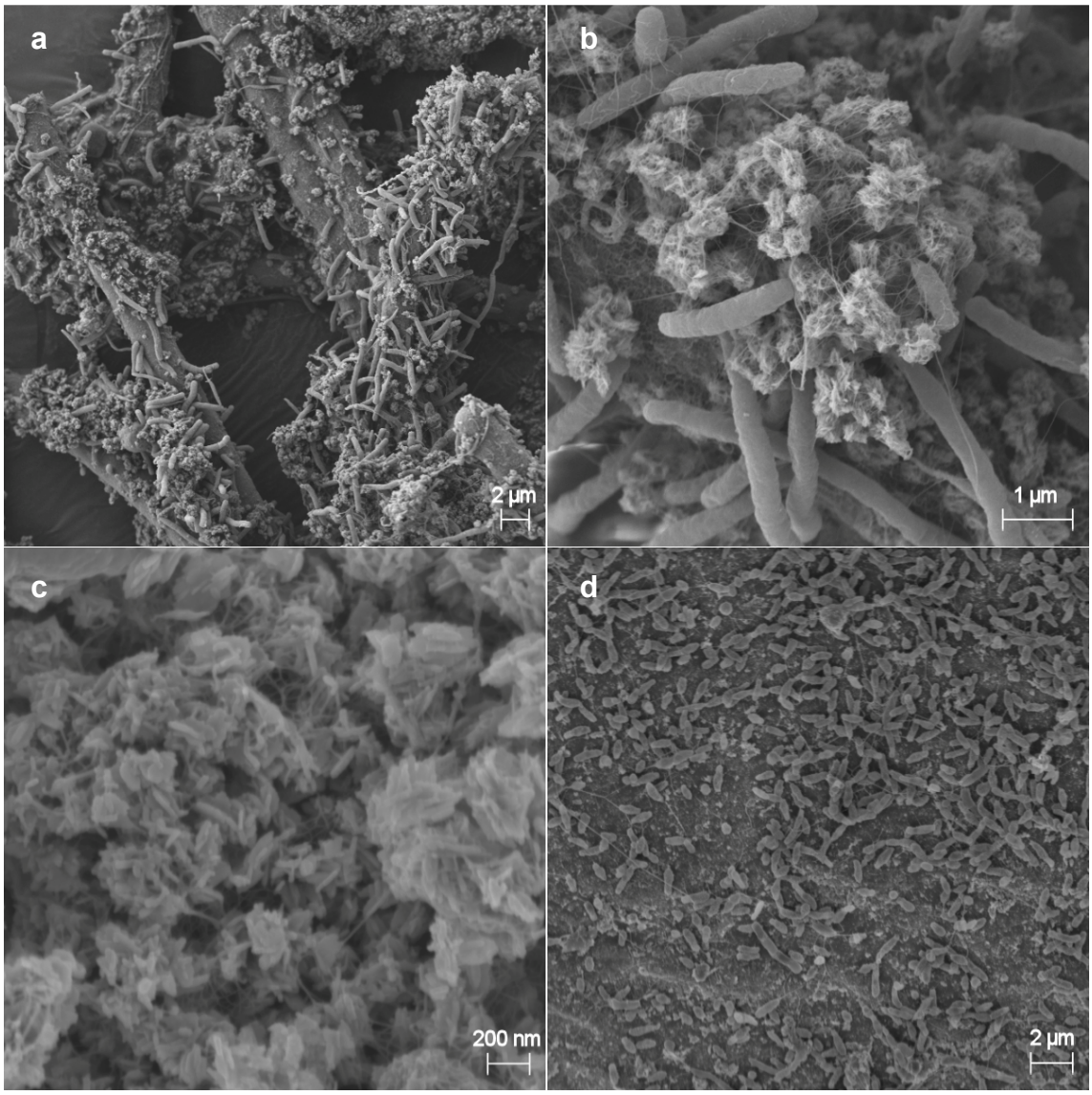

Figure 3.15 a) Abundant heterotrophs, likely FeRB, are attached to partially mineralized cyanobacteria. **b)** Close up of heterotrophs and ferric hydroxide colloids on a cyanobacteria. **c)** Close up of ferric hydroxide colloids within the mat. **d)** Organics and heterotrophs attached to a sand grain from within the sediment.

being outlined by attached iron particles. On heterotrophs, the iron often completely coated the cell with a layer of iron crystals several tens of nanometres thick. Remarkably, fine-grained iron also precipitated within some of the cyanobacterial cells on the thylakoid membranes, even though the outside of the cell was not heavily mineralized (Figure 3.16b). Some larger organic structures, similar in size to the nodules observed in SEM, were also observed in TEM (Figure 3.16c). These organics were covered a thicker (~500 nm), more consolidated layer of iron precipitates (Figure 3.16d).

3.4 Discussion

Fe-BASE geochemical changes

The low concentration of gaseous and dissolved oxygen and lack of ferric hydroxides in the Fe-BASE chamber showed atmospheric oxygen did not enter into the system despite the daily injections of a Fe-seawater solution. However, the ascorbic acid, a reducing agent added to make the seawater anoxic, may have reacted with the ferrous iron. The mineralogy of the iron precipitate could not be determined, as after opening the chamber ferric hydroxides immediately precipitated from the seawater onto the sand. A minimal change in the dissolved sulphur concentration suggests the precipitate was not pyrite. Dissolved iron increased in the Fe-BASE surface water at an average rate of 0.013 mM/day. The pH of the surface water dropped from 8.1 to 6.5 because Fe^{2+} complexes with hydroxide ions.

Fe-OCM geochemical changes

In the Fe-OCM surface water, geochemical changes were dominated by the cyanobacteria undergoing oxygenic photosynthesis (Equation 3.1) and by the ferrous iron

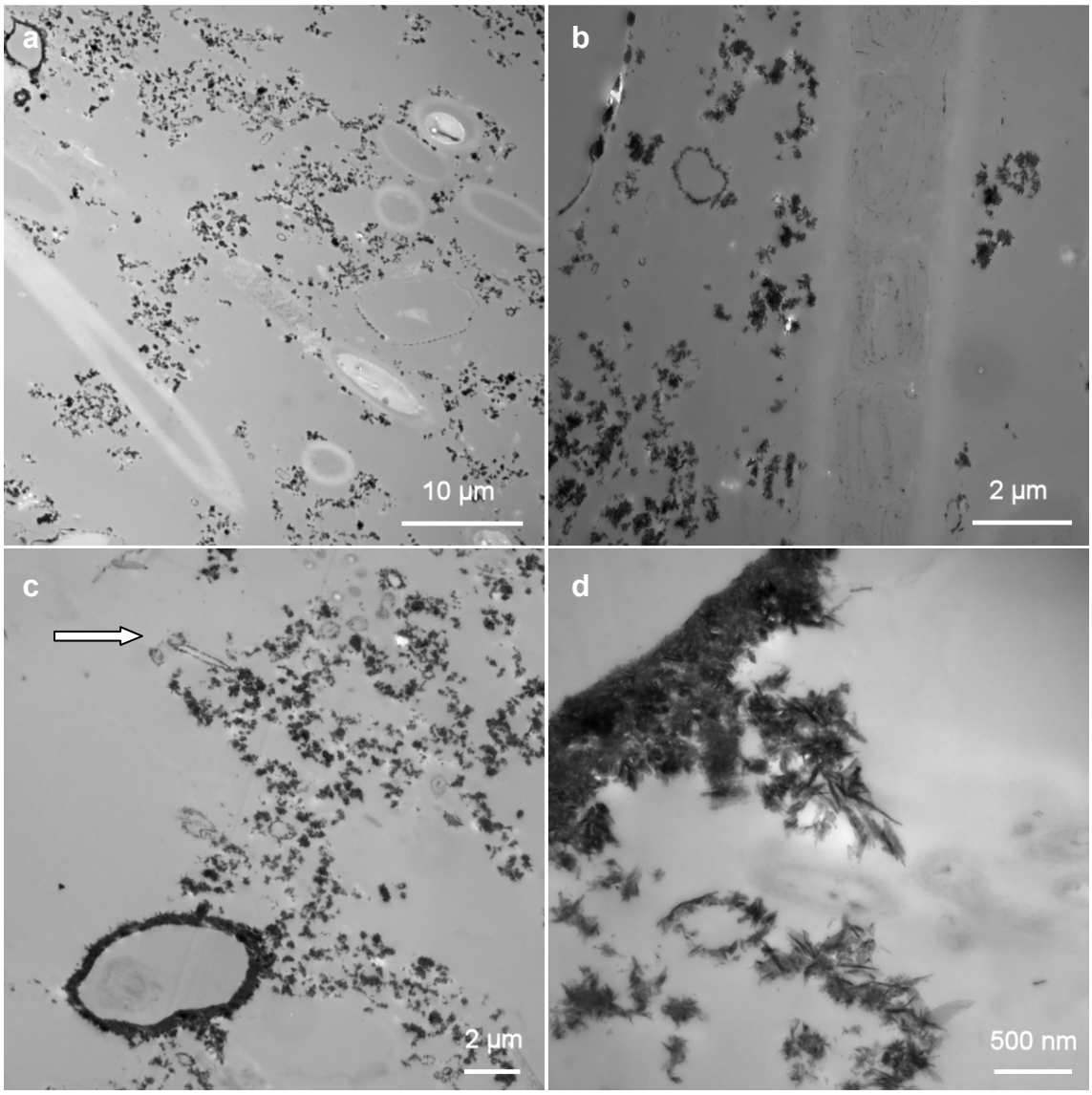

Figure 3.16 a) TEM photomicrograph of an unstained embedded mat showing attachment of iron colloids to the outside of sheaths. **b)** Intracellular precipitates of iron on the cyanobacterial thylakoid membrane. **c)** Heterotrophs (example at arrow) outlined with fine grained iron and a large organic feature (6 µm long) with a thick accumulation of iron. **d)** Close up of accumulated iron and iron colloids.

reacting with the free oxygen (Equation 3.2). The addition of bicarbonate to the already established cyanobacterial mat produced growth. $O_{2(g)}$ increased at a rate of 0.2%/day or 0.08 mM/day, which was the same as the maximum rate of oxygen production without iron (Chapter 2). Cyanobacterial growth was limited after week 3 by nutrient availability, most likely by phosphate. Intracellular mineralization on the cyanobacterial thylakoid membranes may have also slowed the rate of photosynthesis after the first month.

$$CO_2 + H_2O \rightarrow CH_2O + O_2 \quad (3.1)$$

$$4\,Fe^{2+} + O_2 + 10H_2O \rightarrow 4Fe(OH)_3 + 8H^+ \quad (3.2)$$

Starting from day 1, ferrous iron added to the surface water was rapidly oxidized. At a pH of > 6 , oxidation of ferrous iron occurs rapidly at a rate of up to 1.60 μM Fe^{2+}/s (Stumm and Morgan 1981; Trouwborst et al. 2007). Given that one mole of $O_{2(g)}$ is consumed for every four moles of Fe^{2+} oxidized, the addition of 0.029 mol of total Fe^{2+} over twenty-four weeks was equivalent to removing 5% $O_{2(g)}$ total or an average of 400 ppm $O_{2(g)}$ /day from the chamber headspace. The oxidation of ferrous iron also resulted in a decrease in pH after week 1. This decrease in pH would have enhanced dissolution of carbonates in the mat and silicates in the sediment, in part explaining the concurrent increase in dissolved manganese, iron and silica after week 15. The decrease in pH also increased the amount of $CO_{2(g)}$ in the headspace.

After week 3, an increase in the rate of heterotrophy relative to oxygenic photosynthesis in the mat would have also increased the amount of dissolved inorganic carbon (DIC). Aerobic heterotrophy decreases pH, while dissimilatory sulphate and iron reduction increases pH. An increase in dissimilatory Fe and Mn reduction by the *S. oneidensis* could also explain the increase in pore water dissolved iron and manganese

during the last two months of the experiment (Myers and Nealson 1988; Lovley 1991) (Equation 3.3 and 3.4). Mn would have accumulated in the surface water, as abiotic manganese oxidation is kinetically very slow (Stumm and Morgan 1981). The abundance of small, rod-shaped cells, the morphotype of *Shewanella oneidensis,* on ferric hydroxides and cyanobacteria within the mat supports this hypothesis (Figure 3.15a).

$$CH_3COO^- + 8\,Fe(OH)_3 + 15\,H^+ \rightarrow 2\,HCO_3^- + 8\,Fe^{2+} + 20\,H_2O \quad (3.3)$$

$$CH_3COO^- + 4\,MnO_2 + 3\,H_2O \rightarrow 2\,HCO_3^- + 4\,Mn^{2+} + 7\,OH^- \quad (3.4)$$

Using whole mount SEM, a diverse range of bacterial morphotypes of (presumably) aerobic heterotrophs, including *S. oneidensis* were common at the surface of the mat in. However at depth, only *Shewanella oneidensis* was abundant, suggesting dissimilatory iron reduction was the dominate metabolic process in the lower levels of the mat. Cocoid and vibroid shaped bacteria that likely reflected the inoculated methanogens and SRB respectively, were only observed attached to sand grains below the mat. The presence of a sulphide spot at the centre of the chamber, observed as black sediment, also showed SRB were active, although somewhat localized. Methane produced by methanogens was may have been consumed by aerobic methanotrophy (see Chapter 2). Thus, negligible change in the dissolved sulphur and the lack of accumulated methane suggests either a tight redox cycling of sulphur and methane within the mat or more likely a slow rate of sulphate reduction and methanogenesis.

As silicic acid was not added to the experiment, the low dissolved silica in the Fe-OCM and Fe-BASE experiment (< 0.09 mM) reflects the slow rate of olivine dissolution rather than the silica concentration of the ocean on early Earth. Archean ocean dissolved silica values are hypothesized to be much greater than modern (< 0.10 mM), likely at

saturation with cristobalite (0.67 mM) or amorphous silica (2.20 mM), which can affect the adsorption-desorption properties of ferric hydroxides (Konhauser et al. 2007).

Iron cycling within the mat

Intuitively, the lower portion of the mat was expected to have less iron as it was developed before the start of the experiment and before the daily additions of ferrous iron. In contrast, the upper portion of the mat grew concurrently to the daily iron additions. The distribution of iron in the mat was also affected by the cycling of iron between the redox zones within the mat. In the water column and upper mat, high concentrations of oxygen produced by oxygenic photosynthesis immobilized dissolved ferrous iron as ferric hydroxide colloids. At depth in the mat, aerobic heterotrophy consuming the oxygen intuitively produced an anoxic zone. In this anoxic zone, the abundant FeRB reduced the ferric hydroxide colloids back to mobile $Fe^{2+}_{(aq)}$. Ferrous iron that diffused upward into oxic zone was immediately re-oxidized, resulting in the accumulation of ferric hydroxides at the top of the mat.

This redox cycling of iron resulted in several of the observed mat features. First, the accumulation of ferric hydroxides at the bottom of voids within the mat shows iron was diffusing upward until it reached the oxygen-rich void. Second, based on the mat colour, several surficial macroscopic mat areas had fewer ferric hydroxides. In particular, colloid settling alone cannot explain the presence of a large 'green' cyanobacterial mat covered bubble immediately in front of the injection port (Figure 3.9b). However, if iron accumulation was also dependent on remobilization by FeRB and vertical diffusion, a lower iron concentrations would occur where the mat surface was isolated from the anoxic zones. In this case, diffusion was blocked by a large oxygen-rich bubble. The

accumulation of ferric hydroxides by iron redox cycling also appears to be disturbed immediately above the sulphide spot (Figure 3.9a). SRB and dissolved sulphur are preferentially at this location in the chamber due to the method of inoculating heterotrophs before the mat formed (Chapter 2). At this location, some of the Fe^{2+} produced by FeRB reacted with the HS^- produced by the SRB and precipitated as out of solution as $FeS_{(s)}$ (black) and perhaps through diagenesis as pyrite, resulting in less Fe^{2+} diffusing up through the mat.

The redox cycling of iron also resulted in the movement iron from the surface to deeper layers of the mat. At night when oxygen release from photosynthesis ceased, the whole mat most likely became anoxic (Pierson et al. 1999) and dissimilatory iron reduction could have occurred throughout the mat. In this experiment, the FeRB would have not necessary had to move to follow the diurnal movement of the oxic-anoxic boundary, as *S. oneidensis* are facultative anaerobes. During the day, cyanobacteria at depths of 0.5 to 1 mm in a mat could have produced enough oxygen to oxidize all the Fe^{2+} to ferric hydroxides, even at very low light intensities (Trouwborst et al. 2007).

The diurnal movement of the anoxic-oxic boundary and associated anaerobic heterotrophs within microbial mats possessing photosynthesis is almost ubiquitous (Stal 2000). In most modern marine microbial mats, the geochemistry is dominated by sulphur redox cycling, as modern seawater contains high sulphate (28 mM) but is limited in iron (Stal 2000). In the Archean, the oceanic sulphate concentration was low (< 200 μM) (Habicht et al. 2002) but the dissolved iron concentration was high (Holland 1984). The Fe-OCM experiment shows that redox cycle of iron within a photosynthesizing microbial

mat is complex. As such, prescribing a single metabolic process to Archean biogenic iron minerals from benthic mats should be done cautiously.

Secondary minerals

The presence of iron minerals with different morphologies than the ferric hydroxide colloids, including the botryoidal iron nodules (Figure 3.11d) and dense blocky iron precipitates (Figure 3.12) shows secondary iron minerals were being formed at depth in the mat. As both FeRB and oxygen from cyanobacteria were present down to the sand surface, secondary minerals may be composed of either ferric or ferrous iron, such as goethite, lipidocrocite, magnetite, siderite or green rust (Pallud et al. 2010).

Both magnetite and siderite precipitation can be induced by FeRB (Lovley 1991; Roden and Lovley 1993). Biogenic magnetite produced in laboratory experiments is usually < 50 nm, most of which is too small to be magnetic (Moskowitz et al. 1989). Magnetite produced by FeRB can also precipitate as < 1 nm coating on the ferric hydroxides particle (Hansel et al. 2004). From a hot spring, Wade et al. (1999) detected siderite below 1 mm in a cyanobacterial mat heavily mineralized with ferrihydrite, goethite, hematite and nontronite. FeRB can induce siderite precipitation by increasing the DIC and Fe^{2+} (Mortimer et al. 1997; Pierson and Parenteau 2000). In laboratory experiments, biogenic siderite forms subhedral to euhedral rhombic crystals (5-15 μm) (Mortimer et al. 1997). Siderite precipitation may also be enhanced due to an increase in pH from anoxygenic or oxygenic photosynthesis (Pierson and Parenteau 2000).

Like iron, manganese is commonly found in two oxidation states, Mn^{2+}, which is highly soluble, and Mn^{4+}, which is insoluble (Stumm and Morgan 1981). However, unlike iron, Mn^{2+} oxidation without a biological catalyst is kinetically very slow at

circumneutral pH (Stumm and Morgan 1981). In modern marine systems, manganese and iron often slowly co-precipitate as a ferromanganese oxide (Crerar and Barnes 1974). Most FeRB can also perform dissimilatory manganese reduction, which provides more energy per mol of C than iron reduction (Lovley 1991). In anoxic waters with high alkalinity, Mn^{2+} and Fe^{2+} behave similarly, as siderite and rhodochrosite ($MnCO_3$) have similar solubility product constants. In one study, siderite produced by FeRB had up to 40 wt% MnO (Mortimer et al. 1997). In Archean IFs, iron-rich carbonates have a greater concentration of manganese than oxides (Morris 1993), but in general, manganese concentrations are very low (< 1 wt% MnO) (Davy 1983).

In theoretical models for the precipitation of ferrous minerals by FeRB, the amount of iron reduction is controlled by the amount of organic matter in the sediment (Fischer and Knoll 2009). Layers with a more ferrous iron, such as siderite bands, were originally deposited with a higher organic carbon content, and thus, more dissimilatory iron reduction occurred (Fischer and Knoll 2009). In contrast, hematite layers are the result of a limited sedimentary organic carbon content, and thus limited dissimilatory iron reduction during diagenesis (Fischer and Knoll 2009). To produce magnetite, methanogenesis has been proposed as one method of removing organic carbon from the sediment to prevent the complete reduction of ferric hydroxides (Konhauser et al. 2005). The amount of carbon in the sediment may be also limited when ocean currents move C and Fe into different reservoirs (Fischer and Knoll 2009). In the OCM-experiment, both the production of secondary ferrous minerals and methanogenesis was limited by oxygen rather than organic carbon. As the OCM-experiment shows only the earliest stages cyanobacterial mat growth and secondary mineral precipitation, it does not conflict with

the above model. At 2 cm into a well-established iron mineralized cyanobacterial mat, Parenteau and Cady (2010) found the organic carbon content was low (0.2 wt%) and within the range of reported organic carbon contents from IFs (0.041- 0.203 wt%).

Iron nodules

Iron nodules are the most common secondary mineral in the cyanobacterial mat. The hollow structure of the nodules suggests precipitated iron has templated on organics. However, the diameter of the hollow centers (3-5 μm) are larger than the cell diameter of either the filamentous cyanobacteria (2-3 μm) or heterotrophs (< 1 μm) inoculated into the chamber. It is possible that iron preferentially accumulated on a large unknown organism in the mat. But the large range in size of the nodules and semi-spherical shape suggests nodules formed on degraded organics, possibly including partially degraded single cyanobacterial cells or perhaps on a microcolony of smaller heterotrophs. The relationship between the nodules and FeRB, as well as, the mechanism for the accumulation of Mn in some of these nodules is unknown. These nodules are not microfossils, as they do not preserve the shape of the cell (Southam and Donald 1999) but they are biogenic features. Iron granules of a similar size were also observed using light microscopy on an naturally iron mineralized *Oscillatoria* mat (Pierson and Parenteau 2000), but electron microscopy on an embedded piece of mat would be required to determine if these granules are also hollow.

If the iron nodules observed in the Fe-OCM experiment existed in an Precambrian IFs, it would be very difficult to distinguished them from the abiotically produced micro-nodules, which ranged in size from 0.1 to 10 μm (*e.g.*, Ayres 1972; Ahn and Buseck 1990; Morris 1993). Granules with hollow centers can be formed by iron dehydration

and templating on colloidal silica (Ahn and Buseck 1990) or by the wave and tidal action that produced the larger granules and oolites found in granular iron formations (Gross 1972).

Iron microfossils

As noted by Klein (2005), no microfossils are reported from iron-rich layers of IFs; all microfossils associated with IFs occur in the silica or carbonate bands. The most famous example of preserved microfossils is from the 1.88 Ga Gunflint IF. Within the Gunflint chert, cells fossilized in silica are strikingly outlined by dark organics and less commonly pyrite and carbonate (Barghoorn and Tyler 1965). Barghoorn and Tyler (1965) also reported that some of the filamentous microfossils were completely composed of < 1 μm grains of hematite and had suggested that the hematite had replaced the organic matter. Under TEM, goethite and elongate 50-100 nm hematite crystals were observed on the outside of some cell walls from the Gunflint IF (Tazaki et al. 1992).

While not all microfossils are outlined in small amounts of iron, they have been found in many of Paleoproterozoic Gunflint-type fossiliferous cherts. In the silica oncolites of a granular iron formation from the 1.85 Ga Frere Formation, Australia, microfossils are described as segmented rods, tubes, hollow spheres or ellipsoids of iron oxides (Walter et al. 1976). Gunflint-type microfossils occurring as hematite outlines or 'complete replacements' have been reported from the 1.9 Biwabik IF, near the Gunflint chert (Cloud and Licari 1968), the 1.88 Ga Sokoman IF, Canada (Knoll and Simonson 1981) and the 1.8 Ga Chuanlinggou IF, China (Dai et al. 2004). Hematite outlined microfossils also occur within ferriginous carbonate units associated with IFs and have been observed in the 1.89 Ga Odjick and Rocknest formations, Canada (Hofmann and

Grotzinger 1985) and in the 2.5 Ga transition from the Campbellrand carbonate platform to Kuruman IF, South Africa (Klein et al. 1987). While not associated with an iron formation, the controversial 3.5 Ga Apex Chert microfossils are also reported to be outlined in iron oxides (Schopf 1993). Some researchers have re-interpreted this feature to be a pseudo-fossil produced by a hydrothermal quartz and hematite vein (Marshall et al. 2011).

The Fe-OCM experiment contained low concentrations of silica, and therefore, cannot be used to explain the fossilization of cells by silica. However, even though the matrix material between the embedded Fe-OCM sample (plastic) and Precambrian Gunflint-biota (chert) (Figure 3.17) is very different, the pattern of iron deposition onto the cell wall is remarkably similar. Rather than replacing the organic matter during diagenesis, the Fe-OCM experiment suggests cells may have been coated with ferric hydroxides when they were living. Ferris et al. (1988) hypothesized that iron coated cells may be preferentially preserved as silica microfossils, as iron loading on the cell wall prevents enzymatic autolysis after death. The Fe-OCM experiment also shows that cyanobacteria actively try to prevent complete fossilization by ferric hydroxides by producing a thick organic sheath. If the sheath becomes too encrusted with iron, the cyanobacteria will leave the sheath behind. In SEM photomicrographs of embedded mat, up to a fourth of the iron outlined filaments no longer contain cells. Because mineralization can occur on either the cell wall or the sheath, one species of cyanobacteria can produced two different morphological types of microfossils, one with septate and one without (*e.g.*, parallel filaments in Figure 3.13). The production of a

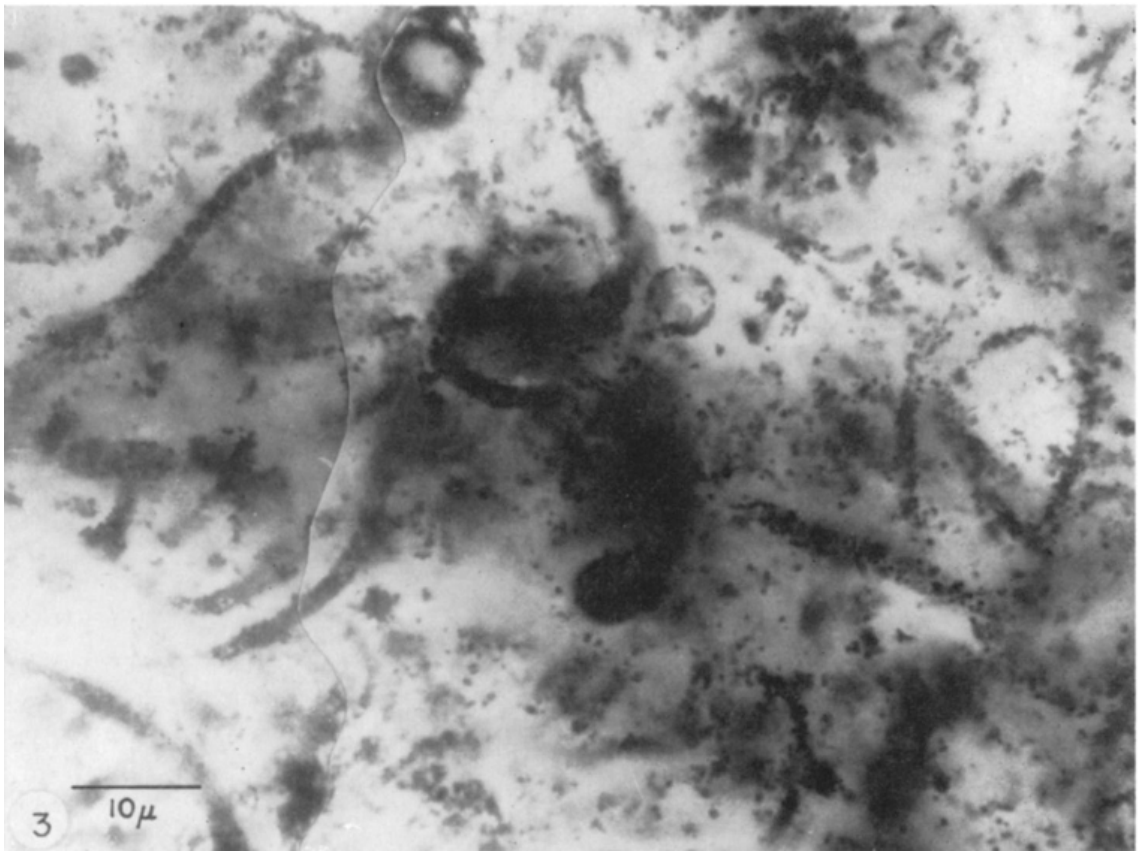

Figure 3.17 From Cloud and Licari (1968) "*Gunflintia* filaments and *Huroniospora* spheroids replaced by hematite are abundant in some of the dark laminations in the stromatolitic rocks at the Corsica mine (Biwabik Iron Formation)"

sheath by cyanobacteria to escape mineralization by silica colloids has also been described from a modern hot spring (Phoenix et al. 2000).

Mineralization on cell surfaces occurs when either passive adsorption on deprotonated organics or the metabolic processes of the cell creates a highly supersaturated environment adjacent to the cell. Deprotonation of the cell wall after cell death may augment mineralization by binding more metals (Southam and Donald 1999). In the Fe-OCM experiment, enhanced fossilization of cell walls occurred at depth in the mat and was associated with secondary mineral precipitation. This suggests FeRB have a role in both the re-mobilizing of iron and fossilization. In other areas of the mat, continued dissimilatory iron reduction could remove all iron from the cell surface (Figure 3.15a), perhaps resulting in pure chert microfossils being preserved in the geologic record (Edwards et al. 2012).

The FE-OCM, with 2.4 mg of Fe/cm^2 may represent some intermediate in iron concentration between fossiliferous IF cherts (85-95 % SiO_2), which only contain a small amounts of siderite and hematite (Marin et al. 2010), and the average iron-rich microbands in IFs, which contain 22.5 mg of Fe/cm^2 (Trendall and Blockley 1970). Klein (2005) hypothesized that microfossils do not occur in iron formations because ferric minerals are not the result of direct microbial activity. Alternatively, fossils may not be present in the iron-rich layers because later stages of diagenesis, compaction and metamorphism destroy the biogenic features. After deposition, the ferric hydroxides and silica gel in IFs underwent dewatering and compaction of up to 95% (Trendall and Blockley 1970; Gross 1972). By definition, all minerals in IFs are secondary as the ferric hydroxides were re-ordered into hematite and the silica gel crystallized into chert (Klein

2005). Most IFs have also undergone low grade metamorphism resulting in secondary minerals, such as minnesotaite, greenalite, stilpnomelane and riebeckite (Klein 2005). In iron formations affected hydrothermal alternation, the hematite is upgraded resulting in large prismatic or platy crystals (Bekker et al. 2010). Any of these processes could have disturbed the < 100 nm iron crystals that outline the microfossils. The smallest microfossils, such as those of the FeRB, would be particularly susceptible to damage. However, this study shows that both cyanobacteria and FeRB have the potential to be fossilized by iron during the earliest stages of diagenesis.

3.5 Conclusion

The metabolic processes of cyanobacteria and FeRB resulted in active redox cycling of iron within the microbial mat. This redox cycling produced macro- and microscopic features, which have potential to be used as biosignatures in Archean and Paleoproterozoic iron formations. Features included the accumulation of ferric hydroxide colloids at the bottom of oxygen-rich voids and fewer ferric hydroxides where iron sulphides were present. Biogenic secondary mineral precipitates included iron-rich hollow nodules and iron-rich microfossils. Microfossils in the Fe-OCM experiment are similar to microfossils outlined in iron from Paleoproterozoic Gunflint-type cherts.

3.6 References

Ahn, J. and Buseck, P. 1990. Hematite nanospheres of possible colloidal origin from a Precambrian banded iron formation. Science, **250**: 111-113.

Ayres, D.E. 1972. Genesis of iron-bearing minerals in banded iron formation mesobands in the Dales Gorge Member, Hamersley Group, Western Australia. Economic Geology, **67**: 1214-1233.

Barghoorn, E.S. and Tyler, S.A. 1965. Microorganisms from the Gunflint Chert. Science, **147**: pp. 563-577.

Bekker, A., Slack, J.F., Planavsky, N., Krapez, B., Hofmann, A., Konhauser, K.O., and Rouxel, O.J. 2010. Iron formation; the sedimentary product of a complex interplay among mantle, tectonic, oceanic, and biospheric processes. Economic Geology and the Bulletin of the Society of Economic Geologists, **105**: 467-508.

Canfield, D. 2005. The early history of atmospheric oxygen: Homage to Robert A. Garrels. Annual Review of Earth and Planetary Sciences, **33**: 1-36.

Canfield, D. 1998. A new model for Proterozoic ocean chemistry. Nature, **396**: 450-453.

Cloud, P. 1973. Paleoecological significance of banded iron-formation. Economic Geology, **68**: 1135-1143.

Cloud, P. and Licari, G. 1968. Microbiotas of banded iron formations. Proceedings of the National Academy of Sciences, **61**: 779-786.

Crerar, D.A. and Barnes, H.L. 1974. Deposition of deep-sea manganese nodules. Geochimica et Cosmochimica Acta, **38**: 279-300.

Dai, Y., Song, H., and Shen, J. 2004. Fossil bacteria in Xuanlong iron ore deposits of Hebei Province. Science in China Series D-Earth Sciences, **47**: 347-356.

Davy, R. 1983. A contribution on the chemical composition of Precambrian iron-formations *In* Iron-formation: facts and problems *Edited by* A.F. Trendall and R.C. Morris. Elsevier, Amsterdam, pp. 325-344.

Edwards, C.T., Pufahl, P.K., Hiatt, E.E., and Kyser, T.K. 2012. Paleoenvironmental and taphonomic controls on the occurrence of paleoproterozoic microbial communities in the 1.88 Ga Ferriman Group, Labrador Trough, Canada. Precambrian Research, **212–213**: 91-106.

Ferris, F., Fyfe, W., and Beveridge, T. 1988. Metallic ion binding by *Bacillus subtilis* - implications for the fossilization of microorganisms. Geology, **16**: 149-152.

Fischer, W.W. and Knoll, A.H. 2009. An iron shuttle for deepwater silica in late Archean and early Paleoproterozoic iron formation. Geological Society of America Bulletin, **121**: 222-235.

Foster, I.S., King, P.L., Hyde, B.C., and Southam, G. 2010. Characterization of halophiles in natural MgSO(4) salts and laboratory enrichment samples: Astrobiological implications for Mars. Planetary and Space Science, **58**: 599-615.

Gross, G. 1972. Primary features in cherty iron-formations. Sedimentary Geology, **7**: 241-&.

Habicht, K., Gade, M., Thamdrup, B., Berg, P., and Canfield, D. 2002. Calibration of sulfate levels in the archean ocean. Science, **298**: 2372-2374.

Hansel, C., Benner, S., Nico, P., and Fendorf, S. 2004. Structural constraints of ferric (hydr)oxides on dissimilatory iron reduction and the fate of Fe(II). Geochimica et Cosmochimica Acta, **68**: 3217-3229.

Hofmann, H.J. and Grotzinger, J.P. 1985. Shelf-facies microbiotas from the Odjick and Rocknest Formations (Epworth Group; 1.89 Ga), Northwestern Canada. Canadian Journal of Earth Sciences, **22**: 1781-1792.

Holland, H.D. 1984. The chemical evolution of the atmosphere and oceans. Princeton University Press, Princeton, 582 p.

Johnson, C.M., Beard, B.L., Klein, C., Beukes, N.J., and Roden, E.E. 2008. Iron isotopes constrain biologic and abiologic processes in banded iron formation genesis. Geochimica et Cosmochimica Acta, **72**: 151-169.

Kappler, A., Pasquero, C., Konhauser, K.O., and Newman, D.K. 2005. Deposition of banded iron formations by anoxygenic phototrophic Fe(II)-oxidizing bacteria. Geology, **33**: 865-868.

Klein, C. and Beukes, N.J. 1992. Time distribution, stratigraphy, and sedimentologic setting and geochemistry of Precambrian iron-formations. *In* The Proterozoic biosphere *Edited by* J.W. Schopf and C. Klein. Cambridge University Press, Cambridge, pp. 139-146.

Klein, C. 2005. Some Precambrian banded iron-formations (BIFs) from around the world: Their age, geologic setting, mineralogy, metamorphism, geochemistry, and origin. American Mineralogist, **90**: 1473-1499.

Klein, C., Beukes, N., and Schopf, J. 1987. Filamentous microfossils in the early Proterozoic Transvaal Supergroup - their morphology, significance, and paleoenvironmental setting. Precambrian Research, **36**: 81-94.

Knoll, A.H. and Simonson, B. 1981. Early Proterozoic microfossils and penecontemporaneous quartz cementation in the Sokoman Iron Formation, Canada. Science, **211**: 478-480.

Konhauser, K.O., Newman, D.K., and Kappler, A. 2005. The potential significance of microbial Fe(III) reduction during deposition of Precambrian banded iron formations. Geobiology, **3**: 167-177.

Konhauser, K. and Ferris, F. 1996. Diversity of iron and silica precipitation by microbial mats hydrothermal waters, Iceland: Implications for Precambrian iron formations. Geology, **24**: 323-326.

Konhauser, K., Hamade, T., Raiswell, R., Morris, R., Ferris, F., Southam, G., and Canfield, D. 2002. Could bacteria have formed the Precambrian banded iron formations? Geology, **30**: 1079-1082.

Konhauser, K.O., Amskold, L., Lalonde, S.V., Posth, N.R., Kappler, A., and Anbar, A. 2007. Decoupling photochemical Fe(II) oxidation from shallow-water BIF deposition. Earth and Planetary Science Letters, **258**: 87-100.

Kump, L.R. and Seyfried, W.E., Jr. 2005. Hydrothermal Fe fluxes during the Precambrian; effect of low oceanic sulfate concentrations and low hydrostatic pressure on the composition of black smokers. Earth and Planetary Science Letters, **235**: 654-662.

Lovley, D.R. 1991. Dissimilatory Fe(III) and Mn(IV) reduction. Microbiological reviews, **55**: 259-287.

Marin, J., Chaussidon, M., and Robert, F. 2010. Microscale oxygen isotope variations in 1.9 Ga Gunflint Cherts: Assessments of diagenesis effects and implications for oceanic paleotemperature reconstructions. Geochimica et Cosmochimica Acta, **74**: 116-130.

Marshall, C.P., Emry, J.R., and Marshall, A.O. 2011. Haematite pseudomicrofossils present in the 3.5-billion-year-old Apex Chert. Nature Geoscience, **4**: 240-243.

Morris, R.C. 1993. Genetic modelling for banded iron-formation of the Hamersley Group, Pilbara Craton, Western Australia. Precambrian Research, **60**: 243-286.

Mortimer, R., Coleman, M., and Rae, J. 1997. Effect of bacteria on the elemental composition of early diagenetic siderite: Implications for palaeoenvironmental interpretations. Sedimentology, **44**: 759-765.

Moskowitz, B., Frankel, R., Bazylinski, D., Jannasch, H., and Lovley, D. 1989. A comparison of magnetite particles produced anaerobically by magnetotactic and dissimilatory iron-reducing bacteria. Geophysical Research Letters, **16**: 665-668.

Myers, C. and Nealson, K. 1988. Bacterial manganese reduction and growth with manganese oxide as the sole electron-acceptor. Science, **240**: 1319-1321.

Nealson, K. and Myers, C. 1990. Iron reduction by bacteria - a potential role in the genesis of banded iron formations. American Journal of Science, **290A**: 35-45.

Parenteau, M.N. and Cady, S.L. 2010. Microbial biosignatures in iron-mineralized phototrophic mats at Chocolate Pots Hot Springs, Yellowstone National Park, United States. Palaios, **25**: 97-111.

Pecoits, E., Gingras, M.K., Barley, M.E., Kappler, A., Posth, N.R., and Konhauser, K.O. 2009. Petrography and geochemistry of the Dales Gorge banded iron formation; paragenetic sequence, source and implications for palaeo-ocean chemistry. Precambrian Research, **172**: 163-187.

Phoenix, V., Adams, D., and Konhauser, K. 2000. Cyanobacterial viability during hydrothermal biomineralisation. Chemical Geology, **169**: 329-338.

Pierson, B. and Parenteau, M. 2000. Phototrophs in high iron microbial mats: Microstructure of mats in iron-depositing hot springs. FEMS Microbiology Ecology, **32**: 181-196.

Pierson, B., Parenteau, M., and Griffin, B. 1999. Phototrophs in high-iron-concentration microbial mats: Physiological ecology of phototrophs in an iron-depositing hot spring. Applied and Environmental Microbiology, **65**: 5474-5483.

Posth, N.R., Hegler, F., Konhauser, K.O., and Kappler, A. 2008. Alternating Si and Fe deposition caused by temperature fluctuations in Precambrian oceans. Nature Geoscience, **1**: 703-708.

Raiswell, R. and Canfield, D.E. 2012. The iron biogeochemical cycle past and present. Geochemical Perspectives, **1:** 1-232.

Roden, E. and Lovley, D. 1993. Dissimilatory Fe(III) reduction by the marine microorganism *Desulfuromonas acetoxidans*. Applied and Environmental Microbiology, **59**: 734-742.

Schopf, J.W. 1993. Microfossils of the early Archean Apex Chert - new evidence of the antiquity of life. Science, **260**: 640-646.

Southam, G. and Donald, R. 1999. A structural comparison of bacterial microfossils vs. 'nanobacteria' and nanofossils. Earth Science Reviews, **48**: 251-264.

Stal, L.J. 2000. Cyanobacterial mats and stromatolites. *In* The Ecology of Cyanobacteria *Edited by* B.A. Whitton and M. Potts. Kluwer Academic, the Netherlands, pp. 61-120.

Stumm, W. and Morgan, J.J. 1981. Aquatic chemistry : An introduction emphasizing chemical equilibria in natural waters. Wiley, New York.

Tazaki, K., Ferris, F., Wiese, R., and Fyfe, W. 1992. Iron and graphite associated with fossil bacteria in chert. Chemical Geology, **95**: 313-325.

Trendall, A.F. 2002. The significance of iron-formation in the Precambrian stratigraphic record. *In* Precambrian sedimentary environments: A modern approach to ancient depositional systems *Edited by* W. Altermann and P.L. Corcoran. Blackwell Science, Oxford, pp. 33-66.

Trendall, A.F. and Blockley, J.G. 1970. The iron formations of the Precambrian Hamersley Group, Western Australia, with special reference to the associated crocidolite. Geologic Survey of Western Australia.

Trouwborst, R.E., Johnston, A., Koch, G., Luther, G.W., III, and Pierson, B.K. 2007. Biogeochemistry of Fe(II) oxidation in a photosynthetic microbial mat: implications for Precambrian Fe(II) oxidation. Geochimica et Cosmochimica Acta, **71**: 4629-4643.

Wade, M., Agresti, D., Wdowiak, T., Armendarez, L., and Farmer, J. 1999. A Mossbauer investigation of iron-rich terrestrial hydrothermal vent systems: Lessons for Mars exploration. Journal of Geophysical Research, **104**: 8489-8507.

Walker, J.C.G. 1984. Suboxic diagenesis in banded iron formations. Nature, **309**: 340-342.

Walter, M.R., Bauld, J., and Brock, T.D. 1972. Siliceous algal and bacterial stromatolites in hot spring and geyser effluents of Yellowstone National Park. Science, **178**: 402-405.

Walter, M., Goode, A., and Hall, W. 1976. Microfossils from a newly discovered Precambrian stromatolitic iron formation in Western Australia. Nature, **261**: 221-223.

Chapter 4 Synthesis

4.1 Archean oxygen oases

In the current accepted model for the oxygenation of Earth's surface, cyanobacterial mats on continental shelves produced highly localized oxygen-rich environments between 2.8-2.5 Ga (Kasting 1993; Holland 2006). These oxygen oases then expanded to oxygenate the atmosphere and ocean surface between 2.45-2.32 Ga (Farquhar et al. 2011). The high iron (the Fe-OCM chamber in Chapter 3) and low iron (the OCM chamber in Chapter 2) experiments in this thesis are modelling two different locations on the continental shelf during the late Archean. The Fe-OCM chamber may represent an environment close to the chemocline, where anoxic ferruginous deep water would have mixed with oxic surface water. The Fe-OCM chamber may also represent an anoxic continental shelf environment that has been newly colonized by a cyanobacterial mat. The OCM experiment may represent a shelf environment closer to shore, perhaps in a stromatolitic reef. In this environment, most of the dissolved iron would have already been removed and aerobic heterotrophy and methanotrophy would have been the primary local oxygen sinks. This model is consistent with the geologic record as many iron formations were deposited in deeper water, whereas, limestone and dolostone units were deposited in a shallow water setting (Trendall 2002). In addition, granular iron formations were deposited in a shallow water, higher energy environment (Trendall 2002).

Between the distal shelf, with a high iron input, and the near shore, with a low iron input, the amount of iron oxidation may have created other geochemical gradients. Areas with high iron oxidation rates may have had a lower pH (Fe-OCM = pH 6.1) than

areas with low iron concentrations (OCM = pH 9.5). In addition, the different heterotrophic communities within these two environments may have also changed the alkalinity, and thus, the amount of carbonate precipitation within the mat. For example aerobic respiration and fermentation results in increased carbonate dissolution, whereas methanogenesis, dissimilatory sulphate reduction and dissimilatory iron reduction (4.5 X more than sulfate reduction) promote carbonate precipitation (Visscher and Stolz 2005).

Interestingly, a high iron concentration did not affect the maximum rate of photosynthesis and both the OCM and Fe-OCM experiments accumulated oxygen at a rate of up to 0.08 mM/day. Note, in the Archean, oxygen production rates by cyanobacterial mats on the shelf floor would have been controlled by light availability, which in part is affected by the relatively faint young sun (Zahnle and Walker 1982) and by water depth. In the Archean, cyanobacterial growth was unlikely to be limited by DIC (like in the OCM experiment) but may have been limited by phosphate (like in the subsequent Fe-OCM experiment).

Oxygen did not accumulate in the atmosphere until 300 Ma after the evolution of oxygenic photosynthesis because of the presence of large oxygen sinks (Holland 2002; Catling and Claire 2005). Given that the fraction of carbon buried as organics has been constant since the early Archean, the rate of oxygen accumulation appears to be controlled by abiotic processes that release reduced chemical species into the atmosphere and oceans (Holland 2002). This thesis examined two oxygen sinks within a microbial mat, methane and dissolved ferrous iron, that may have affected the global fluxes of oxidized and reduced chemical species. The experiment in Chapter 2 determined that the rate of methanotrophy within a mat possessing oxygenic photosynthesis is much greater

than the rate of methanogenesis. This process may have helped draw down atmospheric methane in the late Archean, resulting in widespread glaciations during the Paleoproterozoic (Kasting 2005). The experiment in Chapter 3 determined that > 95% of ferrous iron add to a cyanobacterial mat is mineralized as ferric hydroxide colloids. If the water column above the mat is oxic, iron redox cycling occurs due to the metabolic processes of cyanobacteria and FeRB.

At a microscopic scale, interesting relationships between the microorganisms and iron minerals were also observed in both the OCM and Fe-OCM experiments. In the OCM experiment, the distribution and abundance of aerobic heterotrophs appeared to be controlled by iron availability (*e.g.,* Figure 2.12c versus Figure 2.15b). Further work needs to be completed to determine if low iron concentrations are limiting heterotrophic growth in modern microbial mats, particularly if there is competition between cyanobacteria and bacteria using siderophores.

Within the Fe-OCM experiment, FeRB occurred as either single cells or as large clusters, (i.e., microcolonies). While it unknown exactly why some of these areas contained abundant FeRB, the presence of FeRB removing ferric hydroxides from the cyanobacterial surface (Figure 3.15a) could have mutually beneficial to both organisms. Cyanobacteria are known to release simple sugars and organic acids that create biological 'hot spots' for heterotrophic bacteria (Worm and Søndergaard, 1998). In the Archean, attracting FeRB with simple organics to 'clean' the iron oxides off the surface of the cell wall may have been advantageous to the cyanobacteria.

4.2 Future work

Creating mid-scale laboratory models of Archean environments has several advantages over analog field sites. First, laboratory models can be more controlled and researchers can add uniquely Archean features to the system, such as high $CH_{4(g)}$, high $CO_{2(g)}$, low SO_4^{2-}, variable salinity, a 'faint young sun' or high UV light. Second, the limited diversity of organisms in the inoculated microbial mat allows for greater confidence in correlating observed bacterial morphologies with a specific metabolic process.

If the Archean atmosphere did contain high methane, as proposed by most researchers, abundant and very rapid methanotrophy could have occurred as soon as photosynthesis added oxidizing agents to the environment (O_2 or SO_4^{2-}). Given that $\delta^{13}C$ values of late Archean organics suggest one third of carbon is from methanotrophy (Hayes 1994), further experimental work should be completed to determine the limits of methanotrophy in a cyanobacterial mat with a constantly high methane concentration (*e.g.,* 1000 ppm).

Samples from the Fe-OCM experiment should be further characterized to determine the mineralogy of the precipitates. The distribution of iron in the mat showed FeRB in the anoxic zone was remobilized ferric minerals to $Fe^{2+}_{(aq)}$. Because FeRB can produce ferrous minerals, determining the oxidation state of iron in the secondary precipitates would be helpful to compare the Fe-OCM experiment to Precambrian iron formations. Samples of mat were analyzed in a Rigaku x-ray diffractometer (XRD), however, due to the fine-grained texture and amorphous nature of the iron precipitates no peaks were produced. X-ray absorption near edge structure (XANES) spectroscopy is

one method that could determine the mineralogy and redox state of iron at the micron-scale.

Given the success of the Fe-OCM experiment at modeling a Precambrian iron formation with a redox gradient produced by cyanobacteria and FeRB, other hypotheses about iron formations could be experimentally tested. If a similar process to continuous upward iron mobility in the Fe-OCM experiment occurred in a Precambrian iron deposit, the iron accumulation may also be dependent of the presence of silica layers to trap the iron. In contrast, Fischer and Knoll (2009) have proposed that the redox cycling of iron sequestered silica from the water column into the sediment. In their model, dissolved silica in seawater adsorbed to freshly precipitated ferric hydroxide colloids, which sunk to the ocean floor. Once in the sediment, dissimilatory iron reduction or reordering of the ferric hydroxides crystals resulted in silica desorption and the concentration of silica-rich layers in the pore water. An experiment similar to the Fe-OCM may be able to test hypotheses about the interactions between iron and silica as iron is biologically oxidized and reduced. For example, Konhauser et al. (2005) proposed that the adsorption of silica to ferric hydroxides may hinder FeRB activity.

4.3 References

Catling, D. and Claire, M. 2005. How Earth's atmosphere evolved to an oxic state: A status report. Earth and Planetary Science Letters, **237**: 1-20.

Farquhar, J., Zerkle, A.L., and Bekker, A. 2011. Geological constraints on the origin of oxygenic photosynthesis. Photosynthesis Research, **107**: 11-36.

Fischer, W.W. and Knoll, A.H. 2009. An iron shuttle for deepwater silica in late Archean and early Paleoproterozoic iron formation. Geological Society of America Bulletin, **121**: 222-235.

Hayes, J. 1994. Global methanotrophy at the Archean-Proterozoic transition. *In* Early life on Earth: Nobel Symposium No. 84 *Edited by* S. Bengtson. Columbia University Press, New York, pp. 220-236.

Holland, H. 2002. Volcanic gases, black smokers, and the Great Oxidation Event. Geochimica et Cosmochimica Acta, **66**: 3811-3826.

Holland, H.D. 2006. The oxygenation of the atmosphere and oceans. Philosophical Transactions: Biological Sciences, **361**: 903-915.

Kasting, J.F. 1993. Earth's early atmosphere. Science, **259**: 920-926.

Kasting, J. 2005. Methane and climate during the Precambrian era. Precambrian Research, **137**: 119-129.

Konhauser, K.O., Newman, D.K., and Kappler, A. 2005. The potential significance of microbial Fe(III) reduction during deposition of Precambrian banded iron formations. Geobiology, **3**: 167-177.

Trendall, A.F. 2002. The significance of iron-formation in the Precambrian stratigraphic record. *In* Precambrian sedimentary environments: A modern approach to ancient depositional systems *Edited by* W. Altermann and P.L. Corcoran. Blackwell Science, Oxford, pp. 33-66.

Visscher, P. and Stolz, J. 2005. Microbial mats as bioreactors: Populations, processes, and products. Palaeogeography Palaeoclimatology Palaeoecology, **219**: 87-100.

Worm, J. and Morten Søndergaard. 1998. Dynamics of heterotrophic bacteria attached to *Microcystis spp.* (cyanobacteria). Aquatic Microbial Ecology, **14**: 19-28.

Zahnle, K.J. and Walker, J.C.G. 1982. The evolution of solar ultraviolet luminosity. Reviews of Geophysics, **20**: 280-292.

Appendices

Appendix A Properties of forsterite sand

A-1 X-ray fluorescence (XRF) of forsterite sand

Trace Element Analysis by pressed pellet XRF

Element	Concentration (ppm)
Nb	8
Zr	22
Y	7
Sr	3
Rb	< 2
Th	< 5
U	< 5
Pb	< 5
Ga	< 2
As	< 2
Zn	45
Cu	11
Ni	2663
Co	124
Mn	995
Cr	2350
V	10
Ba	857

A-2 Physical and chemical properties of forsterite sand

from the OLIVINE 100 Optamineral Inc. technical data sheet

Typical Chemical Analysis (%):

Magnesium Oxide	MgO	~ 48.0
Silicon Dioxide	SiO_2	~ 43.0
Iron Oxide	Fe_2O_3	~ 7.0
Aluminum Oxide	Al_2O_3	~ 0.5
Nickel	Ni	~ 0.4
Calcium Oxide	CaO	~ 0.1
Manganese Oxide	MnO	~ 0.1

Typical Physical Properties:

Colour…….. Green to grey/green **Grain Shape……**Angular
Mineral……. Olivine **Bulk Density……..**115 lbs./ft.^{3}
Moisture……..< 0.20%
Solubility……. Insoluble **Melting Point (^{o}F)……**~2800 - 3200
Specific Gravity (g/cc)…..…3.3 **Melting Point (^{o}C)……**~1538 – 1760

Typical Gradation:

US		**Per Cent**	
Mesh	**Microns**	**Retained**	**Passing**
20	850	0.0	100.0
30	600	0.0	100.0
40	425	0.4	99.6
50	300	1.5	98.1
70	212	9.0	89.1
100	150	32.5	56.6
140	106	33.0	23.6
200	75	15.6	8.0
270	53	5.4	2.6
PAN	0	2.6	0.0
		Grain Fineness #:	***101.4***

Appendix B Chemical compositions of solutions and media

B-1 Artificial Seawater

Chemical	g/L solution
NaCl	21.195
KCl	0.6
$NaHCO_3$	0.175
KBr	0.085
H_3BO_3	0.025
NaF	0.0027
$MgCl_2 \cdot 6H_2O$	9.59
$CaCl_2$	1.0153
$SrCl_2 \cdot 6H_2O$	0.0214
$C_6H_8O_6$	0.1-0.2

(modified to exclude sulphate)

Harrison, P.J., Waters, R.E., and Taylor, F.J.R. 1980. A broad spectrum artificial sea water medium for coastal and open ocean phytoplankton. Journal of Phycology, **16**: 28-35.

B-2 BG-11 Cyanobacterial Media

Chemical	g/L solution
Disodium EDTA	0.001
Citric acid	0.006
$NaNO_3$	1.5
$K_2HPO_4 \cdot 3H_2O$	0.04
$MgSO_4 \cdot 7H_2O$	0.075
$CaCl_2 \cdot 2H_2O$	0.036
$Na_2CO_3(H_2O)$	0.02
Ferric ammonium citrate	0.006
SL-8 micronutrient solution	1ml
DN-vitamin mix	1ml

Rippka, R., Deruelles, J., Waterbury, J.B., Herdman, M. and Stanier, R.Y. 1979.Generic assignments, strain histories and properties of pure cultures of cyanobacteria. Journal of General Microbiology, **111**: 1-61.

B-3 Postgate SRB Media

Chemical	g/L of solution
Tryptone	10
MgSO4·7H2O	2
60% Sodium Lactate	6
Yeast Extract	1
L-ascorbic acid	0.75
Na-thioglycollate	0.75
(modified to exclude Fe)	

Media brought to pH=7.5 with NaOH and then filter sterilized.

Postgate, J. R. 1984. The sulphate-reducing bacteria. 2nd edition. Cambridge Press.

B-4 Balch Methanogen Media

Chemical	g/L of solution
KCl	0.335
$MgCl_2$/ $MgCl_2.6H_2O$	2.75/ 5.87
$MgSO_4$	3.45
NH_4Cl	0.25
$CaCl_2$	0.07
K_2HPO_4	0.18
NaCl	18
Mineral Elixir	10 mL
Vitamin Mixture	10 mL
Sodium Acetate	1
Yeast Extract	2
Trypicase/pepticase/peptone	2
$FeSO_4$ stock	6 mL
$NiCl_2$ stock	0.1 mL
Resazurin	1 mL
1.25% cysteine-sulphide	20 mL
8% Na_2CO_3	4.8 mL

Headspace 20%CO_2:80% H_2

Mineral Elixir for Balch media

Chemical	g/L of solution
Nitrilotriacetate (nitrilotriacetic acid)	1.5
$MgSO_4.7H_2O$	3.0
$MnSO_4.H_2O$	0.5
NaCl	1.0
$CoCl_2.6H_2O$	0.1
$CaCl_2$	0.075
$ZnSO_4.7H_2O$	0.1
$CuSO_4.5H_2O$	0.01
$AlK(SO_4)_2.12H_2O$	0.01
H_3BO_3 (Boric Acid)	0.01
$Na_2MoO_4.2H_2O$	0.01

Vitamin Mixture for Balch media

Chemical	g/L of solution
Biotin (Vitamin B_7)	0.002
Folic acid	0.002
Pyrodoxine hydrochloride (Vitamin B_6)	0.01
Thiamine hydrochloride	0.005
Riboflavin	0.005
Nicotinic acid	0.005
Vitamin B_{12} (Cobalamin)	0.005
PABA (p-aminobenzoic acid)	0.005
Lipoic acid	0.005
Pantothenic acid	0.005

Balch, W.E., Fox, G.E., Magrum, L.J., Woese, C.R., and Wolfe, R.S.,. 1979. Methanogens: Reevaluation of a unique biological group. Microbiological Reviews, **43**: 260-296.

Appendix C Microbial counts

Sample	Count of green cells in square					Average count	# cell per mL	amount added (ml)	total cells in addition
	1	2	3	4	4				
FeRB_blue	11	6	9	7	6	7.8	97500000	30	~ $3x10^9$
Meth_green	8	10	12	10	15	11	137500000	30	$4.13x10^9$
Meth_orange	1	4	4	0	0	1.8	22500000	20	$4.45x10^8$
SRB_pink	8	15	21	20	12	15.2	190000000	18	$3.42x10^9$

A total cell count used the formula:

cells/mL = (average cells in 0.25 mm by 0.25 mm square) X (25 squares/1 mm by 1 mm grid) X 50 000 X dilution factor

where 50 000 calculates the volume of represented by the counting chamber grid and the dilution factor is 10.

Appendix D PHREEQC geochemical modeling

D-1 Inputs into PHREEQC modeling the surface water

Elements	OCM at T=0 (M)	OCM final (M)	BASE at T=0 (M)	BASE final (M)
B	4.04E-04	4.04E-04	4.04E-04	4.04E-04
Br	7.14E-04	7.14E-04	7.14E-04	7.14E-04
C	2.10E-03	2.10E-03	2.10E-03	1.43E-03
Ca	9.10E-03	9.10E-03	9.10E-03	9.10E-03
Cl	4.83E-01	4.83E-01	4.83E-01	4.83E-01
F	6.43E-05	6.43E-05	6.43E-05	6.43E-05
Fe	1.52E-06	0.00E+00	7.80E-07	6.12E-06
H(0)				3.60E-06
K	8.72E-03	8.72E-03	8.72E-03	8.72E-03
Mg	4.72E-02	4.72E-02	4.72E-02	4.72E-02
Na	3.65E-01	3.65E-01	3.65E-01	3.65E-01
O(0)	3.10E-06	1.25E-04	3.10E-06	3.10E-06
P	5.79E-04	0.00E+00	4.58E-04	2.04E-04
S(6)	1.96E-04	2.34E-04	7.00E-06	
Si	0.00E+00	4.62E-06	0.00E+00	4.99E-05
Sr	8.05E-05	8.05E-05	8.05E-05	8.05E-05
pH	8	9.5	8	7.9

EQUILIBRIUM_PHASES	OCM at T=0 (total mol)	OCM final (total mol)	BASE at T=0 (total mol)	BASE final (total mol)
$CH_{4(g)}$	0.00124	0.00000157	0	0
$CO_{2(g)}$	0.00019	0.0000087	0.000107	0.000159
Fayalite	0.108	0.108	0.108	0.108
Magnetite	0.069	0.069	0.069	0.069
$O_{2(g)}$	0.0008	0.02004	0.000174	0.00195
Pyrite	0.066	0.066	0.066	0.066
$H_{2(g)}$	0	0	0	0.0007277

SOLID_SOLUTIONS	(total moles)			
Olivine				
Fayalite	5.09	5.09	5.09	5.09
Forsterite	45.85	45.85	45.85	45.85

D-2 PHREEQC saturation indices (SI) of surface water

Phase	Chemical Formula	OCM at T=0	OCM final	BASE at T=0	BASE final
Anhydrite	CaSO4	-2.98	-2.91	-4.43	-2.97
Aragonite	CaCO3	0.4	1.44	0.4	0.13
Brucite	Mg(OH)2	-2.17	0.83	-2.16	-2.36
Calcite	CaCO3	0.54	1.58	0.54	0.28
Celestite	SrSO4	-2.77	-2.69	-4.22	-2.75
CH4(g)	CH4	-73.35	-87.31	-73.35	-72.62
Chalcedony	SiO2		-1.95		-0.69
Chrysotile	Mg3Si2O5(OH)4		8.15		1.09
CO2(g)	CO2	-3.15	-5.1	-3.15	-3.21
Diopside	CaMgSi2O6		1.58		-2.28
Dolomite	CaMg(CO3)2	1.98	4.06	1.98	1.46
Fayalite	Fe2SiO4				-6.47
Fe(OH)2	Fe(OH)2	-6.18		-6.47	-5.48
Fe(OH)3(a)	Fe(OH)3	1.8		1.51	2.39
Fluorite	CaF2	-1.37	-1.37	-1.37	-1.37
Forsterite	Mg2SiO4		0.93		-4.19
Goethite	FeOOH	7.69		7.41	8.29
Gypsum	CaSO4:2H2O	-2.78	-2.7	-4.23	-2.76
H2(g)	H2	-24	-27	-24	-2.54
H2O(g)	H2O	-1.52	-1.52	-1.52	-1.52
Halite	NaCl	-2.68	-2.68	-2.68	-2.68
Hematite	Fe2O3	17.4		16.82	18.6
Hydromagnesite	Mg5(CO3)4(OH)2:4H2O	-4.02	3.14	-4.02	-5.26
Hydroxyapatite	Ca5(PO4)3OH	8.59		8.29	
Jarosite-K	KFe3(SO4)2(OH)6	-6.38		-10.14	-4.26
Magnesite	MgCO3	0.88	1.93	0.88	0.62
Magnetite	Fe3O4	10.7		9.83	12.59
Melanterite	FeSO4:7H2O	-10.82		-12.56	-9.91
O2(g)	O2	-2.86	-1.26	-2.86	-2.86
Quartz	SiO2		-1.52		-0.26
Sepiolite	Mg2Si3O7.5OH:3H2O		1.95		-0.65
Sepiolite(d)	Mg2Si3O7.5OH:3H2O		-0.95		-3.55
Siderite	FeCO3	-2.69		-2.98	-2.05
SiO2(a)	SiO2		-2.79		-1.53
Strontianite	SrCO3	-0.73	0.32	-0.73	-0.99
Talc	Mg3Si4O10(OH)2		7.95		3.41
Vivianite	Fe3(PO4)2:8H2O	-6.66		-7.73	

D-3 PHREEQC calculated concentrations in surface water after batch reaction

Species	OCM at T=0 Molality	OCM final Molality	BASE at T=0 Molality	BASE final Molality
OH-	5.12E-06	2.31E-06	4.96E-06	4.13E-06
H+	4.03E-09	8.94E-09	4.16E-09	5.00E-09
H2O	5.55E+01	5.55E+01	5.55E+01	5.55E+01
B	4.04E-04	4.05E-04	4.04E-04	4.04E-04
Br	7.14E-04	7.16E-04	7.14E-04	7.14E-04
C(-4)	1.07E-03	1.13E-11	3.91E-04	5.63E-06
C(4)	2.46E-03	2.12E-03	1.82E-03	1.58E-03
Ca	9.10E-03	9.12E-03	9.10E-03	9.10E-03
Cl	4.83E-01	4.84E-01	4.83E-01	4.83E-01
F	6.43E-05	6.44E-05	6.43E-05	6.43E-05
Fe(2)	1.04E-06	9.75E-07	1.01E-06	9.89E-07
Fe(3)	4.02E-13	7.70E-13	4.12E-13	4.71E-13
H(0)	3.51E-09	2.95E-11	2.92E-09	9.93E-10
K	8.72E-03	8.74E-03	8.72E-03	8.72E-03
Mg	4.75E-02	4.74E-02	4.73E-02	4.74E-02
Na	3.65E-01	3.66E-01	3.65E-01	3.65E-01
O(0)	0.00E+00	0.00E+00	0.00E+00	0.00E+00
P	5.79E-04		4.58E-04	
S(-2)	3.56E-09	3.32E-10	3.24E-09	1.89E-09
S(6)	2.43E-11	2.00E-04	4.50E-11	1.63E-09
Si	2.64E-03	6.07E-02	2.99E-03	6.05E-03
Sr	8.05E-05	8.07E-05	8.05E-05	8.05E-05

Description of solution

	OCM at T=0	OCM final	BASE at T=0	BASE final
pH (charge balance)	8.512	8.167	8.499	8.419
pe (adjust to redox equilibrium)	-5.737	-4.354	-5.683	-5.369
Ionic strength	5.42E-01	5.44E-01	5.41E-01	5.42E-01
Total alkalinity (eq/kg)	4.00E-03	4.30E-03	3.08E-03	2.25E-03
Total CO2 (mol/kg)	2.46E-03	2.12E-03	1.82E-03	1.58E-03
Electrical balance (eq)	-1.71E-03	-2.36E-03	-1.07E-03	2.62E-04
Percent error 100*(Cat-|An|)/(Cat+|An|)	-0.18	-0.24	-0.11	0.03

Appendix E $FeCl_2 \cdot xH_2O$ added to the chambers

Standards were made by mix 0.029 g of $FeCl_2 \cdot xH_2O$ in 10 ml of either artificial seawater (STD 1-3) or de-ionized water (STD 4-6).

Results from ICP-AES

Parameter:	Fe	Mn	Ca	Mg	S	Si	Al	Ni	P
MRL	0.10	0.02	0.1	0.10	0.1	0.1	0.01	0.02	0.01
Sample	µg/ml	µg/ml	µg/ml	µg/ml	µg/ml	µg/ml	µg/ml	µg/ml	µg/ml
FeCl2_STD_1	758	< 0.01	304	1090	0.34	< 0.01	< 0.01		
FeCl2_STD_2	888	< 0.01	317	1120	0.35	< 0.01	< 0.01		
FeCl2_STD_3	862	< 0.01	319	1120	0.36	< 0.01	< 0.01		
FeCl2_STD_4	890	0.04	7.09	0.75	0.2	0.03		0.16	0.06
FeCl2_STD_5	897	0.04	0.2	ND	0.11	0.29		0.17	0.05
FeCl2_STD_6	921	0.03	0.9	ND	0.2	1.04		0.16	0.05

Calculated molecular weight

Sample	$FeCl_2 \cdot xH_2O$ (g)	water (ml)	Calculated molecular weight of $FeCl_2 \cdot xH_2O$ (g/mol)
FeCl2_STD_1	0.0291	10.75	199.29
FeCl2_STD_2	0.0299	10.07	186.67
FeCl2_STD_3	0.299	10.07	192.3
FeCl2_STD_4	0.293	10.01	183.63
FeCl2_STD_5	0.0297	9.94	186.08
FeCl2_STD_6	0.0295	10.45	171.20

MAIJA RAUDSEPP

EDUCATION

2010 - 2012	Master of Science in Geology with Environment and Sustainability The University of Western Ontario Thesis: Late Archean oceans: a laboratory model of oxygen oases Supervisor: Dr. Gordon Southam
2005 - 2009	Bachelor of Science (Honours) Environmental Earth Sciences The University of Alberta Thesis: Provenance of mainland erratics on S. Banks Island, NWT Supervisor: Dr. John England Directed Study: Metal adsorption in alginate Supervisor: Dr. Kurt Konhauser

EMPLOYMENT HISTORY

2010 -2012	Earth Sciences Teaching Assistant, University of Western Ontario Fall 2010 ES1083F Life on Planet Earth Winter 2011 ES1086F Origin and Geology of the Solar System Winter 2012 Earth Sciences Department Outreach and ES1089G Earth, Art and Culture
2007-2009 (May-Aug)	Quaternary Geology Summer Research Assistant Dr. John England, University of Alberta

SELECT AWARDS

2011-2012	Ontario Graduate Scholarship
2012	Environment and Sustainability Program Graduate Student Award
2009	Dean's Silver Medal in Science, University of Alberta
2006-2009	Petro-Canada Emerging Leaders Dean's Citation
2008	NSERC Undergraduate Student Research Award
2007	NSERC Undergraduate Student Research Award

RESEARCH PUBLICATIONS

Raudsepp, M., Banerjee, N.R. and Southam, G. 2012. Archean laboratory models possessing photosynthetic microbial mats. Goldschmidt Geochemistry Conference, Montreal, poster.

Petrash, D.A., Lalonde, S. V.. **Raudsepp, M**. and Konhauser, K. O. 2011. Assessing the importance of organic matrix materials in biofilm chemical reactivity: Insights from proton and cadmium adsorption onto the commercially available biopolymer alginate. Geomicrobiology Journal, **28**(3): 266-273.